AN EVALUATION OF MICROSTRUCTURAL FACTORS AFFECTING COLD HEADABILITY OF MEDIUM CARBON STEELS

by

Saad N. Almotham

A thesis submitted to the Faculty and the Board of Trustees of the Colorado School of Mines in partial fulfillment of the requirements for the degree of Master of Science (Metallurgical and Materials Engineering).

Golden, Colorado

Date: 08/26/2013

Signed: _____
Saad N. Almotham

Signed: _____
Dr. David K. Matlock
Thesis Advisor

Golden, Colorado

Date: 8/24/13

Signed: _____
Dr. Chester Van Tyne
Professor and Interim Department Head
Department of Metallurgical
and Materials Engineering

ABSTRACT

Cold heading is a cold forging operation that is of increasing importance in the steel industry. A series of 1045 steels, 41XX steels, two 16MnCr5 steels and a 1080V steel were evaluated using a laboratory cold heading test in order to evaluate the effects of chemical composition and microstructural variations on cold headability of steel. In addition, heat-treatment schedules were performed on a 10V45 w/Nb material in order to evaluate cold headability of various steel microstructures processed from the same base material. All samples were machined using a 16G surface finish. Lubrication was found to cause an unstable deformation mode and thus, all tests were performed after acetone wiping to ensure consistent friction conditions by removal of residual oil films. Imposed deformation speeds of 0.15, 1.5 and 15 mm/s during testing of as-received 1045 materials showed that fracture behavior in microalloyed 1045 materials was independent of deformation speed and thus, a test speed of 15 mm/s was used for all tests. Three types of cracks were observed in cold-headed samples: longitudinal, shear and 'mixed' mode. However, cracks which nucleated at low strains were found to be longitudinal for all materials except for hot-rolled 4140 which exhibited a tendency towards shear cracking. Fracture limits, defined as the true compressive strain at which no cracks were detected at 20X, were found to correlate with hardness and sulfur content of the steels. Increasing hardness and sulfur content corresponded to a decrease in the fracture limit. Fracture in all materials occurred by ductile rupture via void nucleation and growth and void nucleation was found to be enhanced by sulfide inclusions in 1045 and heat-treated 10V45 materials. Testing of heat-treated 10V45 w/Nb materials was unable to assign fracture limit values as small longitudinal cracks were observed at strains lower than the fracture limit of as-received 10V45 w/Nb. Spheroidized 41XX materials exhibited the best formabilities of all materials. Pre-drawing enhanced cold headability of 4140 and 4135 but had a limited effect on PL41. The 1045 materials had lower fracture limits than 41XX materials despite having comparable hardnesses. Testing of 16MnCr5 and 1080V materials revealed that a high carbon steel with a low sulfur content can undergo approximately the same amount of deformation as a low carbon steel with a high sulfur content without fracture. Surface roughening occurred as either uniform orange peel or longitudinal surface relief. The type of surface roughening corresponded to microstructures of the different materials.

TABLE OF CONTENTS

ABSTRACT iii

LIST OF FIGURES vii

LIST OF TABLES xv

Acknowledgements xvi

CHAPTER 1 : INTRODUCTION 1

CHAPTER 2 : LITERATURE REVIEW 2

2.1 Cold Heading Process 2

2.2 Advantages of Cold Heading 2

2.3 Cold Heading Wire Material Requirements 3

2.3.1 Surface Requirements 3
2.3.2 Cleanliness 3
2.3.3 Chemical Composition 3
2.3.4 Microstructure 4
2.3.5 Pre-drawing 5

2.4 Cold Heading Parameters 5

2.4.1 Strain Rate 6
2.4.2 Strain 6
2.4.3 Lubrication 6

2.5 Cold Headability/Ductile Fracture Criteria 7

2.5.1 Micromechanical Approach to Ductile Failure 7
2.5.2 Macromechanical Approach to Ductile Failure 8

2.6 Assessment of Cold Headability 8

2.6.1 Tensile Test 8
2.6.2 Upset Test 9
2.6.3 Drop Weight Impact Test 9

2.7 Shear Banding 10

CHAPTER 3 : EXPERIMENTAL DESIGN AND PROCEDURE 11

3.1 Purpose of Project and Experimental Approach 11

3.2 Identification of a Laboratory Cold Heading Test 11

3.1 Material Selection 12

3.2 Sample Preparation and Machining 14

3.1 Testing Parameters 16

3.2 Testing Procedure 18

3.3 Metallography and Material Characterization 18
3.4 Fractography and Fracture Evaluation 19
3.1 Examining Flow Behavior 19
3.2 Heat Treatment Procedure 20
3.3 Heat Treatment Schedules of 10V45 w/Nb 21
3.4 Inclusion Analysis 22
CHAPTER 4 : RESULTS 24
4.1 Introduction 24
4.2 Testing Procedure 24
4.2.1 Effects of Lubrication 24
4.2.2 Reproducibility 25
4.3 Characterization of As-received Materials 26
4.1 Characterization of Heat-treated Materials 28
4.2 Effects of Strain Rate Variation 34
4.3 Fracture Limits for As-received Materials 41
4.4 Comparative Study of Fracture Evolution in As-received Materials 42
4.5 Cold Heading Response for 10V45 w/Nb Heat-treated Materials 45
4.6 Grain Flow and Stress-Strain Curves 72
4.1 Fractography and Fracture Analysis 75
4.2 Inclusion Analysis 86
CHAPTER 5 : DISCUSSION OF EXPERIMENTAL RESULTS 88
5.1 Introduction 88
5.2 Developed Test Procedure 88
5.3 Characterization of As-received Materials 88
5.4 Characterization of Heat-treated Materials 90
5.5 Effects of Deformation Speed Variation for As-received 1045 Materials 92
5.6 Cold Heading Response of As-received Materials 93
5.1 Cold Heading Response of Heat-treated Materials 95
5.2 Surface Features 98
CHAPTER 6 : CONCLUSIONS 100
CHAPTER 7 : FUTURE WORK 103
REFERENCES 104
APPENDIX A: CALCULATIONS FOR SAMPLE DIMENSIONS 106

APPENDIX B: SUMMARY OF CRACK SEVERITY FOR 1045 SERIES SAMPLES TESTED AT THE THREE DEFORMATION SPEEDS 109

APPENDIX C: SULFIDE LENGTH DISTRIBUTION CHARTS FROM INCLUSION ANALYSIS DATA 116

LIST OF FIGURES

Figure 2.1 Schematic illustration showing a common form of the cold heading process in which a head is formed between a punch and a die [1]. 2

Figure 2.2 Schematic illustration of the microvoid nucleation, growth and coalescence process [9]. 4

Figure 2.3 Schematic illustration of the wire drawing process [14]. 5

Figure 2.4 Schematic forming limit diagram for a cold heading sample. Strain path a is followed using no lubrication and strain path b is achieved through lubrication. Cold heading Material B along strain path a results in failure. Mitigation of this problem is done by either switching to Material A or following strain path b [20]. 7

Figure 2.5 Schematic illustrations of compression fracture planes described by Kudo and Asi [20]. 9

Figure 3.1 Schematic illustrations of the possible variations for a laboratory upsetting test. (a) Unsupported upset test (b) one-sided supported upset test (c) two-sided supported upset test. 12

Figure 3.2 (a) Schematic illustration of the die configuration showing the inner hardness test blocks (b) The actual die configuration. 13

Figure 3.3 Schematic illustration showing the inverse relation between strength (hardness) and ductility (compression limit). Low carbon steels generally have low strength levels and high ductility while the opposite is true for high carbon steels. Medium carbon steels exhibit an intermediate ductility and strength capabilities. 14

Figure 3.4 Schematic illustrations of where samples are machined with respect to the as received materials cross sections. Dimensions are in mm. (a) 1045 alloys (b) 41XX alloys (c) 1080V (d) 16MnCr5. 17

Figure 3.5 Stereo microscope macrograph of a quenched and tempered 10V45 w/Nb sample at 20X. Arrows point to examples of what are considered ‘incipient cracks’ in the context of this work. 20

Figure 4.1 Image of 1045 Al samples tested with the application of an oil lubricant. The samples were tested (from left to right) using the slow, medium and fast speeds. The unstable mode of deformation is clear in samples compressed with the medium and high strain rates. 25

Figure 4.2 (a) Load-displacement and (b) true stress-strain curves for duplicate sample sets of 1045 Al and 1045 Al-TMP tested with the medium strain rate (1.5 mm/s) to the indicated displacement/strain. Each set is represented with thin solid and bold dashed lines for the first and duplicate sample, respectively. The curves are not corrected for machine stiffness. 25

Figure 4.3 Light optical micrographs of longitudinal sections of 1045 series materials. The direction of rolling is horizontal. (a) 1045 Al, HV=218 (b) 1045 Al, TMP HV=196 (c) 10V45, HV=255 (d) 10V45 TMP, HV=259 (e) 10V45 w/Nb, HV=275 (f) 10V45 w/Nb TMP, HV=247. Etchant is 2 pct nital. 27

Figure 4.4 Light optical micrographs of longitudinal sections for the 4135 materials. The direction of rolling is horizontal. (a) Hot-rolled 4135, HV=299 (b) pre-drawn 4135, HV=277 (c) spheroidized 4135, HV=195. Etchant is 2 pct nital. 29

Figure 4.5 Light optical micrographs of longitudinal sections for the 4140 materials. The direction of rolling is horizontal. (a) Hot-rolled 4140, HV=319 (b) pre-drawn 4140, HV=290 (c) spheroidized 4140, HV=195. Etchant is 2 pct nital. 30

Figure 4.6 Light optical micrographs of longitudinal sections for the PL41 materials. The direction of rolling is horizontal. (a) Hot-rolled PL41, HV=255 (b) pre-drawn PL41, HV=315 (c) spheroidized PL41, HV=155. Etchant is 2 pct nital. 31

Figure 4.7 Light optical micrographs of low carbon materials. (a) Hot-rolled (HR) and (b) control-rolled (CR)16MnCr5 materials HV= 220, 189 for (a) and (b), respectively. Etchant is picral acid [29]. 32

Figure 4.8 SEM micrographs at (a) low magnification and (b) high magnification of 1080V material. HV= 361 [30]. 33

Figure 4.9 Light optical micrographs of a longitudinal section from a representative spheroidized 10V45 w/Nb sample. (Austenitized at 1000 °C for an hour, water quenched, heated to 700°C for 48 hours and air cooled.) HV=194. The direction of rolling is horizontal. (a) Low magnification (b) high magnification. Etchant is 2 pct nital. 35

Figure 4.10 Light optical micrographs of longitudinal sections of heat-treated 10V45 w/Nb samples: (a) Normalized (heated to 1000 °C and air cooled) HV=292, (b) normalized (same treatment in (a)) and aged (heated to 625°C for an hour) HV=292, (c) normalized (same treatment in (a)) and over-aged (heated to 675 °C for an hour) HV=262. The direction of rolling is horizontal. Etchant is 2 pct nital. 36

Figure 4.11 Light optical micrographs of longitudinal sections of heat-treated 10V45 w/Nb samples austenitized at 866 °C and isothermally transformed for 20 minutes at 435 °C. HV=303. (a) Low magnification (b) high magnification. The direction of rolling is horizontal. Etchant is 2 pct nital. 37

Figure 4.12 Light optical micrographs of longitudinal sections of heat-treated 10V45 w/Nb samples austenitized at 866 °C and isothermally transformed for 20 minutes at 365 °C. HV=322. (a) Low magnification (b) high magnification. The direction of rolling is horizontal. Etchant is 2 pct nital. 38

Figure 4.13 Light optical micrographs of longitudinal sections of the heat-treated 10V45 w/Nb samples austenitized at 870 °C, water quenched and tempered at 615 °C for two hours. HV= 304. (a) Low magnification (b) high magnification. The direction of rolling is horizontal. Etchant is 2 pct nital. 39

Figure 4.14 Light optical micrographs of longitudinal sections of the 10V45 w/Nb heat-treated condition austenitized at 870 °C, water quenched and tempered at 590 °C for two hours. HV=320. (a) Low magnification (d) high magnification. The direction of rolling is horizontal. Etchant is 2 pct nital. 40

Figure 4.15 (a) Load-displacement curves for three samples of 10V45 w/Nb tested with the indicated strain rates. (b) A magnified view of the low displacement behavior shown in (a). The curves are not corrected for machine stiffness. 41

Figure 4.16 Macrographs of 1045 Al cold-headed samples at two levels of strain and two magnifications. Fracture limit is 0.85 true compressive strain. (a) and (b) 1.15 true compressive strain (c) and (d) 1.52 true compressive strain. 46

Figure 4.17 Macrographs of 10V45 cold-headed samples at three levels of strain and two magnifications. Fracture limit is 0.69 true compressive strain. (a) and (b) 0.89 true compressive strain (c) and (d) 1.15 true compressive strain (e) and (f) 1.52 true compressive strain. 47

Figure 4.18 Macrographs of 10V45 TMP cold-headed samples at one level of strain and two magnifications. Fracture limit is 0.64 true compressive strain. (a) and (b) 0.89 true compressive strain. 48

Figure 4.19 Macrographs of 10V45 w/Nb cold-headed samples at one level of strain and two magnifications. Fracture limit is 0.69 true compressive strain. (a) and (b) 0.89 true compressive strain. 48

Figure 4.20 Macrographs of hot-rolled 4135 cold-headed samples at three levels of strain and two magnifications. Fracture limit is 1.24 true compressive strain. (a) and (b) 0.87 true compressive strain (c) and (d) 1.13 true compressive strain (e) and (f) 1.38 true compressive strain. 49

Figure 4.21 Macrographs of pre-drawn 4135 cold-headed samples at three levels of strain and two magnifications. Fracture limit is 1.43 true compressive strain. (a) and (b) 0.89 true compressive strain (c) and (d) 1.15 true compressive strain (e) and (f) 1.43 true compressive strain. 50

Figure 4.22 Macrographs of spheroidized 4135 cold-headed samples at three levels of strain and two magnifications. No cracks were detected at 20X magnification on a stereo microscope at a true compressive strain as high as 1.98 true compressive strain. (a) and (b) 0.89 true compressive strain (c) and (d) 1.15 true compressive strain (e) and (f) 1.52 true compressive strain. 51

Figure 4.23 Macrographs of hot-rolled 4140 cold-headed samples at three levels of strain and two magnifications. Fracture limit is 0.86 true compressive strain. (a) and (b) 0.86 true compressive strain (c) and (d) 1.15 true compressive strain (e) and (f) 1.52 true compressive strain. 52

Figure 4.24 Macrographs of pre-drawn 4140 cold-headed samples at three levels of strain and two magnifications. Fracture limit is 1.24 true compressive strain. (a) and (b) 0.87 true compressive strain (c) and (d) 1.11 true compressive strain (e) and (f) 1.52 true compressive strain. 53

Figure 4.25 Macrographs of spheroidized 4140 cold-headed samples at three levels of strain and two magnifications. No cracks were detected at 20X magnification on a stereo microscope at a true compressive strain as high as 1.94 true compressive strain. (a) and (b) 1.15 true compressive strain (c) and (d) 1.52 true compressive strain (e) and (f) 1.73 true compressive strain. 54

Figure 4.26 Macrographs of hot-rolled PL41 cold-headed samples at three levels of strain and two magnifications. Fracture limit is 1.35 true compressive strain. (a) and (b) 0.89 true compressive strain (c) and (d) 1.13 true compressive strain (e) and (f) 1.43 true compressive strain. 55

Figure 4.27 Macrographs of pre-drawn PL41 cold-headed samples at three levels of strain and two magnifications. Fracture limit is 1.24 true compressive strain. (a) and (b) 0.89 true compressive strain (c) and (d) 1.14 true compressive strain (e) and (f) 1.52 true compressive strain. 56

Figure 4.28 Macrographs of spheroidized PL41 cold-headed samples at three levels of strain and two magnifications. No cracks were detected at 20X magnification on a stereo microscope at a true compressive strain as high as 2.02 true compressive strain. (a) and (b) 0.89 true compressive strain (c) and (d) 1.15 true compressive strain (e) and (f) 1.52 true compressive strain. 57

Figure 4.29 Macrographs of HR 16MnCr5 cold-headed samples at three levels of strain and two magnifications. Fracture limit is 0.95 true compressive strain. (a) and (b) 0.89 true compressive strain (c) and (d) 1.15 true compressive strain (e) and (f) 1.52 true compressive strain. 58

Figure 4.30 Macrographs of CR 16MnCr5 cold-headed samples at three levels of strain and two magnifications. Fracture limit is 0.91 true compressive strain. (a) and (b) 0.89 true compressive strain (c) and (d) 1.15 true compressive strain (e) and (f) 1.52 true compressive strain. 59

Figure 4.31 Macrographs of 1080V cold-headed samples at three levels of strain and two magnifications. Fracture limit is 0.86 true compressive strain. (a) and (b) 0.89 true compressive strain (c) and (d) 1.15 true compressive strain (e) and (f) 1.52 true compressive strain. 60

Figure 4.32 Macrographs of spheroidized (austenitized at a 1000 °C for an hour, water quenched, heated to 700 °C for 48 hours and air cooled) 10V45 w/Nb cold-headed samples at three levels of strain and two magnifications. Cracks are observed at 20X on a stereo microscope at a strain level as low as 0.57 true compressive strain. (a) and (b) 0.89 true compressive strain (c) and (d) 1.15 true compressive strain (e) and (f) 1.52 true compressive strain. 64

Figure 4.33 Macrographs of normalized (austenitized at 1000 °C for an hour and air cooled) 10V45 w/Nb cold-headed samples at three levels of strain and two magnifications. Cracks are observed at 20X on a stereo microscope at a strain level as low as 0.57 true compressive strain. (a) and (b) 0.89 true compressive strain (c) and (d) 1.15 true compressive strain (e) and (f) 1.52 true compressive strain. 65

Figure 4.34 Macrographs of normalized and aged (austenitized at 1000 °C for an hour, air cooled, heated to 625 °C for an hour and air cooled) 10V45 w/Nb cold-headed samples at three levels of strain and two magnifications. Cracks are observed at 20X on a stereo microscope at a strain level as low as 0.57 true compressive strain. (a) and (b) 0.89 true compressive strain (c) and (d) 1.15 true compressive strain (e) and (f) 1.52 true compressive strain. 66

Figure 4.35 Macrographs of normalized and over-aged (austenitized at 1000 °C for an hour, air cooled, heated to 675 °C for an hour and air cooled) 10V45 w/Nb cold-headed samples at three levels of strain and two magnifications. Cracks are observed at 20X on a stereo microscope at a strain level as low as 0.57 true compressive strain. (a) and (b) 0.89 true compressive strain (c) and (d) 1.15 true compressive strain (e) and (f) 1.52 true compressive strain. 67

Figure 4.36 Macrographs of higher-temperature isothermal hold (austenitized at 866 °C for 10 minutes, rapidly cooled to 435 °C and held for 20 minutes and air cooled) 10V45 w/Nb cold-headed samples at three levels of strain and two magnifications. Cracks are observed at 20X on a stereo microscope at a strain level as low as 0.49 true compressive strain. (a) and (b) 0.89 true compressive strain (c) and (d) 1.15 true compressive strain (e) and (f) 1.52 true compressive strain. 68

Figure 4.37 Macrographs of lower-temperature isothermal hold (austenitized at 866 °C for 10 minutes, rapidly cooled to 365 °C and held for 20 minutes and air cooled) 10V45 w/Nb cold-headed samples at three levels of strain and two magnifications. Cracks are observed at 20X on a stereo microscope at a strain level as low as 0.49 true compressive strain. (a) and (b) 0.89 true compressive strain (c) and (d) 1.15 true compressive strain (e) and (f) 1.52 true compressive strain. 69

Figure 4.38 Macrographs of quenched and higher-temperature temper (austenitized at 870 °C for 10 minutes, water quenched, tempered at 615 °C for two hours and air cooled) 10V45 w/Nb cold-headed samples at three levels of strain and two magnifications. Cracks are observed at 20X on a stereo microscope at a strain level as low as 0.49 true compressive strain. (a) and (b) 0.89 true compressive strain (c) and (d) 1.15 true compressive strain (e) and (f) 1.52 true compressive strain. 70

Figure 4.39 Macrographs of quenched and lower-temperature temper (austenitized at 870 °C for 10 minutes, water quenched, tempered at 590 °C for two hours and air cooled) 10V45 w/Nb cold-headed samples at three levels of strain and two magnifications. Cracks are observed at 20X on a stereo microscope at a strain level as low as 0.49 true compressive strain. (a) and (b) 0.89 true compressive strain (c) and (d) 1.15 true compressive strain (e) and (f) 1.52 true compressive strain. 71

Figure 4.40 Stereo microscope images of 1045 Al samples cold headed at 15 mm/s to (a) 1.15 and (b) 1.52 true compressive strains. Samples were longitudinally sectioned and macroetched in a solution of 50 vol pct HCl and 50 vol pct DI water at a temperature range between 70 and 80 °C. 72

Figure 4.41 True stress-strain curves for representative samples of the 1045 series. 73

Figure 4.42 True stress-strain curves for representative samples of the 41XX series. 74

Figure 4.43 True stress-strain curves for representative samples of the low and high carbon materials (HR and CR 16MnCr5 and 1080V). 75

Figure 4.44 True stress-strain curves for representative samples of the heat-treated 10V45 w/Nb materials. 76

Figure 4.45 (a) Low and (b) high magnification SEM fractographs of a cold headed 1045 Al sample. Area boxed in (a) is magnified in (b) A trace of an MnS inclusion was verified in (b) and is highlighted by the arrow. Axis of loading is vertical. 78

Figure 4.46 (a) Low and (b) high magnification SEM fractographs of a cold-headed heat-treated 10V45 w/Nb sample (quenched and high temperature temper). Area boxed in (a) is magnified in (b). Manganese sulfide inclusions have been verified in (b). Axis of loading is vertical. 79

Figure 4.47 (a) Low and (b) high magnification SEM fractographs of a cold headed pre-drawn 4140 sample. Vertical longitudinal surface relief bands parallel to the crack can be seen in (a). Area boxed in (a) is magnified in (b). Axis of loading is vertical. 80

Figure 4.48 SEM fractograph of a cold headed hot-rolled 4140 sample. Longitudinal surface features are highlighted by arrows as well as shear bands. A shear crack propagates diagonally through the image. Axis of loading is vertical. 81

Figure 4.49 Optical micrograph of a normalized 10V45 w/Nb sample illustrating void nucleation at a broken inclusion. The micrograph is taken approximately midway through the cold-headed height near the outer surface. Axis of loading is normal to the cross section. 81

Figure 4.50 Optical micrograph of a normalized and aged 10V45 w/Nb sample illustrating void nucleation at a broken inclusion. The micrograph is taken approximately midway through the cold-headed height at the outer surface. Axis of loading is normal to the cross section. 82

Figure 4.51 Optical micrograph of a spheroidized 10V45 w/Nb sample illustrating initial void nucleation at a probable inclusions site. The micrograph is taken approximately midway through the cold-headed height at the outer surface. Axis of loading is normal to the cross section. 82

Figure 4.52 Optical micrograph of a spheroidized 10V45 w/Nb sample illustrating void nucleation inclusions and a crack at the surface. These features are indicated by arrows. The micrograph is taken approximately midway through the cold-headed height at the outer surface. Axis of loading is normal to the cross section. 83

Figure 4.53 Optical micrograph of a quenched and high temperature temper 10V45 w/Nb sample illustrating void nucleation at the area highlighted by the arrow. The micrograph is taken approximately midway through the cold-headed height at the outer surface. Axis of loading is normal to the cross section. 83

Figure 4.54 (a), (b) Optical micrographs of as-received 10V45 w/Nb sample illustrating void nucleation at inclusions sites. Micrographs are taken approximately midway through the cold-headed height at the outer surface. Axis of loading is normal to the cross section. 84

Figure 4.55 Optical micrograph of an over-aged 10V45 w/Nb sample illustrating initial void nucleation and a probable trace of an inclusion. The micrograph is taken approximately midway through the cold-headed height at the outer surface. Axis of loading is normal to the cross section..... 85

Figure 4.56 Optical micrograph of a quenched and high temperature temper 10V45 w/Nb sample illustrating initial void nucleation and preferential crack propagation to inclusion sites. The micrograph is taken approximately midway through the cold-headed height at the outer surface. Axis of loading is normal to the cross section. 85

Figure 4.57 Optical micrograph of a 1045 Al TMP showing a large crack. The micrograph is taken approximately midway through the cold-headed height at the outer surface. Axis of loading is normal to the cross section..... 86

Figure 4.58 Sulfide length distribution charts for a) 10V45 w/Nb b) hot-rolled 4135. 87

Figure 5.1 Fracture limit as a function of sulfur content for as-received materials. Fracture limits of spheroidized 41XX materials are greater than the data points in the plot..... 95

Figure 5.2 Fracture limit as a function of total sulfide length for as-received materials used in the inclusion analysis..... 96

Figure 5.3 Fracture limit as a function of Vickers hardness for as-received materials..... 96

Figure A.1 Schematic illustration of a frictionless upsetting process..... 107

Figure A.2 Theoretical load-displacement curves for low and high carbon steels of the various indicated diameters (mm). The low carbon steel has an n=0.21 and a K=600 MPa and the high carbon has an n=0.12 and a K=2650 MPa [29].The h/d ratio was assumed to be two for all materials. 108

Figure B.1 Macrograph of a 1045 Al TMP sample cold headed to 72 pct engineering strain using the 0.15 mm/s speed. This sample represents an uncracked sample with respect to strain rate effects evaluation. Compressed height = 3.16 mm. 110

Figure B.2 Macrographs of laboratory cold headed samples showing increasing degree of longitudinal cracking severity. (a) 10V45-TMP sample cold headed to 63.3% engineering strain using the 15 mm/s speed. Low severity longitudinal cracks are illustrated. Compressed height = 4.18 mm (b) 10V45 w/Nb sample cold headed to 68.9% engineering strain using the 0.15 mm/s speed. Moderate longitudinal cracks are illustrated. Compressed height = 3.20 mm (c) 1045 Al-TMP sample cold headed to 75.5% engineering strain using the1.5 mm/s speed. High severity longitudinal cracks are illustrated. Compressed height = 2.68 mm. 111

Figure B.3 Photographs of laboratory cold headed samples showing increasing degree of shear crack severity. (a) 1045 Al TMP sample cold headed to 76.1% engineering strain using the 1.5 mm/s speed. Low severity shear cracks are pointed out by the arrows. Compressed height = 2.68 mm (b) 1045 Al TMP sample cold headed to 68.5% engineering strain using the 15 mm/s speed. Moderate severity shear cracking is illustrated. Compressed height = 3.59 mm (c) 10V45 sample cold headed to 80.0% engineering strain using the 0.15 mm/s speed. High degree of shear cracking is shown. Compressed height = 2.68 mm. 112

Figure C.1 Sulfide length distribution charts for a) 1045 Al b) 1045 Al TMP. 117

Figure C.2 Sulfide length distribution charts for a) 10V45 b) 10V45 TMP..... 117

Figure C.3 Sulfide length distribution charts for a) 10V45 w/Nb b) 10V45 w/Nb TMP. 118

Figure C.4 Sulfide length distribution chart for hot-rolled 4135. 118

Figure C.5 Sulfide length distribution charts for a) CR 16MnCr5 and b) 1080V. 119

LIST OF TABLES

Table 3.1 - Chemical Compositions of Experimental Steels (wt pct.) 15

Table 3.2 – Summary of Reheat and Finish Rolling Temperatures for the 1045 Base Steels 16

Table 3.3 – Wire Diameters of the 41XX Series Alloys in The As-received Condition 16

Table 3.4 - Heat Treatment Schedules of 10V45 w/Nb 23

Table 4.1 – Summary of Volume Fraction Data for 1045 Materials 28

Table 4.2 – Summary of Fracture Limit, Yield Stress and Hardness Data for As-received Materials 42

Table 4.3 – Summary of Fracture Limit, Yield Stress and Hardness Data for Heat-treated 10V45 w/Nb Samples 63

Table 4.4 – Inclusion Analysis Data 87

Table 5.1 – Summary of Volume Fraction Data, Vickers Hardness and Yield Stresses for 1045 Materials 90

Table B.1 – Summary of Cracking Severity for Selected 1045 Al Samples at The Three Deformation Speeds 113

Table B.2 – Summary of Cracking Severity for 1045 Al TMP Samples at The Three Deformation Speeds 113

Table B.3 – Summary of Cracking Severity for 10V45 Samples at The Three Deformation Speeds 114

Table B.4 – Summary of Cracking Severity for 10V45 TMP Samples at The Three Deformation Speeds 114

Table B.5 – Summary of Cracking Severity for 10V45 w/Nb Samples at The Three Deformation Speeds 115

Table B.6 – Summary of Cracking Severity for 10V45 w/Nb TMP Samples at The Three Deformation Speeds 115

ACKNOWLEDGEMENTS

I would like to thank a few people that without their help, the completion of this work could not have been possible.

Firstly, my advisor, Dr. David Matlock who was always accessible and helpful with his technical advice and guidance.

I would also like to thank my committee members, Dr. John Speer and Dr. Chester Van Tyne for their support.

In addition, I would like to dedicate a special thanks to Bob Cryderman for his insightful input and interest with regard to the project.

Special thanks are due to The Saudi Basic Industries Corporation (SABIC) for the invaluable opportunity to study at CSM and for their financial support throughout the duration of this project and also to the sponsors of ASPPRC.

I would like to thank Glenn Eavenson and Ken Farmer of Evraz North America for their help in conducting the inclusion analysis at their facilities.

I would also like to thank fellow students at ASPPRC. Especially, Greg Lehnhoff, Paul Gibbs, Lee Rothleutner, Haytham Al-Jabr, Venkkateesh Parthasarathi, Julian Stock, Zahra Ghanbari, Preston Wolfram, Stephanie Miller and Tyson Brown. I would also like to thank the ASPPRC undergraduate student assistants, Matthew Glazier and Alex Gonzalez.

On a personal level, I would like to thank my friends in the states, back home in Saudi Arabia and wherever they may be for their unconditional support and encouragement.

Last but not least, I would like to deeply thank my mother, my father, my sisters, my brothers, my nieces and my nephews for their love and support during my studies away from home over the past two years during my graduate studies and five years before that for my undergraduate studies.

CHAPTER 1 : INTRODUCTION

Cold heading is the cold forging operation where a compressive force is applied on a cylindrical metal part and metal is forced to flow creating a 'head'. The process is integral to the production of fasteners, i.e. bolts, screws etc. The process is of increasing importance from an industrial standpoint as increased interest in cold heading has been expressed by industry and ASPPRC sponsors.

Production of fasteners starts with hot rolling a rod. The rod is then typically descaled, coated, cold drawn during a step often referred to as pre-drawing (i.e. drawing prior to cold heading), spheroidized in a batch or a continuous furnace, cleaned, coated, inspected, cold headed and heat-treated after cold heading in order to achieve strength and ductility requirements. This project evaluates options to improve the process by testing alternative microstructures not traditionally used as an attempt to improve the economy of the process by eliminating or optimizing certain processing steps.

The focus of the project is medium carbon steels. A family of 1045 materials with variation in microalloying content and finish-rolling temperatures was employed in the study in order to investigate the potential for microalloying and thermomechanical processing in enhancing the strength of cold headed parts and, thereby, eliminating post-forming heat treatment. Heat-treatment of a 10V45 alloy containing niobium was carried out to produce various microstructures from the same base materials. These heat-treatments facilitated comparison between the cold heading behavior of various steel microstructures of the same base chemistry. In addition, three cold heading grade 41XX alloys were tested in the hot-rolled, pre-drawn and spheroidized conditions to compare the cold heading behavior. Finally, a high and low carbon steels are tested in order to obtain a broader sense of the cold heading behavior in relation to the medium carbon materials.

This thesis is divided into the following chapters. Chapter 1 is an introduction to the project highlighting the motivation and objective for the work. Chapter 2 is a literature review pertaining to the project. Chapter 3 details the experimental materials matrix and experimental design approach in order to achieve the project objectives. Chapter 4 presents experimental results from the project. Chapter 5 is a discussion of experimental results presented in Chapter 4. Chapter 5 outlines the major conclusions from the project. Chapter 7 discusses the options for potential continuation of this work.

CHAPTER 2 : LITERATURE REVIEW

2.1 Cold Heading Process

Cold heading refers to the forming operation in which the cross-sectional area of a blank is increased at one or more points along its length by applying a compressive force. The process is carried out at room temperature [1]. One form of the process is schematically illustrated in Figure 2.1.

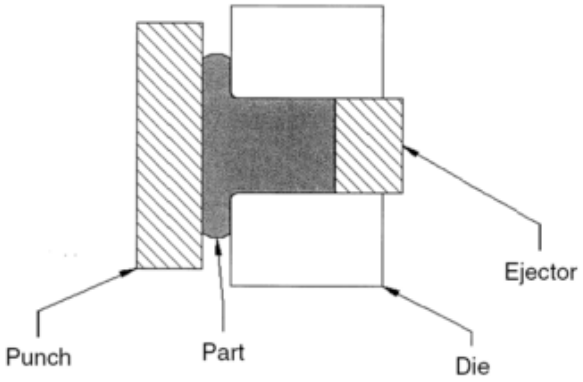

Figure 2.1 Schematic illustration showing a common form of the cold heading process in which a head is formed between a punch and a die [1].

A typical manufacturing process for cold heading steel starts with hot rolling a rod of an appropriate chemistry. The rod then undergoes a descaling step to remove scale and is coated to prevent the surface from corroding and providing a surface that is better lubricated during the subsequent cold drawing step. After cold drawing to size, the wire is then heat treated in a batch or a continuous furnace to produce a ductile spheroidized microstructure. The wire is then cleaned, coated, inspected and shipped for cold heading [2].

2.2 Advantages of Cold Heading

Cold heading possesses advantages over alternative methods for production of fasteners such as machining [1]. Cold heading is a high production rate process compared with machining where material is gradually removed until the final desired shape is obtained. Also, cold heading produces little to no scrap whereas machining can result in up to 60 vol pct of the material being scrapped. Additionally, cold heading provides increased strength of the part due to cold working. Cold heading also provides a means for controlled grain flow, thereby enhancing impact, fatigue and tensile strength by as much as 20% compared with parts produced by machining [3].

2.3 Cold Heading Wire Material Requirements

Quality requirements for cold heading steel wire include surface condition, cleanliness, chemical composition, microstructure and pre-drawing. Each requirement will be discussed independently in the following subsections.

2.3.1 Surface Requirements

The presence of surface defects is detrimental to workability as they promote the onset of cracking. These defects are mostly seams, cracks, shells and rolling laps and are characterized in terms of their depth, width and length. Defects may arise at any step in the production process and therefore, special care must be taken to minimize the occurrence of such defects [4]. Jenner *et al.* showed that longitudinal or transverse surface cracks or defects negatively influence workability [5]. Many researchers indicate that defects act as circumferential stress raisers and consequently result in an earlier fracture on the equatorial surface than in the absence of such defects [5, 6, 7]. However, Turner *et al.* speculated that the acuity of a surface notch decreases with equatorial expansion during heading but hypothesized that defects act as strain discontinuities that alter the strain path leading ultimately to localization of fracture on the equatorially expanding surface [8].

Inspection of the surface integrity may be done by hot eddy-current inspection, visual inspection and acid-pickle testing [5, 9]. In this work, surface effects are not a variable. Thus, test specimens all have a consistent surface finish.

2.3.2 Cleanliness

The presence of second-phase inclusions is detrimental to upsetability as they promote the formation of microvoids by decohesion at the inclusion-matrix interface. These microvoids ultimately lead to ductile fracture by microvoid nucleation, growth and coalescence mechanisms [9]. The steps of this process are schematically illustrated in Figure 2.2. Specific to C-Mn steels, the focus of this study, manganese sulfide (MnS) inclusions have been found to be an important factor in ductile fracture initiation [4, 6]. In the presence of such inclusions, second phase particles, such as carbides, have a minimal role to play in the initiation of microscopic voids [4].

2.3.3 Chemical Composition

Cold headability is sensitive to chemical composition. Increasing carbon content raises strength but inversely affects ductility and toughness [6]. Additionally, steels with medium carbon levels are subject to decarburization during post-forming heat treatment. The decarburization may enhance cold heading behavior by providing a more ductile structure at the equatorially expanding surface but may exhibit insufficient hardenability in subsequent processing. A compromise must be met to achieve a

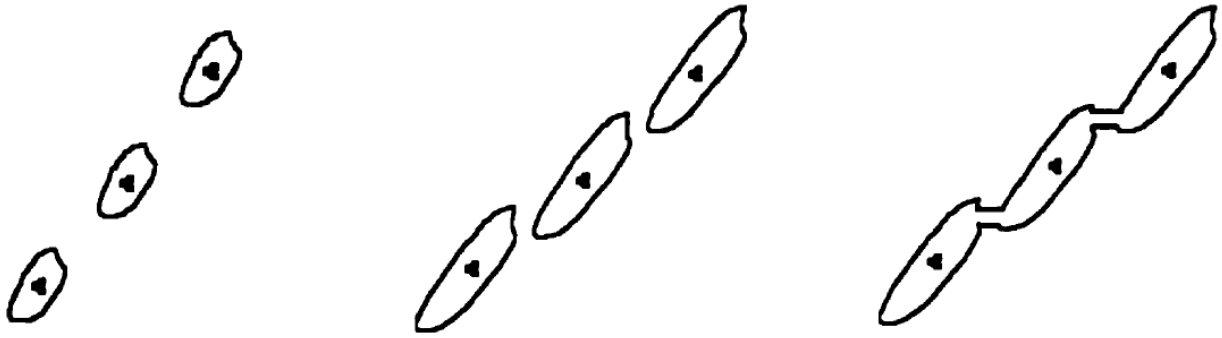

Figure 2.2 Schematic illustration of the microvoid nucleation, growth and coalescence process [9].

combination of strength and ductility appropriate for the final application of the part.

Cold headability is also affected by the content of residual elements (e.g. copper, nickel, chromium, molybdenum and tin) [7]. Residual elements are mainly present in steels produced by recycled scrap [10]. The content of residual element content should in order to achieve optimal cold headability performance through a sound steel making practice. The presence of residual elements negatively impacts ductility and increases hardness [7]. However, additions of hardenability agents, such as chromium and molybdenum, may be required for enhanced toughness despite their adverse effects on ductility [9]. In the presence of inclusions, however, the residual element content is less critical to the cold heading performance [11].

2.3.4 Microstructure

The most commonly used microstructure for cold heading of steel is a spheroidize annealed microstructure [6]. The microstructure consists of a continuous ferrite matrix with spheroidal carbides (cementite) dispersed within the matrix. This microstructure provides the advanced degree of ductility required for the extensive deformation in cold heading. A microstructure comprised of a ferrite matrix and pearlite is also used for cold heading applications. This microstructure is less desirable as it is resistant to deformation due to the fine lamellar cementite plate that subdivides the ferrite [9].

Spheroidization is performed industrially in a batch or a continuous furnace in a non-oxidizing environment in order to prevent decarburization and scale formation [12]. A spheroidized microstructure is the most stable microstructure in steel and may be attained from any prior microstructure given a sufficient heating time and temperature [13]. Spheroidization may be achieved subcritically by heating to below the A_1 temperature for extended amounts of time or intercritically by heating in the ferrite + austenite phase field [15]. Spherical carbides form to minimize the ferrite/carbide interfacial energy. Starting with pearlite, for example, the spherical particle yields the lowest surface area to volume ratio and is, therefore, more stable than the plate morphology associated with pearlite [13].

Ma showed by a means of a drop-weight test that cold headability of a steel containing 0.034 wt pct carbon, 0.94 wt pct manganese and 0.015 wt pct sulfur is inversely proportional to aspect ratio of cementite particles in pearlite colonies and the amount of inclusion content of the steel. A more spheroidized steel exhibited better cold headability [32]. Bainitic microstructures have been shown to have good cold headability and could serve to eliminate post-forming heat treatment in low carbon steels [15].

2.3.5 Pre-drawing

A wire drawing process after heat treatment and before cold heading has been demonstrated to improve cold headability [18, 19]. In the process, the cross-sectional area of the wire is reduced by drawing through a die that defines the final cross section. The process is schematically illustrated in Figure 2.3. Specifically, a 35-45 pct reduction in cross-sectional area through die with a bite angle of 15° serves to significantly improve headability [19]. Moreover, pre-drawing improves surface finish and, therefore, enhances cold headability. Drawing also provides a means for precision diameter control [20]. Classes of as hot-rolled and pre-drawn materials are utilized in this study.

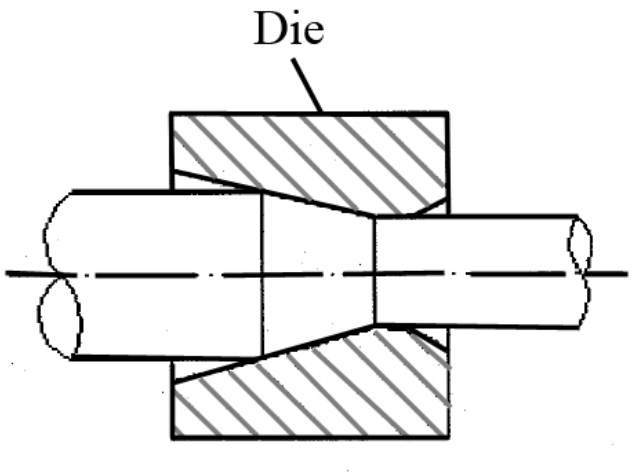

Figure 2.3 Schematic illustration of the wire drawing process [14].

2.4 Cold Heading Parameters

There are three main parameters in the cold heading process. These are strain rate, strain and lubrication. These parameters are discussed independently in the following subsections.

2.4.1 Strain Rate

Cold heading is a high strain rate process in which strain rates exceeding 100 s^{-1} are achievable [21]. The high strain rates provide for the high production rates that are one of the advantages of the process [3]. Flow stress and ductility may be strain-rate dependent. Therefore, it is important to simulate the strain rates used in the industrial process when assessing cold headability [22]. During high strain cold heading, about 90-95 pct of the mechanical energy is transferred into heat leading to flow softening. However, if strain rate is not high enough to induce considerable increases in temperature, higher strain rate leads to higher flow stress [23].

2.4.2 Strain

The amount of induced strain is another parameter in the cold heading process. The imposed deformation can be described by two primary strain components. The first is an axial compressive strain with respect to the height of the sample. The other is a tensile radial strain with respect to the diameter of the sample. The following equations are mathematical expressions for these two strains.

$$\varepsilon_{axial} = \ln\left(\frac{H}{H_0}\right) \qquad \text{Eq. 2.1}$$

$$\varepsilon_{radial} = \ln\left(\frac{D}{D_0}\right) \qquad \text{Eq. 2.2}$$

where ε is true strain, H is height, D is diameter and the subscript 0 indicates initial conditions. Forming limit diagrams are used for forming operations to predict the level of deformation the material can undergo before the onset of fracture. An example of a forming limit diagram is shown in Figure 2.4. The diagram is a plot of compressive strain in the loading direction versus tensile strain in the transverse direction. For a certain material, there exists a fracture locus line that is usually straight. This line indicates the combinations of compressive and tensile strains a material can undergo without failure. Following different strain paths through the application of lubrication or other means can enhance the cold heading behavior of a formed metal part [15].

2.4.3 Lubrication

Lubrication is used in the industrial cold heading process to minimize friction and improve cold headability. The rough contact between the surface of the formed part and the forming dies increases the deformation force resulting in an increased propensity for fracture. High friction leads to a non-uniform plastic deformation and surface barreling. Surface barreling induces secondary tensile stresses that result in longitudinal cracking [27].

2.5 Cold Headability/Ductile Fracture Criteria

It has been proven difficult to predict a general fracture criterion of metals due to the intricate interplay between many variables [24]. Therefore, various fracture criteria have been developed that

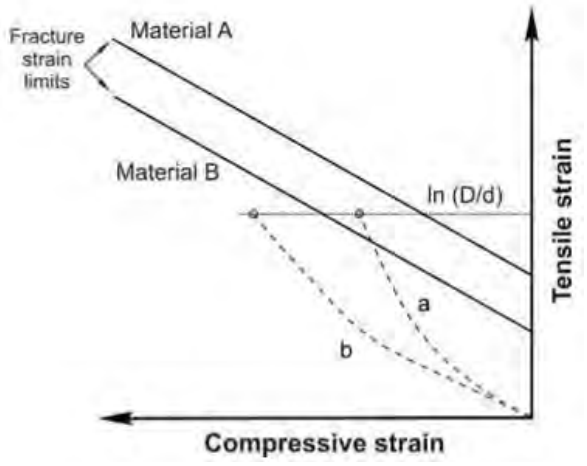

Figure 2.4 Schematic forming limit diagram for a cold heading sample. Strain path a is followed using no lubrication and strain path b is achieved through lubrication. Cold heading Material B along strain path a results in failure. Mitigation of this problem is done by either switching to Material A or following strain path b [20].

consider different variables and their effects on fracture during forming processes. There are two approaches usually used to predict the onset of fracture in forming operations: 1) Micromechanical Approach and 2) Macromechanical Approach.

2.5.1 Micromechanical Approach to Ductile Failure

This approach emphasizes the role of inclusions and second-phase particles in the ductile fracture process as they act as stress concentrators that give rise to microvoid nucleation at these sites. Upon subsequent loading, the nucleated voids grow and link resulting in failure of the part. This approach considers the size and distribution of second-phase particles. It is difficult to apply since it requires a significant amount of experimentation to establish a micromechanical criteria that applies on a macroscopic scale [9]. An example of these criteria is given by Oyane *et al.* [25]. In this criterion, ductile fracture occurs when the total volumetric strain reaches a material-dependent critical value. The mathematical form of this criterion is as follows,

$$\int_0^{\varepsilon_{eq}^f} \left(1 + A\frac{\sigma_m}{\sigma_{eq}}\right) d\varepsilon_{eq} = C \qquad \text{Eq. 2.3}$$

where ε_{eq} is equivalent strain and ε_{eq}^{f} is final equivalent strain, A and C are fracture criteria constants, σ_m is hydrostatic stress and σ_{eq} is equivalent stress [25].

2.5.2 Macromechanical Approach to Ductile Failure

The macromechanical approach is involved with calculating the stress and strain fields for all stages during a deformation process until the onset of fracture. The calculated stress and strain fields are then used to predict fracture for a specific combination of stress states, i.e. a specific operation. Various forms of this approach state that fracture occurs when the plastic energy accumulated at a certain point reach a critical value [9]. An example is the Crockroft and Latham criterion for ductile fracture

$$\int_0^{\varepsilon_{eq}^{f}} \sigma_1 d\varepsilon_{eq} = C \qquad \text{Eq. 2.4}$$

where ε_{eq}^{f} is the equivalent fracture strain, C is a fracture criterion constant, σ_1 is the maximum principal tensile stress and $d\varepsilon_{eq}$ is equivalent strain [26]. For an upset test, the principal stress state acts at the centerline with respect to height on the equatorial surface of a sample.

2.6 Assessment of Cold Headability

In order to evaluate the cold heading performance of different materials, one of three mechanical tests is usually carried out to obtain ductility and strength parameters; these are the tensile, upset and impact tests.

2.6.1 Tensile Test

A tensile test involves axial deformation on a machined sample using grips until fracture. It offers advantages in that it is readily accessible, fairly straight forward and provides parameters that give an indication of material strength and ductility by the ultimate tensile stress and total elongation, respectively. However, there are some drawbacks of using the tensile test for evaluating cold headability. Steels used for cold heading have good ductility and fail during tensile testing in a ductile manner after localized deformation (necking). The stress state is initially uniaxial until the onset of necking. At this point, a hydrostatic component of stress is added to the uniaxial component at the neck, thus, increasing the chances of localized failure. As a result, the tensile test does not accurately simulate an industrial cold heading process due to the different stress states in the two tests [26]. In addition, the strain rate in tensile

testing is usually on the order of 10^{-4} to 10^{-2} s^{-1} which is significantly lower than cold heading strain rates [27].

2.6.2 Upset Test

The upset test is performed by applying a compressive load on a cylindrical piece. It is also simple to perform and does not require sophisticated equipment. It simulates stress states undergone during a cold heading process better than in the tensile test due to the similar loading conditions. Lubrication is required during an upset test in order to lower friction and prevent barreling. Kudo *et al.* defined two operative failure modes for materials undergoing an upsetting forming operation [20]. These modes are illustrated schematically in Figure 2.5. Longitudinal cracks on the surface parallel to the loading direction are indicative of the first mode. Reasons for failure in this manner include surface defects, severe anisotropic microstructure or the exhaustion of the tensile ductility of the material and development of high secondary tensile stresses. The second mode is easily categorized by the distinctive shear cracks at a 45° angle from the loading direction. These cracks are the result of reaching the ductility limit after the strength increase associated with strain hardening [20]. A draw back of the upset test is that the strain rates used in the test are on the order of 10^{-2} to 1 s^{-1} and, therefore, do not accurately simulate strain rates during an industrial cold heading operation [27].

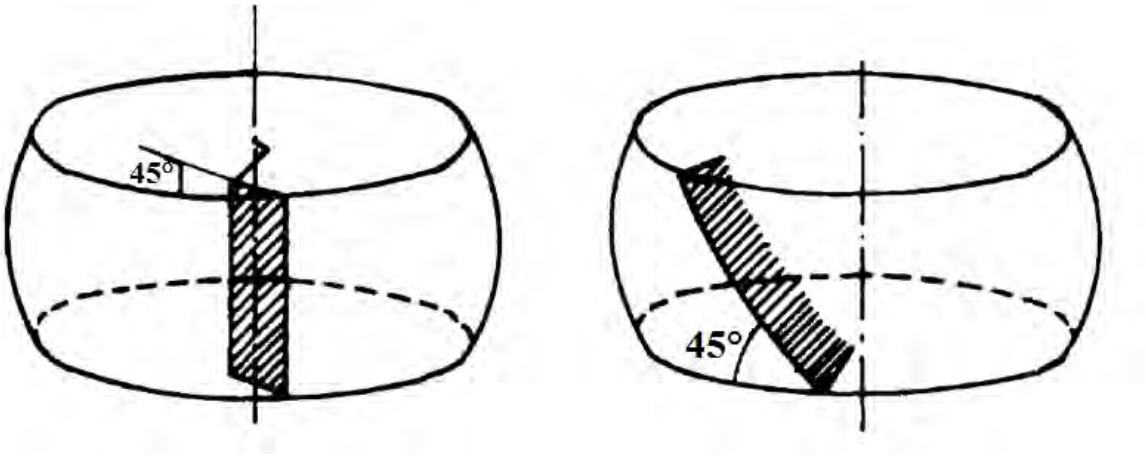

Figure 2.5 Schematic illustrations of compression fracture planes described by Kudo and Asi [20].

2.6.3 Drop Weight Impact Test

In a drop weight impact test, a weight is dropped on the workpiece in order to compress it. This test is capable of high strain rates exceeding 10^{2} s^{-1}. The strain rate and reduction are controlled by changing the dropped weight and the height from which the weight is dropped. The test accurately simulates the loading conditions during an industrial cold heading process and consequently, the stress state during the test [18].

2.7 Shear Banding

Shear banding is a phenomenon that results from work transforming into heat during plastic deformation. For high strain rates, such as in cold heading, the short impact time is not enough for heat to dissipate away from the deformation zone resulting in localized heating or ‘thermal softening’ in the heated zone. This leads to a heterogeneous mode of plastic deformation and the occurrence of shear bands [23].

CHAPTER 3 : EXPERIMENTAL DESIGN AND PROCEDURE

3.1 Purpose of Project and Experimental Approach

The assessment of various factors for improving cold heading performance was done through testing various materials by means of a consistent testing procedure. The different cold heading responses were then analyzed in light of chemical composition, processing and microstructural variations in order to optimize the process. This chapter gives information about the testing method, the materials included in the study and the selected heat-treatment schedules.

3.2 Identification of a Laboratory Cold Heading Test

The selection of a consistent testing methodology was carried out. The test ought to allow for the evaluation of the cold headability and also be appropriate for equipment in the ASPPRC facilities. The largest MTS test frame available had a capacity of 444.8 kN (100,000 lb). A cylindrical specimen geometry was chosen since it is the geometry of commercially cold headed parts. The height to diameter ratio was chosen to be 2, a value less than 2.5 to prevent buckling for steel and larger than 1.5 to simulate commercial processes. After the determination of the sample geometry and height-to-diameter ratio, the task was to determine the sample diameter and corresponding height. A sample diameter which would accommodate sufficient strain without exceeding the force capacity of the available equipment was identified by predicting force-displacement curves for material with assumed strength and strain hardening properties. Based on the analysis detailed in APPENDIX A, the samples were determined to have a diameter of 6 mm and a compressed height of 12 mm in order for a high carbon steel sample to undergo up to 80 pct engineering strain without exceeding the system load capacity.

Identification of a cold heading test also involved selection of a die configuration. Possible options included a typical unsupported upset test, a one-sided supported upset test and a two-sided supported upset test. These configurations are schematically illustrated in Figure 3.1 (a), (b) and (c), respectively. After examination of the choices, it was decided that a one-sided supported upset test (Figure 3.1 (b)) would be used for two reasons. First, the sample geometry resembles typical common commercial cold heading processes. Secondly, it was relatively easy to set up and avoids potential issues with alignment in the case of a two-sided supported upset test. Accordingly, the sample height had to be more than 12 mm to yield an unconstrained compressible height of 12 mm.

The detailed die configuration is shown in Figure 3.2. The upper die was made of 1541 steel. On one side, a drill and tap hole was made with threads to easily screw the upper die into the studs attached to the MTS frame. On the bottom of the upper die, a disk-shaped cavity was made to insert a 55 HRC

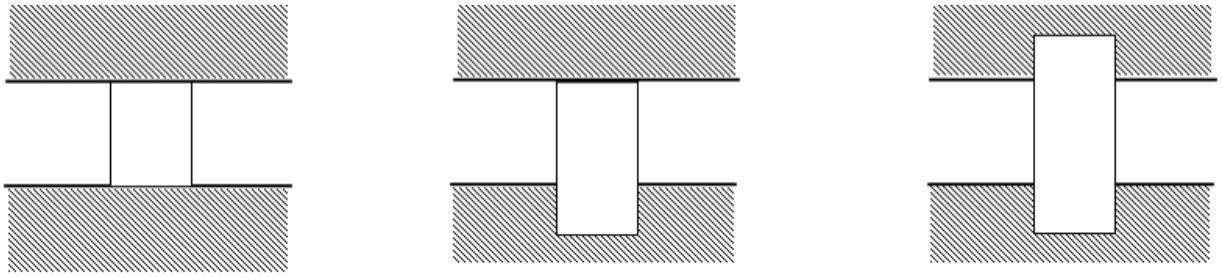

Figure 3.1 Schematic illustrations of the possible variations for a laboratory upsetting test. (a) Unsupported upset test (b) one-sided supported upset test (c) two-sided supported upset test.

hardness calibration block. The purpose for this block was to take on the load when performing a test and if damaged, could be easily replaced. The hardness block is held in place by a thin holder ring screwed into the upper die. The bottom configuration consisted of a die holder which has a cavity on its bottom to insert another hardness calibration block that also serves to take on the load. This cavity was connected to another concentric opening of a smaller diameter on the top for the bottom die which is a cylindrical hard tool steel insert. The bottom die had a 6-mm diameter hole that went from the top to the bottom of the insert for the sample to go into. A hard punch was therefore needed for retrieval of the sample after performing a test. It also served to vary the height to diameter ratio if needed later. This configuration was easy to set up and damaged parts could be selectively replaced at minimum cost. This also meant that the sample height would have to be greater than 12 mm to ensure an unconstrained compressible height of 12 mm. It was deemed appropriate, therefore, that the samples would be of 6-mm diameter and 18-mm height. A punch was accordingly made to have 6 mm of the height of the sample constrained and result in an h/d ratio of 2.

3.1 Material Selection

The main focus of this study was medium carbon steels. Thus, two sets of medium carbon steel alloys were selected for conducting the experiment. Additionally, a set of low carbon steels and a high carbon steel were included in the study. One reason for including the additional steels is to get a broader sense of the cold heading response. Another reason was to obtain actual data points for the schematic plot seen in Figure 3.3. The figure shows the predicted inverse relation between strength and compression limits. Low carbon steels have high ductility (i.e. compression limit) and low strength (hardness) while high carbon steels have high strength but inferior ductility properties. Medium carbon steels lie somewhere in between low and high carbon steels with intermediate strength and ductility properties. It was expected that testing of the as-received materials would produce data points that lie on the curve. Ideally, by pursuing heat treatment options, it would be most beneficial to increase strength without

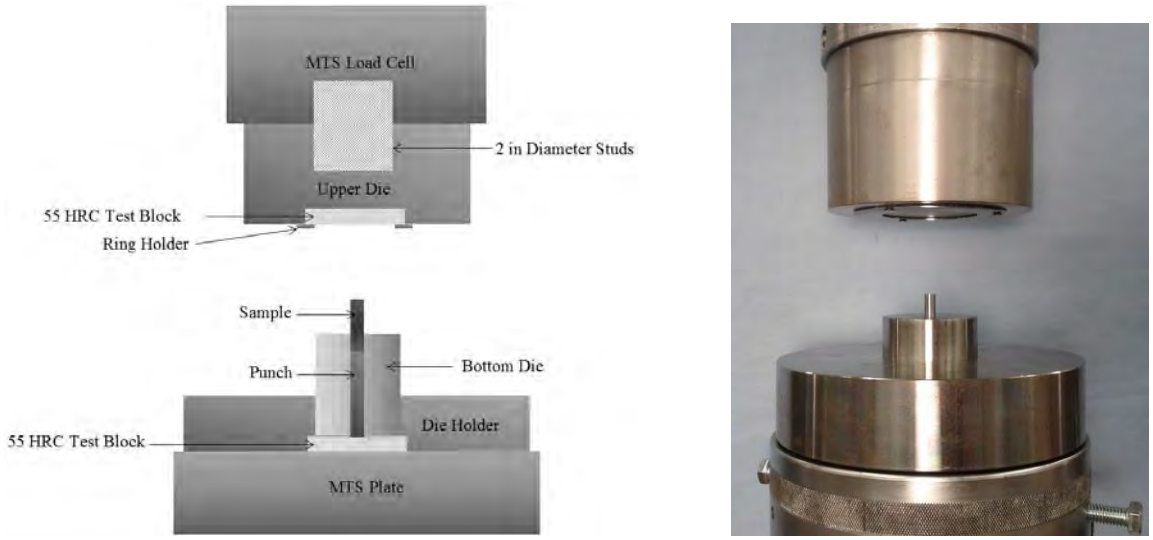

(a) (b)

Figure 3.2 (a) Schematic illustration of the die configuration showing the inner hardness test blocks (b) The actual die configuration.

compromising, ductility. This would be accomplished by moving off the curve to higher hardness values at the same or higher compression limits.

The first set of medium carbon steels consisted of a series of 1045 steels studied previously in the thermomechanical processing study of Mukherjee [28]. The second set was a series of 41XX based alloy steels. Compositions and alloy designations are shown in Table 3.1. The 1045 based steels include three alloys, 1045 Al with 0.02 wt pct aluminum (Al), 10V45 with 0.09 wt pct vanadium (V), 10V45 + niobium (Nb) with 0.09 wt pct V and 0.02 wt pct Nb. Each of the three alloys was provided in the conventional hot-rolled condition and after special thermomechanical processing designed to refine the microstructure by incorporating low finishing temperatures. Summary of the reheating and the finish rolling temperatures could be found in Table 3.2 [28]. The steels have between 0.025 and 0.030 wt pct sulfur (S). These alloys were supplied by Gerdau Macsteel Division as 52 mm diameter bars.

The 41XX based alloys supplied by Bekaert included a 4135, 4140 and a cold heading grade steel designated as PL41. Each alloy was supplied in three conditions: (i) as-rolled wire rod and (ii) pre-drawn wire and (iii) commercially spheroidized wire. The pre-drawn wires were drawn from the as-rolled wire rods and hence, they had smaller diameters as seen in Table 3.3. The pre-drawn wire then underwent a spheroidization heat treatment step for extended periods of time at temperatures below the A1. The 4135 and 4140 alloys differed mostly in carbon (C), Al and copper (Cu) content. The PL41 has comparable carbon content to that of 4140. However, it had no molybdenum (Mo). All three alloys had less than 0.01 wt pct S.

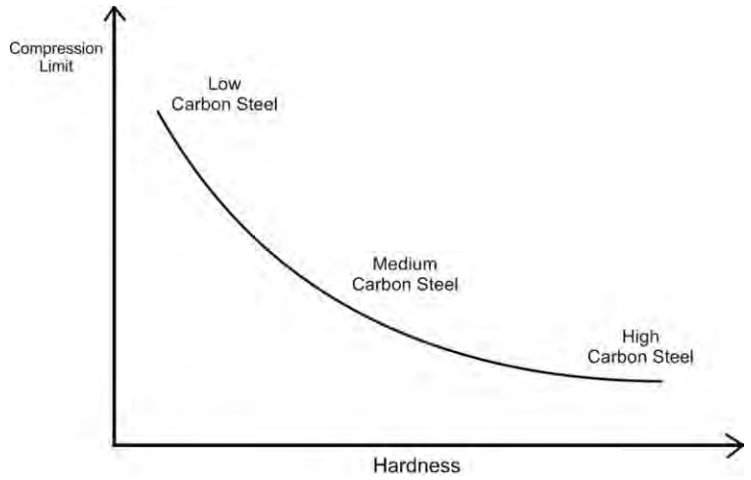

Figure 3.3 Schematic illustration showing the inverse relation between strength (hardness) and ductility (compression limit). Low carbon steels generally have low strength levels and high ductility while the opposite is true for high carbon steels. Medium carbon steels exhibit an intermediate ductility and strength capabilities.

A set of low carbon steels was also included in the study. These were used previously in Schaneman's work [29]. The set consisted of one base chemistry (16MnCr5) and two processing conditions. The first processing condition is hot rolled (HR) where the bar was heated to 1125 °C and finished at 1018 °C. The other processing condition is controlled rolled (CR) where the bar was rolled at 1080 °C and finished at 886°C. These bars were approximately 37.6 mm in diameter. The base alloy had 0.025 wt pct S. The high carbon (1080V) steel was provided by Evraz Rocky Mountain Steel and used in Miller's project with the ASPPRC [30]. It was supplied as an industrially hot rolled coil with a diameter of 12.7 mm. Sulfur content for the steel was 0.007 wt pct.

3.2 Sample Preparation and Machining

Cylindrical samples with a diameter of 6 mm and a height of 18 mm were machined from the as-received (i) 1045 steels, (ii) 41XX steels, (iii) 16MnCr5 steels and (iv) industrially hot-rolled 1080V steel. The tolerance for all machined samples was +/- 0.0254 mm. All samples were machined with a consistent 16G surface finish in order to minimize surface effects. For the 1045 steels, samples were machined from the 52-mm-diameter bars at a consistent distance from the center of the bars (18 mm) to assure consistent microstructures in all samples. For the 41XX steels, samples were machined from the center of the wires. The HR and CR 16MnCr5 samples were machined at a consistent 10 mm away from the center of the bar. Schematic illustrations of where the samples were machined from the as-received bars can be found in Figure 3.4. In addition, heat-treatable samples were rough-machined of the 10V45 w/Nb. The samples

machined for laboratory heat treating were machined with a 19 mm height and a 7 mm diameter. They were also machined at a consistent 18 mm from the center of the circular cross section of the bar.

Table 3.1 - Chemical Compositions of Experimental Steels (wt pct.)

Alloy	C	Mn	Si	Ni	Cr	Mo	Ti
1045 Al	0.45	0.72	0.24	0.08	0.12	0.04	0.001
1045 Al TMP	0.46	0.72	0.24	0.07	0.11	0.03	0.001
10V45	0.45	0.82	0.28	0.07	0.15	0.03	0.001
10V45 TMP	0.48	0.84	0.29	0.07	0.15	0.02	0.001
10V45 w/Nb	0.46	0.85	0.27	0.08	0.14	0.03	0.001
10V45 w/Nb TMP	0.46	0.85	0.27	0.08	0.14	0.03	0.001
4135	0.34	0.74	0.26	0.015	0.93	0.16	-
4140	0.41	0.75	0.22	0.015	0.93	0.16	-
PL41	0.40	0.76	0.24	0.02	1.07	-	0.0045
16MnCr5	0.18	1.13	0.21	0.01	1.05	0.04	-
1080V	0.79	0.70	0.25	0.07	0.15	0.015	0.001

Alloy	Nb	V	Al	N	S	P	Cu
1045 Al	0.001	0.003	0.021	0.0097	0.025	0.010	0.13
1045 Al TMP	0.001	0.003	0.019	0.0102	0.025	0.008	0.13
10V45	0.001	0.084	0.000	0.0127	0.027	0.011	0.15
10V45 TMP	0.001	0.094	0.000	0.0131	0.029	0.013	0.14
10V45 w/Nb	0.020	0.092	0.000	0.0124	0.030	0.018	0.16
10V45 w/Nb TMP	0.020	0.092	0.000	0.0124	0.030	0.018	0.16
4135	-	-	0.0249	0.0053	0.0086	0.0120	0.0172
4140	-	-	0.0470	0.0031	0.0077	0.0133	0.0237
PL41	-	-	0.0264	0.0024	0.0100	0.0141	0.0276
16MnCr5	-	-	0.029	-	0.025	0.015	0.16
1080V	0.00	0.03	0.003	0.0077	0.007	0.009	0.21

Table 3.2 – Summary of Reheat and Finish Rolling Temperatures for the 1045 Base Steels

Material	Reheat Temperature (°C)	Finish Rolling Temperature (°C)
1045 Al	1197	997
1045 Al- TMP	1220	791
10V45	1202	1008
10V45-TMP	1218	796
10V45 w/Nb	1216	1027
10V45 w/Nb TMP	1220	811

Table 3.3 – Wire Diameters of the 41XX Series Alloys in The As-received Condition

Alloy	Wire Rod Diameter (mm)	Pre-drawn wire diameter (mm)	Spheroidized Diameter (mm)
4135	8.00	6.53	6.53
4140	11.50	9.02	9.02
PL41	10.50	7.93	7.93

3.1 Testing Parameters

In the initial stage of testing, three principal deformation speeds were employed in the study. Since all samples effectively have the same geometry and dimensions, these speeds translated into three strain rates. The speeds were 0.15 mm/s, 1.5 mm/s and 15 mm/s which result in initial imposed engineering strain rates of $1.25x10^{-2}\ s^{-1}$, $1.25x10^{-1}\ s^{-1}$ and $1.25\ s^{-1}$, respectively. These are referred to as slow, medium and fast strain rates, respectively. Note that the maximum imposed velocity is about 80% of the peak velocity available for the MTS system. The variables in testing are strain rate and the amount of imposed strain. Prior to testing, sample measurements recorded included sample total height, diameter and unconstrained height.

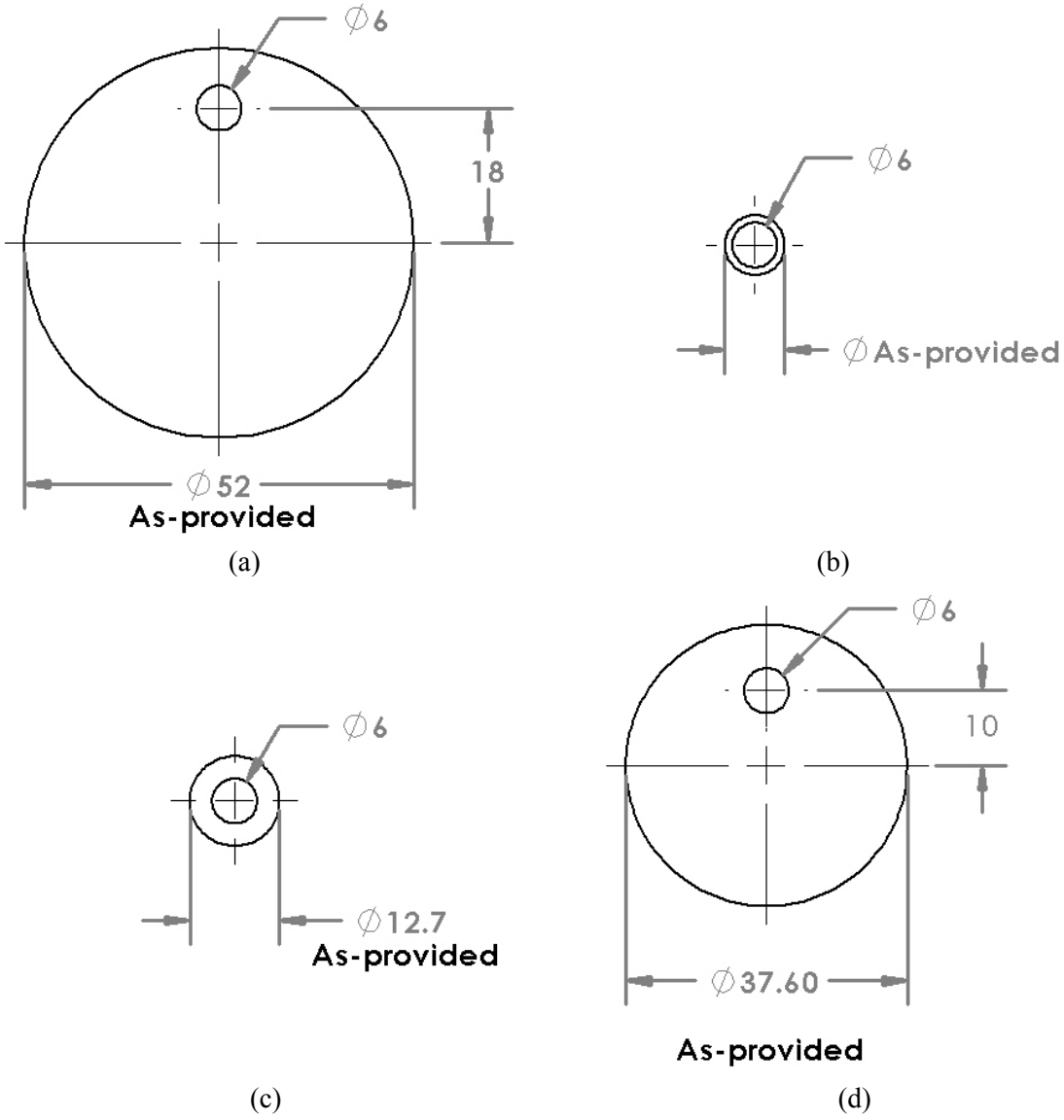

Figure 3.4 Schematic illustrations of where samples are machined with respect to the as received materials cross sections. Dimensions are in mm. (a) 1045 alloys (b) 41XX alloys (c) 1080V (d) 16MnCr5.

In the second stage of testing, the highest strain rate were exclusively used in testing since varying strain rate did not result in a notable improvement or difference in the cold heading performance (see section 4.2 Effects of Strain Rate Variation). From that point on, only the 15 mm/s speed was exclusively used in testing. Also, lubrication was shown to result in an asymmetrical deformation behavior and therefore, samples were all wiped with acetone prior to each test to assure the removal of residual oils from the machining process and hence, consistent friction conditions. The controlled parameter in testing was the amount of imposed strain. Each set of samples was tested to define a fracture

limit that allows for comparison of tested materials. To achieve this, samples were tested at approximately 2.5 pct engineering strain increments until no cracks are detectable by the procedure prescribed in the following section. This level of strain is, then, referred to as the fracture limit for the material. All tests were performed at room temperature.

3.2 Testing Procedure

Several preliminary tests were run to evaluate the effects of lubrication and establish a consistent and reproducible test procedure. Results on the lubrication tests are presented in the next chapter. The final test procedure consisted of the following steps after inserting the sample in the lower die:

1- Preload to low force significantly below yielding to 'seat' all parts and establish a reference point for displacement measurement and control.
2- After preloading, the load cell (top configuration) and the actuator (bottom configuration) were separated by a distance sufficient to allow the actuator get to the specified speed before loading.
3- Samples were wiped with acetone to increase friction. The reason for acetone wiping is that lubrication proved to cause unstable deformation behavior that resulted in asymmetrically deformed samples. (See results section on lubrication effects)
4- The control program was set up by inputting the final desired height (i.e. imposed compressive strain). The final height was entered into the machine with reference to the zero displacement point defined during preloading.
5- Samples were compressed to the specified height, held for five seconds and then released. This was performed consistently on all samples.
6- Compressive and circumferential strains were calculated based on pre- and post-testing measurements.

After testing, samples were removed from the lower die with a punch and a manual laboratory hydraulic press. Samples were measured to determine the actual imposed compression and imposed circumferential strains. Compressed samples were also evaluated in a stereomicroscope to assess type and degree of surface cracking. Standard macrophotographic techniques were used to record the observations.

3.3 Metallography and Material Characterization

Longitudinally and transversely sectioned samples were prepared by grinding, polishing and etching in a 2 pct nital solution of as-received materials and heat-treated materials. All Vickers hardness data were obtained from transverse sections perpendicular to the rolling direction. A 500 gmf load and a standard 10 second dwell time were used for all hardness data. All micrographs taken for material

characterization purposes were taken on longitudinally sectioned samples parallel to the rolling direction. The etchant of all metallographic samples was 2 pct nital unless another etchant is indicated.

3.4 Fractography and Fracture Evaluation

After each sample was tested, it was visually inspected for cracks under a stereo microscope at 20X. If a crack is visible, the sample is considered cracked even if the cracks are not visible with the naked eye. The cracks may not be critical from a practical application standpoint but provide a method for evaluating cold headability. A fracture limit with respect to true compressive strain was then defined for each material. At the fracture limit strain or smaller strains, no cracks were observed. Figure 3.5 is a stereo microscope macrograph at 20X of a 10V45 w/Nb sample containing examples of 'incipient' cracks. These cracks are observed frequently at strains slightly above fracture limits. The smallest cracks observed by this method of evaluation were approximately 0.04 mm long and 0.01 mm wide. Defining fracture limits allowed for comparisons of relative formabilities of the different materials with respect to chemical composition, processing history, inclusion content or other variables. Additionally, the type of cracking (shear or longitudinal), the degree of cracking (low, medium or high) were also noted.
An environmental scanning electron microscope (ESEM) was used to conduct fractography on representative cold-headed samples of the 1045 series, 41XX series, 16MnCr5, 1080V and heat-treated 10V45 w/Nb materials. Samples were placed as-tested in the ESEM and images were captured from inside the cracks. In addition, representative samples of the as-received 1045 materials and 10V45 w/Nb materials were mounted, ground to about halfway through the upset height, polished and etched to reveal the microstructure around observed cracks. Additionally, macrographs were taken at three levels of strain for all as-received and heat-treated materials unless samples were not available for a certain level of strain. This was done to get a sense of the relative worsening of crack severity with increasing strain for each material and to be able to compare different materials irrespective of the fracture limit.

3.1 Examining Flow Behavior

Two cold-headed 1045 Al samples of different reductions were sectioned parallel to the loading axis. These samples were then polished and macroetched in a solution of 50 pct volume hydrochloric acid and 50 pct volume deionized water at a range of temperature between 70 and 80 °C for approximately 10 minutes. Macroetching was performed to reveal the large-scale strains and gain an appreciation for the deformation behavior resulting from the developed procedure.

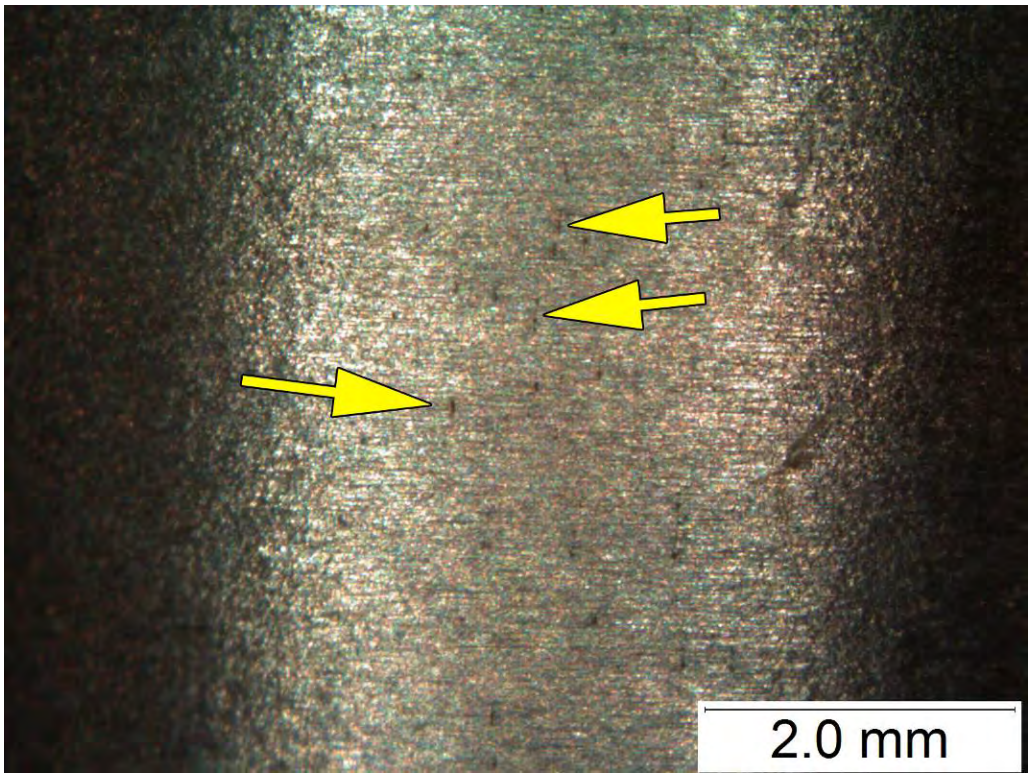

Figure 3.5 Stereo microscope macrograph of a quenched and tempered 10V45 w/Nb sample at 20X. Arrows point to examples of what are considered 'incipient cracks' in the context of this work.

3.2 Heat Treatment Procedure

Heat treatable samples were rough-machined of the conventionally hot-rolled 10V45 w/Nb alloy. The alloy was selected for heat treatment due to its equiaxed starting microstructure and its unique vanadium and niobium alloying. Carbolite air furnaces and salt pots in the ASPPRC facilities were used to carry out the heat treatments with the exception of isothermally-transformed sets. Preliminary heat treatments were done on 10V45 w/Nb samples to determine the extent of the decarburization response. It was of interest to test the cold heading response of a homogeneous microstructure throughout the sample as opposed to a microstructure with a decarburized layer that could possibly give a false impression of cold headability by having a softer ferritic microstructure where the stress was highest during cold heading. In the most severe case for the trials, the decarburized layer was found to be approximately 250 μm in depth. Note, the preliminary tests were done by placing samples in the furnace without any precautions to minimize decarburization. Therefore, samples were rough machined with an additional 500 μm at the surface to provide a factor of safety. Thus, the heat-treatable samples are 7 mm diameter by

19 mm height. After heat treatment, samples were machined to final dimensions (6 mm diameter by 18 mm height).

For austenitization heat treatment steps that involve air cooling (normalizing steps) and tempering steps, sample sets were heat treated in stainless steel bags, argon was blown into the bags, and a coupon of titanium was placed with the samples. The reason for doing this is to minimize decarburization as argon displaces air inside the bag and titanium limits the contact of oxygen with the steel due to the high affinity of titanium for oxygen. After heat-treatment, air cooled samples were removed from the bag and shaken in a stainless steel screen until they reached room temperature to ensure a consistent cooling for all samples at all sides of each sample. Heat treatment schedules that involve a critical quenching step were done in a refractory flask. That is due to the difficulty of removing samples from a stainless steel bag and quenching fast enough to ensure the intended transformation. The flask contained charcoal at the bottom and a stainless steel screen separating the charcoal from the samples. Placing charcoal inside the flask limited the reaction of oxygen in air with the carbon in the steel. Samples were placed inside the flask on top of the screen and the flask was covered with a flat steel sheet. After heat-treatment, the cover sheet was removed and samples were dipped in the quenching medium.

Heat treatment schedules for bainitic microstructures involve an isothermal hold at an intermediate temperature after austenitization. A rapid cool from the austenitization temperature to the isothermal hold temperature is critical in order to achieve the intended transformation. Therefore, bainitic microstructures are heat treated in salt pots with the capacity to cool samples from the austenitization temperature to the isothermal hold temperature instantaneously after austenitization

3.3 Heat Treatment Schedules of 10V45 w/Nb

Spheroidized microstructures were of interest due to their high formability properties and therefore, their wide use for cold heading applications. Results on the samples were coupled with the same alloys with the as-received ferritic-pearlitic microstructures would also allow for comparing the fracture limits for the as-received materials with a spheroidized one. To attain a uniform distribution of spheroidized carbides, samples were heated to 1000 °C for 60 minutes and then water quenched. Spheroidization was then done by heating to 700 °C for 48 hours.

An aging study was proposed that would enable evaluating aging as an option to increase strength of cold headed parts. Comparing the strength and fracture limits for sample sets aged at different aging temperatures could help achieve that goal. A preliminary aging experiment was performed on as-received 10V45 w/Nb samples. The samples were normalized by heating to 1000 °C for 60 minutes to thoroughly dissolve niobium and vanadium, air cooled and then aged at temperatures between 575 °C and 675 °C at 25 C increments for 60 minutes. It was observed that an increase in hardness occurred at around 625 °C

while aging at 675 °C causes a drop in hardness. Therefore, three sample sets were normalized by heating to a 1000 °C followed by air cooling. One sample was tested as-normalized and the second set was aged at 625 °C and the third set was aged at 675 °C. This allowed for the assessment of aging as an option for increasing the strength of cold heading steel without compromising formability.

Bainitic microstructures are increasingly being used in cold heading applications and have the potential to eliminate the post-forming heat treatment. Therefore, two isothermally-transformed sample sets were heat treated to evaluate the performance of the microstructures for cold heading applications. The two sets were austenitized at 866 °C for 10 minutes and then one set was rapidly cooled to 435 °C and the other to 365 °C to create two different microstructures with a hardness difference. In addition, two quenched and tempered sets were heat treated by austenitizing at 870 °C for 10 minutes and water quenching. The resultant microstructure at this point was fully martensitic. The two sets were then tempered at 615°C and 590 °C for two hours. These temperatures were selected after trials as an attempt to match the hardness of the quenched and tempered sets with the bainitic sets and compare cold headability of the differently processed microstructures of the same hardness. All the heat treatment schedules are summarized in Table 3.4.

3.4 Inclusion Analysis

An inclusion analysis was carried out on as-received 1045 materials, hot-rolled 4135, CR 16MnCr5 and 1080V. The analysis was done on an automated optical microscope program used to assess quality of industrially produced steels in Evraz North America's facilities in Pueblo, CO. The analysis was done by scanning a ground and polished area composed of 200 frames at 200X and autofocusing every 5 frames. Data extracted from the analysis identified sulfides based on color contrast. The data also provided a count of the inclusions, size and aspect ratio.

Table 3.4 - Heat Treatment Schedules of 10V45 w/Nb

Desired Microstructure	Procedure
Spheroidized	Heat to 1000 °C for 60 minutes. Water quench. Heat to 700 °C for 48 hours. Air cool.
Normalized	Heat to 1000 °C for 60 minutes. Air cool.
Normalized and Aged	Heat to 1000 °C for 60 minutes. Air cool. Heat to 625 °C for 60 minutes. Air cool.
Normalized and Over-aged	Heat to 1000 °C for 60 minutes. Air cool. Heat to 675 °C for 60 minutes. Air cool.
High Temperature Isothermal Hold	Heat to 866 °C for 10 minutes. Rapid cool to 435 °C and hold for 20 minutes. Air cool.
Low Temperature Isothermal Hold	Heat to 866 for 10 minutes. Rapid cool to 365 °C and hold for 20 minutes. Air cool.
Quenched and High-Temperature Temper	Heat to 870 °C for 10 minutes. Water quench. Heat to 615 °C for 120 minutes. Water quench.
Quenched and Low-Temperature Temper	Heat to 870 °C for 10 minutes. Water quench. Heat to 590 °C for 120 minutes. Water quench.

CHAPTER 4 : RESULTS

4.1 Introduction

This chapter presents experimental results for this project. First, testing methodology results are presented which include the effects of lubrication and reproducibility. Secondly, materials characterization work is presented for the as-received materials and then the heat-treated materials. After that, the effects of deformation speed variations, which were evaluated in the initial stage of testing, are overviewed. A close look is then taken at fracture limits as defined by the procedure detailed in the previous chapter for the as-received materials and then the heat-treated materials. After that, stress-strain curves from as-received and heat-treated materials and the grain flow pattern from the developed procedure are discussed. Fractography and metallography on cold-headed samples results are then summarized. Lastly, results of an inclusion analysis for selected materials are presented.

4.2 Testing Procedure

The developed test procedure was evaluated in terms of effects of lubrication and reproducibility. These results are discussed in the following subsections.

4.2.1 Effects of Lubrication

Initial tests designed to assess the effects of lubrication on material behavior in the laboratory upsetting test were performed with an LPS 1 Premium Lubricant on as-received 1045 Al samples. These tests showed that the application of a lubricant on the sample and the upper platen resulted in an asymmetrical deformation behavior. The extent of the deformation asymmetry is greatly associated with strain rate. Figure 4.1 compares the deformation behavior in lubricated samples deformed using the low, medium and high displacement rates introduced in Chapter 3. In the figure, axisymmetric deformation can be seen in the sample tested at the low strain rate but significant asymmetry in the samples tested at the medium and high strain rate. Methods to eliminate the potential for asymmetric deformation included lowering the h/d ratio or modifying friction. While successful, lowering the h/d ratio was determined to be an unacceptable solution since this approach would limit the maximum imposed strain. The alternative was the removal of all residual oil from the machined sample and upper die which resulted in symmetric deformation at all speeds. Therefore, it was decided to study the cold heading response of different materials under consistent friction conditions assured by acetone wiping of both the sample and the upper platen.

4.2.2 Reproducibility

The test methodology put forward in the previous chapter proved to be reproducible in terms of the load-displacement response. Testing was done using duplicate sample sets in initial testing for each combination of strain and strain rate until reproducibility was well established. Figure 4.2 contains load-displacement (Figure 4.2 (a)) and true stress-strain (Figure 4.2 (b)) plots for 1045 Al and 1045 Al-TMP samples. The figure shows excellent reproducibility of the load-displacement data between tests.



Figure 4.1 Image of 1045 Al samples tested with the application of an oil lubricant. The samples were tested (from left to right) using the slow, medium and fast speeds. The unstable mode of deformation is clear in samples compressed with the medium and high strain rates.

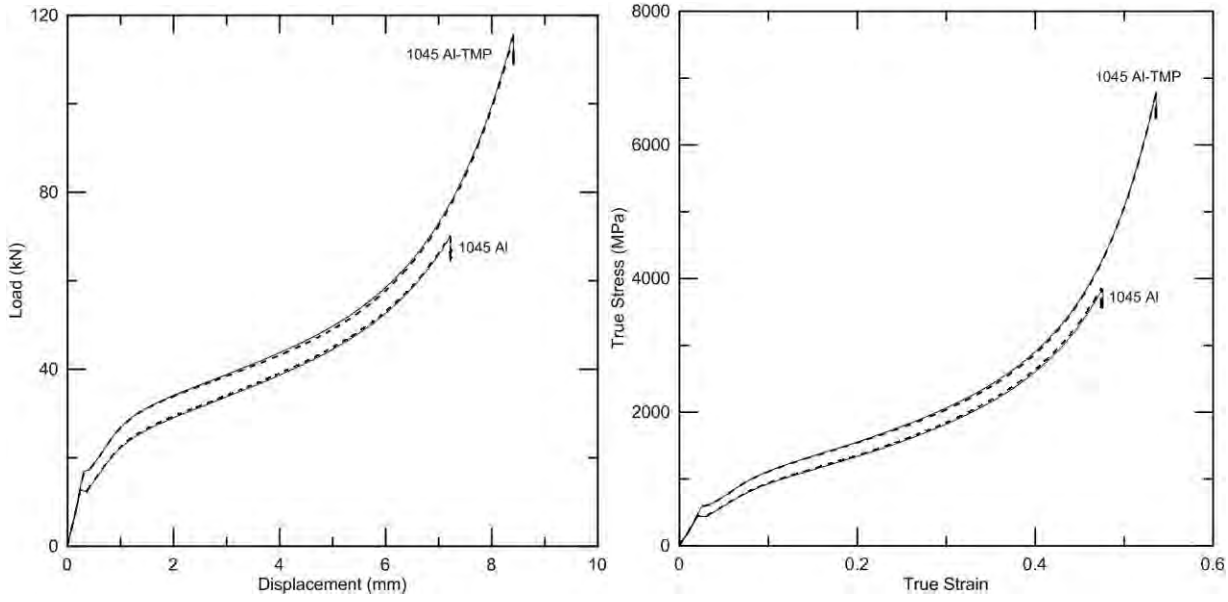

(a) (b)

Figure 4.2 (a) Load-displacement and (b) true stress-strain curves for duplicate sample sets of 1045 Al and 1045 Al-TMP tested with the medium strain rate (1.5 mm/s) to the indicated displacement/strain. Each set is represented with thin solid and bold dashed lines for the first and duplicate sample, respectively. The curves are not corrected for machine stiffness.

4.3 Characterization of As-received Materials

Metallographic samples were prepared from machined samples of the as-received 1045 series materials to examine the microstructure. Figure 4.3 is a series of light optical micrographs from longitudinal cross-sections of the six materials. Longitudinal cross-sections were chosen for metallographic purposes to reveal any directionality of the microstructure or elongated inclusions with respect to the direction of rolling. Microstructures consisted of pearlite colonies surrounded by proeutectoid ferrite outlining the prior austenite grains. Manganese sulfide inclusions elongated in the rolling direction were observed in all 1045 microstructures. In many instances, intragranular idiomorphic ferrite was observed to surround elongated manganese sulfide inclusions. A mechanism for preferential ferrite nucleation around the manganese-depleted regions surrounding MnS inclusions was proposed by Krauss [13]. Conventionally hot-rolled materials mostly exhibited an equiaxed morphology with the occasional exception of ferrite bands surrounding MnS inclusions. Low finish rolling temperatures (i.e. thermomechanical processing) resulted in the elongation of the proeutectoid ferrite in the direction of rolling for the three alloys which proved to be associated with austenite pancaking. This happened to a lesser extent in 1045 Al TMP which exhibited a more equiaxed morphology than 10V45 TMP and 10V45 w/Nb TMP. Notable differences between the three alloys were mainly in volume fractions and colony sizes of the microconstituents.

Table 4.1 details the constituent volume fractions in each material. Proeutectoid ferrite volume fraction measurements were performed by placing a 10x10 grid on three optical micrographs taken randomly at 100X for each material and counting the intercepts that lie in the proeutectoid ferrite. It was assumed that the microstructure consists of only ferrite and pearlite and therefore, the remaining intercepts lie in the pearlite. For the 1045 Al alloy, thermomechanical processing resulted in refinement of the microstructure, some directionality in morphology and an increase in the ferrite volume fraction from 34 to 50 pct. For the 10V45 alloy, a low finish rolling temperature resulted in a severe directionality in microstructure, some refinement of proeutectoid grains and pearlite colonies and an increase in proeutectoid ferrite volume fraction from 35 to 43 pct. For the 10V45 w/Nb alloy, low finish rolling temperature also resulted in a severe directionality of microstructure but a very notable increase in proeutectoid volume fraction. By comparing the three hot rolled materials, ferrite volume fraction was essentially the same for the three materials. However, for the thermomechanically-processed materials, ferrite volume fraction is highest in 10V45 w/Nb TMP at 60 vol pct, 50 vol pct in 1045 Al TMP and the lowest in 10V45 TMP at 43 vol pct.

Metallographic samples were also prepared from as-received 41XX wires for microstructural examination. Figure 4.4 through Figure 4.6 are a series of light optical micrographs prepared from longitudinally sectioned wires of the 4135, 4140 and PL41 materials, respectively. Hot-rolled 4135

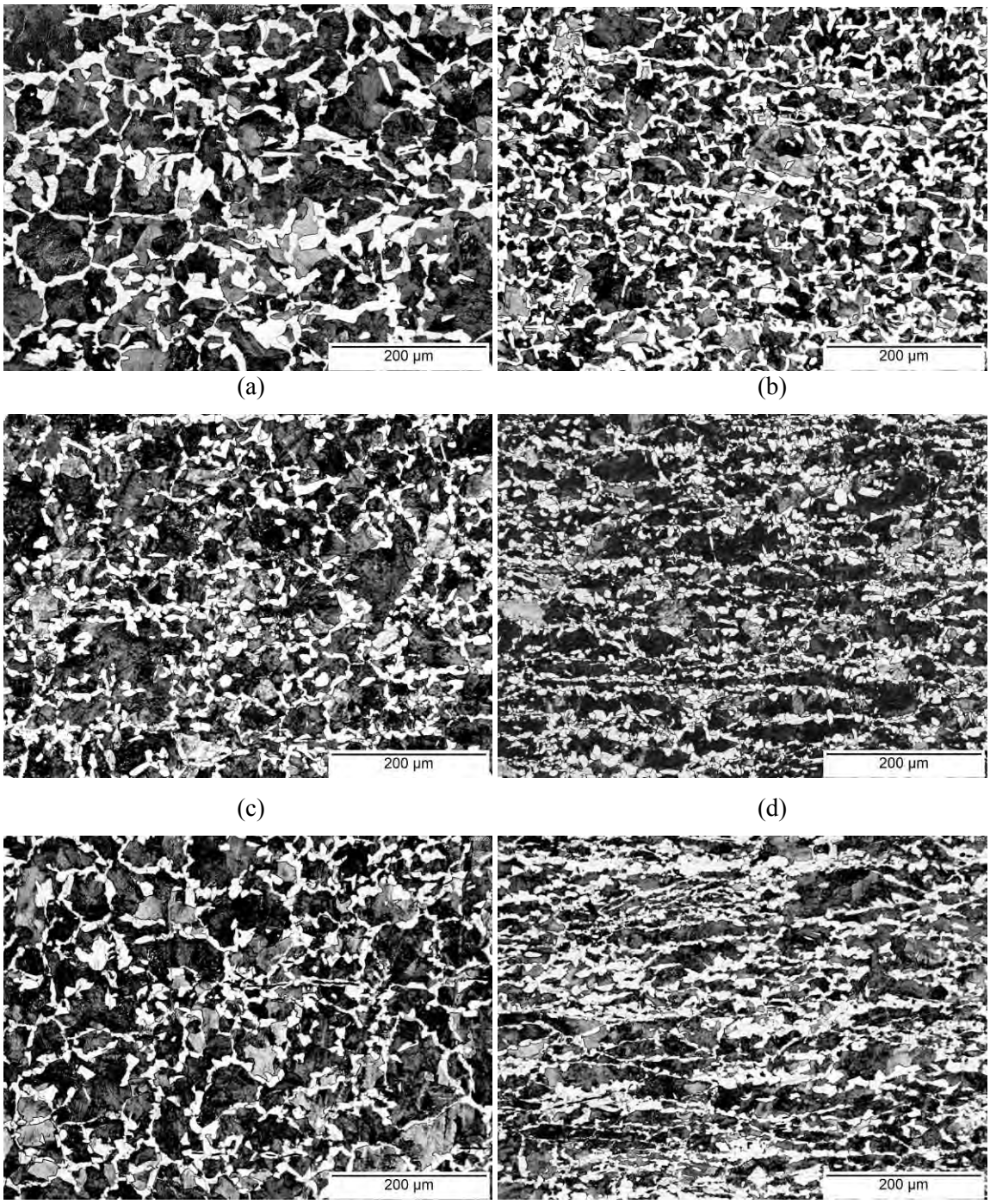

Figure 4.3 Light optical micrographs of longitudinal sections of 1045 series materials. The direction of rolling is horizontal. (a) 1045 Al, HV=218 (b) 1045 Al, TMP HV=196 (c) 10V45, HV=255 (d) 10V45 TMP, HV=259 (e) 10V45 w/Nb, HV=275 (f) 10V45 w/Nb TMP, HV=247. Etchant is 2 pct nital.

Table 4.1 – Summary of Volume Fraction Data for 1045 Materials

Material	Proeutectoid Ferrite (vol pct)	Pearlite (vol pct)
1045 Al	34	66
1045 Al- TMP	50	50
10V45	35	65
10V45-TMP	43	57
10V45 w/Nb	35	65
10V45 w/Nb TMP	60	40

consisted of a duplex microstructure in which proeutectoid ferrite, acicular ferrite, bainite and possibly pearlite and retained austenite are present. The microstructure of hot-rolled 4140 consisted of limitedamounts of proeutectoid ferrite, acicular ferrite and bainite. The amount of bainite was higher in hot-rolled 4140 than 4135 as apparent from the darker etching areas. Pre-drawn 4135 and 4140 were similar to their hot-rolled counterparts as no heat-treatment was undergone. However, microstructural features were elongated along the direction of drawing. The microstructure of hot-rolled and pre-drawn PL41 consisted of proeutectoid ferrite and pearlite. Directionality was observed in hot-rolled and pre-drawn materials but to a greater extent in pre-drawn materials. The directionality was especially severe in pre-drawn PL41 as seen in Figure 4.6 (a) and (b). The spheroidized 41XX steels all had completely spheroidized microstructures that are entirely distinct from the original (pre-drawn) microstructures.

Figure 4.7 (a) and (b), respectively, are light optical micrographs of the hot-rolled (HR) 16MnCr5 steel and the control-rolled (CR) 16MnCr5 steel. The HR microstructure consisted of proeutectoid ferrite (16 vol pct), bainite or possibly Widmanstatten ferrite and few pearlite colonies. In contrast, the CR microstructure consisted of a higher volume of proeutectoid ferrite (47 vol pct) and pearlite.
Figure 4.8 contains SEM micrographs at two magnifications of the 1080V steel. As can be seen in Figure 4.8, the microstructure consist primarily of pearlite with limited amounts of proeutectoid ferrite.

4.1 Characterization of Heat-treated Materials

Figure 4.9 through Figure 4.14 show light optical micrographs of all heat-treated materials. Figure 4.9 shows low and high magnification micrographs of the same area of the spheroidized 10V45 w/Nb sample. The micrographs show a completely spheroidized microstructure. The spheroidized material has a Vickers hardness of 194 compared to 275 for the as-received 10V45 w/Nb condition. Figure 4.10 (a), Figure 4.10 (b) and Figure 4.10 (c), respectively, show the normalized, normalized and aged, and normalized and over-aged conditions of the 10V45 w/Nb alloy. The microstructures all

consisted of pearlite colonies surrounded by proeutectoid ferrite outlining the prior austenite grain boundaries. The

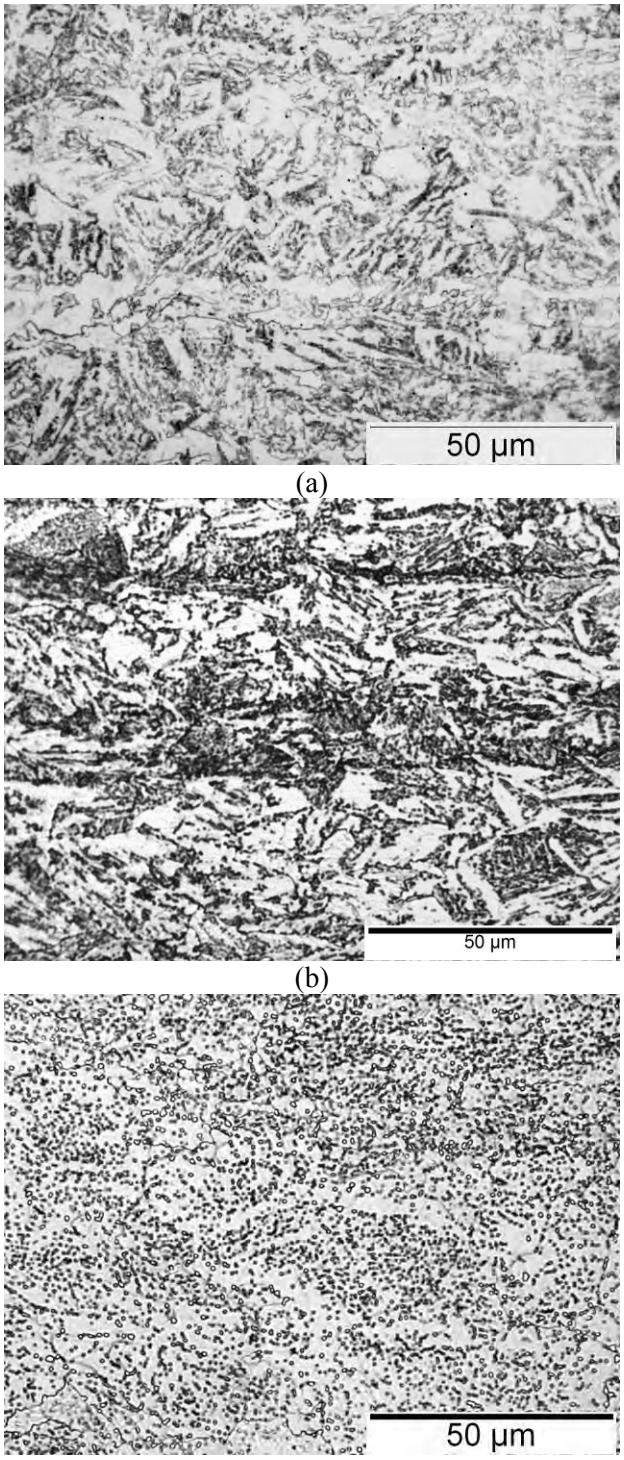

Figure 4.4 Light optical micrographs of longitudinal sections for the 4135 materials. The direction of rolling is horizontal. (a) Hot-rolled 4135, HV=299 (b) pre-drawn 4135, HV=277 (c) spheroidized 4135, HV=195. Etchant is 2 pct nital.

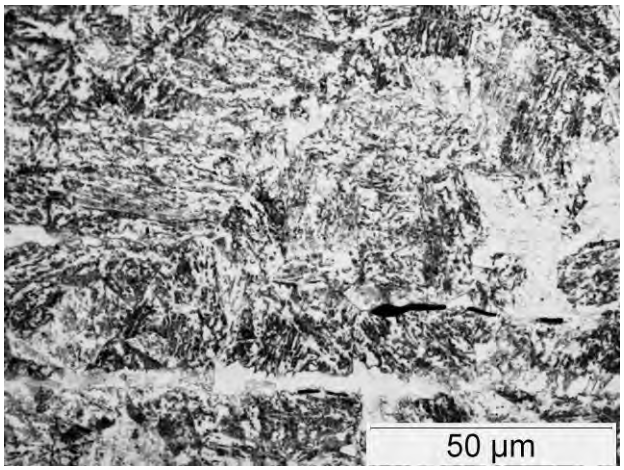

(a)

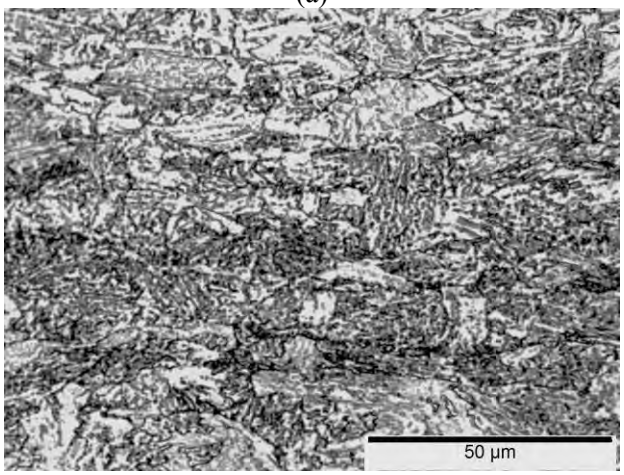

(b)

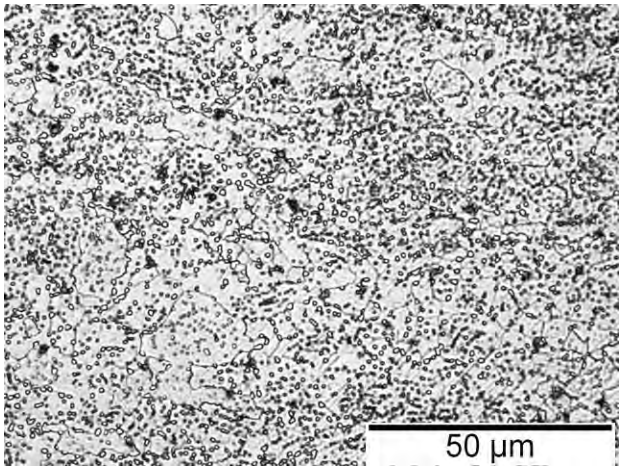

(c)

Figure 4.5 Light optical micrographs of longitudinal sections for the 4140 materials. The direction of rolling is horizontal. (a) Hot-rolled 4140, HV=319 (b) pre-drawn 4140, HV=290 (c) spheroidized 4140, HV=195. Etchant is 2 pct nital.

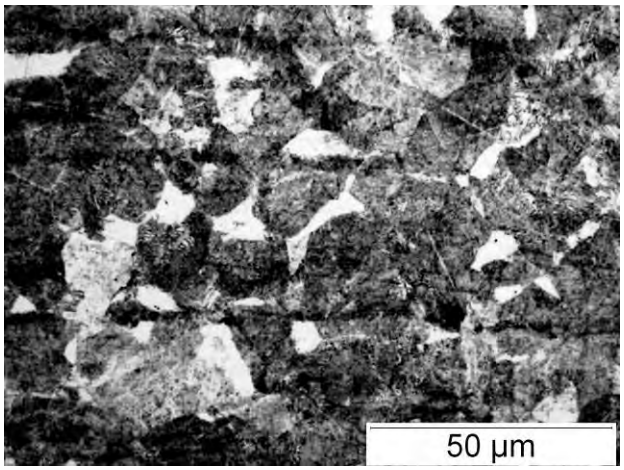

(a)

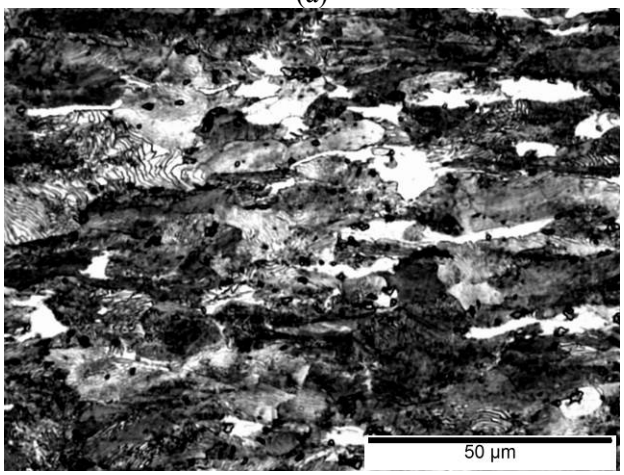

(b)

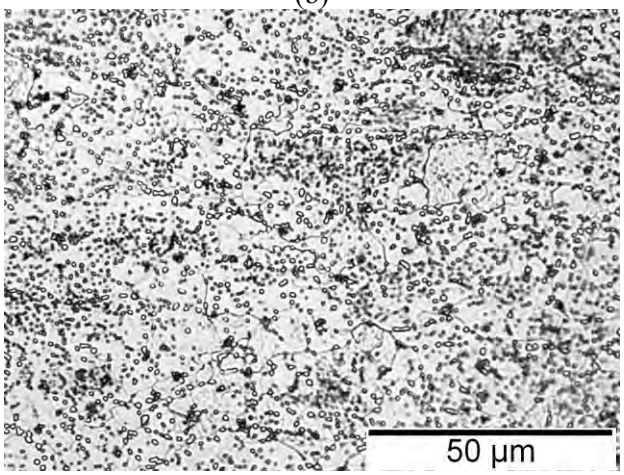

(c)

Figure 4.6 Light optical micrographs of longitudinal sections for the PL41 materials. The direction of rolling is horizontal. (a) Hot-rolled PL41, HV=255 (b) pre-drawn PL41, HV=315 (c) spheroidized PL41, HV=155. Etchant is 2 pct nital.

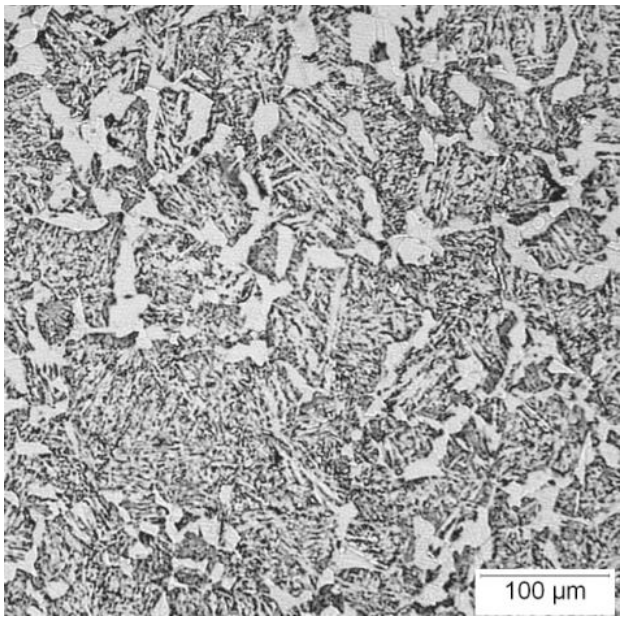

(a)

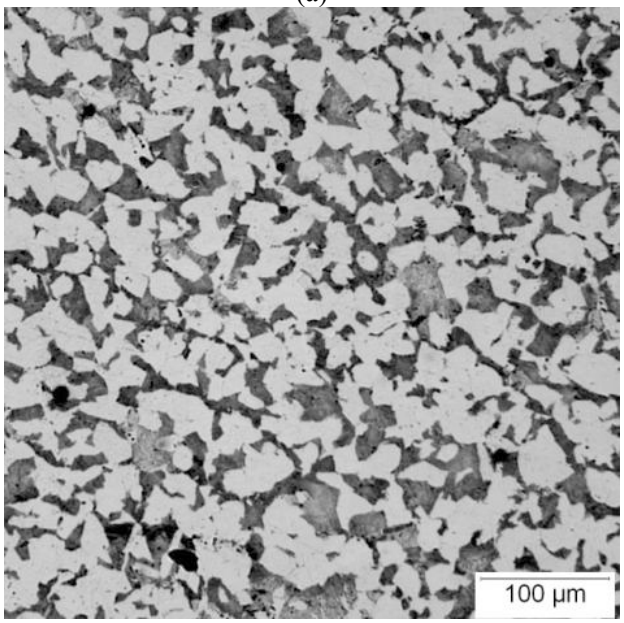

(b)

Figure 4.7 Light optical micrographs of low carbon materials. (a) Hot-rolled (HR) and (b) control-rolled (CR)16MnCr5 materials HV= 220, 189 for (a) and (b), respectively. Etchant is picral acid [29].

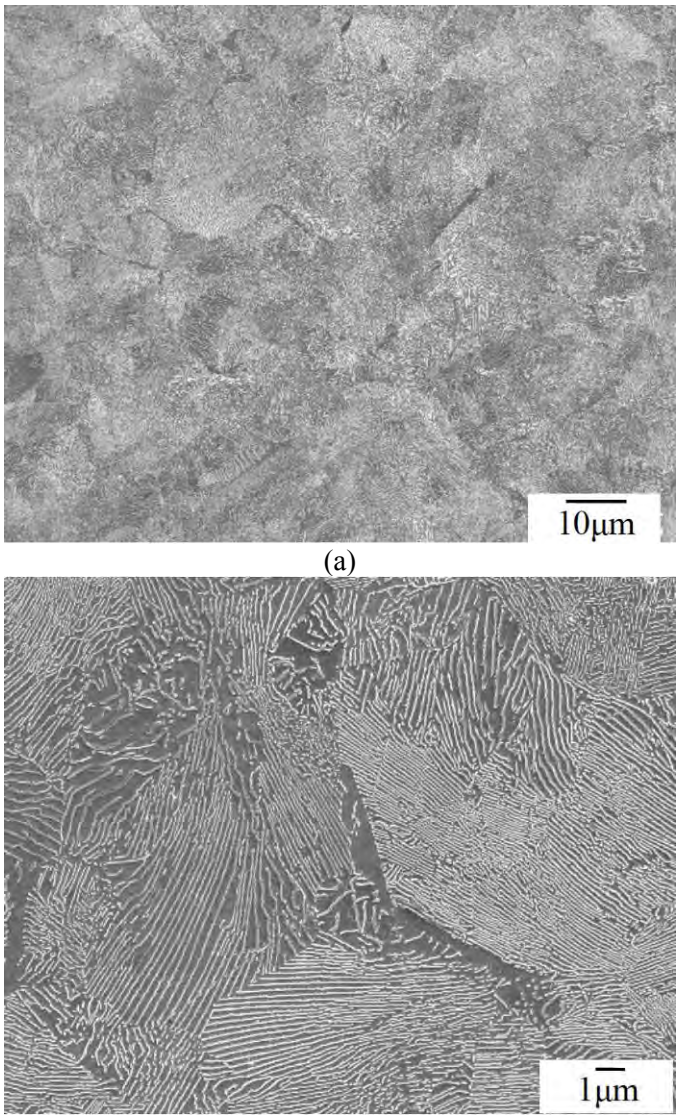

Figure 4.8 SEM micrographs at (a) low magnification and (b) high magnification of 1080V material. HV= 361 [30].

prior austenite grain size, as delineated by the proeutectoiod ferrite surrounding pearlite colonies, was significantly finer for the three conditions than the as-received material (Figure 4.3 (e)). Elongated inclusions were present in all the microstructures even if not visible in the selected micrographs. Vickers hardness for the normalized, normalized and aged, and normalized and over-aged samples were 292, 292 and 262, respectively.

Figure 4.11 and Figure 4.12, respectively, show light optical micrographs at two magnifications of the 10V45 w/Nb austenitized and isothermally-transformed at a high temperature (435 °C) or low temperature (365 °C). The microstructure of the sample processed at a high isothermal hold temperature (Figure 4.11) consisted of a mixture of bainite, proeutectoid ferrite and pearlite colonies. On the other

hand, the low isothermal hold condition microstructure was bainitic as seen in Figure 4.12. Elongated inclusions were observed in both isothermally-transformed microstructures. Vickers hardness values for the higher and lower isothermal hold sets were 303 and 322, respectively. Figure 4.13 and Figure 4.14, respectively, show, at two magnifications the quenched and tempered 10V45 w/Nb samples tempered at 615 °C and 590 °C. The microstructures were similar to each other and are composed of a heavily tempered martensite. The microstructures were distinctly different from the original martensitic microstructure. Elongated inclusions were found in both microstructures. Vickers hardness for the quenched and higher-temperature temper and quenched and lower-temperature temper were 304 and 320, respectively.

4.2 Effects of Strain Rate Variation

The effects of displacement rate on the load displacement data are illustrated in Figure 4.15 for the 10V45 w/Nb steel deformed at 0.15 mm/s, 1.5 mm/s and 15 mm/s. All samples were tested after cleaning in acetone to remove residual oil from the machining process. As shown in Figure 4.15, the complete load-displacement curves, the general shape of the curves were similar. However, as shown in the magnified view of the load displacement data in Figure 4.15 (b) or by the high displacement data in Figure 4.15 (a), there were distinct differences in the curves. At low displacements, the measured loads ordered with imposed rate, i.e. highest loads for the highest rate. In contrast, as shown in Figure 4.15 (a), the trend reverses at high displacement.

With regard to failure, in the hot-rolled and thermomechanically processed 1045 Al materials, higher strain rates caused failure to occur at lower displacements. However, the hot-rolled and thermomechanically processed 10V45 materials did not exhibit this behavior. No correlation can be drawn between strain rate and the extent of cracking as similar degrees of fracture were often observed for all three strain rates at a given strain. Similarly, no correlation between strain rate and processing conditions was found for the hot-rolled and thermomechanically processed 10V45 w/Nb materials. The nature of crack formation and type of crack (i.e. shear or longitudinal) were independent of strain rate over the strain rate range investigated. As the observed response of the 1045 and 10V45 w/Nb exhibited limited sensitivities to displacement rate, all subsequent tests were performed only at the highest displacement rate, 15 mm/s APPENDIX B contains a table for each 1045 material summarizing crack severity with respect to strain and strain rate for samples tested in the initial stage of testing. Macrographs of example samples illustrating what is considered uncracked, low, moderate and high severity shear and longitudinal cracks are also available in the appendix.

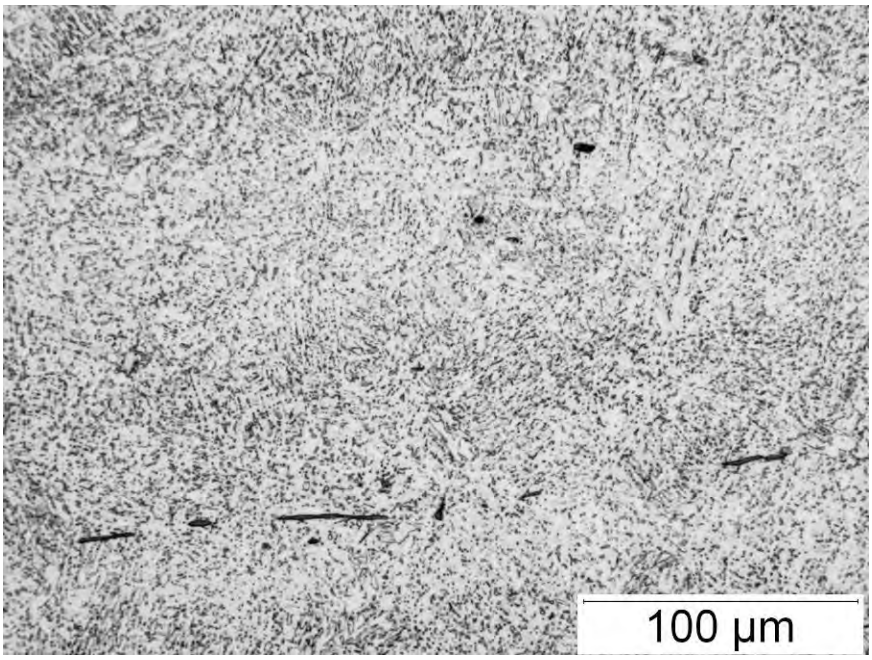

(a)

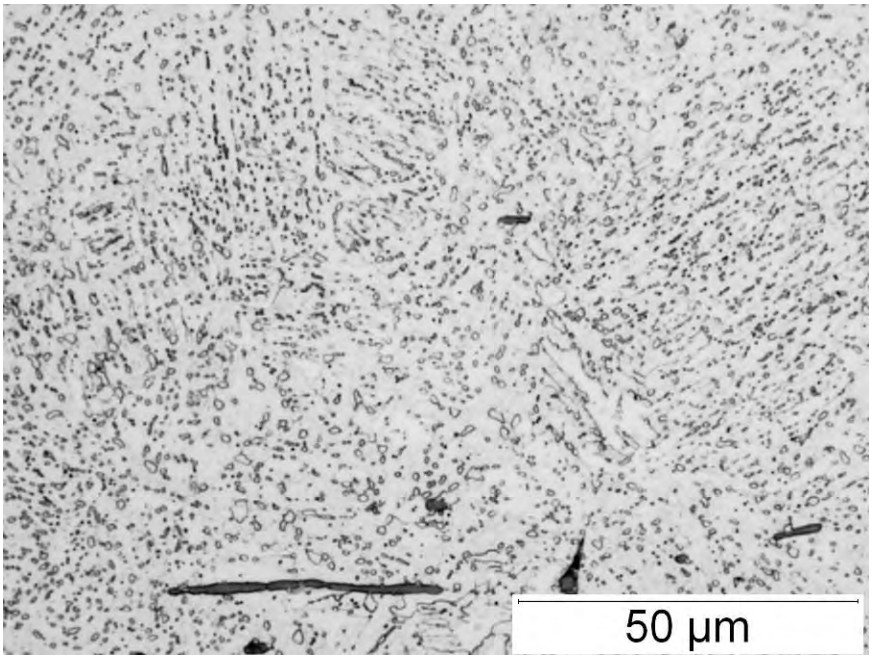

(b)

Figure 4.9 Light optical micrographs of a longitudinal section from a representative spheroidized 10V45 w/Nb sample. (Austenitized at 1000 °C for an hour, water quenched, heated to 700°C for 48 hours and air cooled.) HV=194. The direction of rolling is horizontal. (a) Low magnification (b) high magnification. Etchant is 2 pct nital.

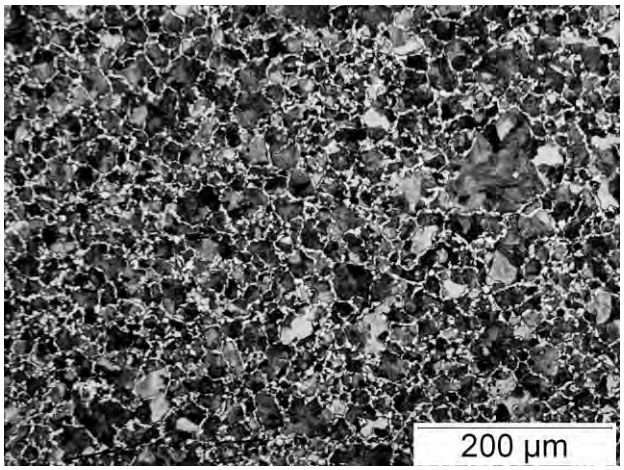

(a)

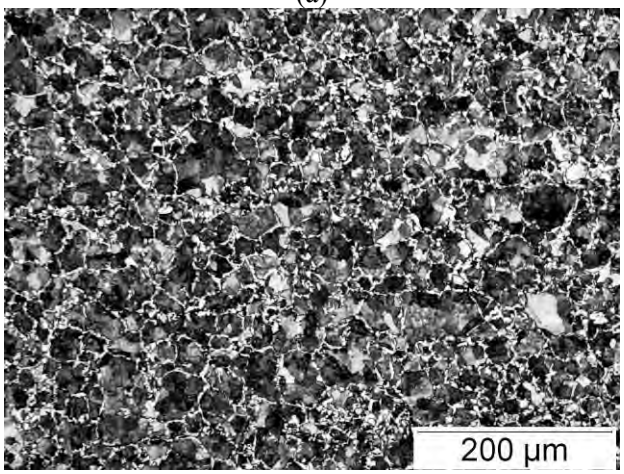

(b)

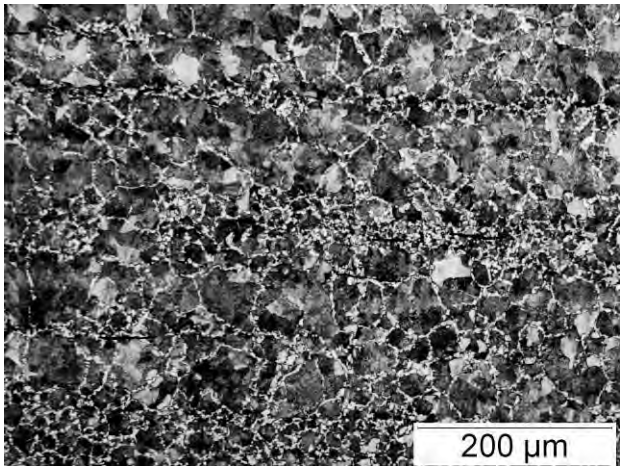

(c)

Figure 4.10 Light optical micrographs of longitudinal sections of heat-treated 10V45 w/Nb samples: (a) Normalized (heated to 1000 °C and air cooled) HV=292, (b) normalized (same treatment in (a)) and aged (heated to 625°C for an hour) HV=292, (c) normalized (same treatment in (a)) and over-aged (heated to 675 °C for an hour) HV=262. The direction of rolling is horizontal. Etchant is 2 pct nital.

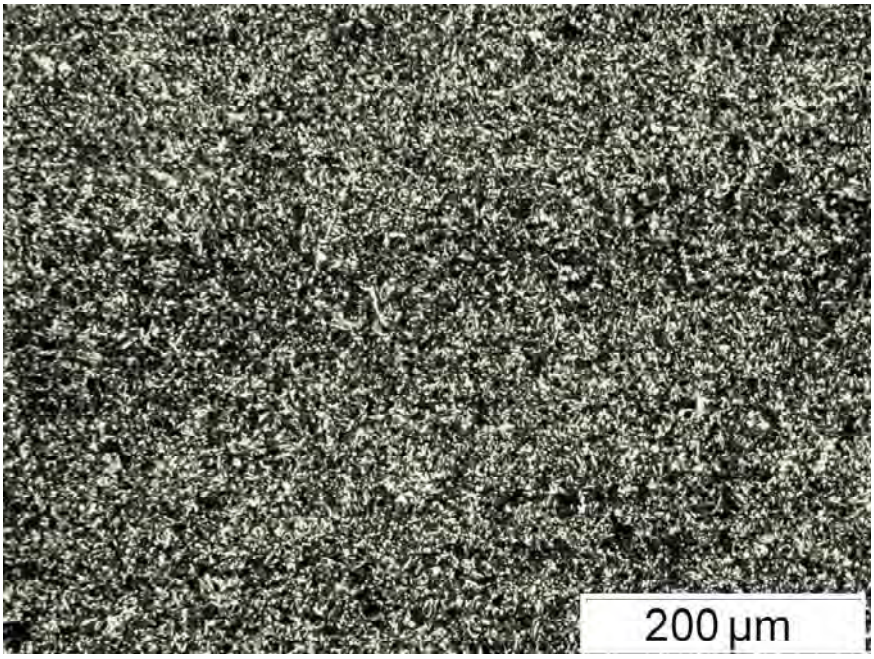

(a)

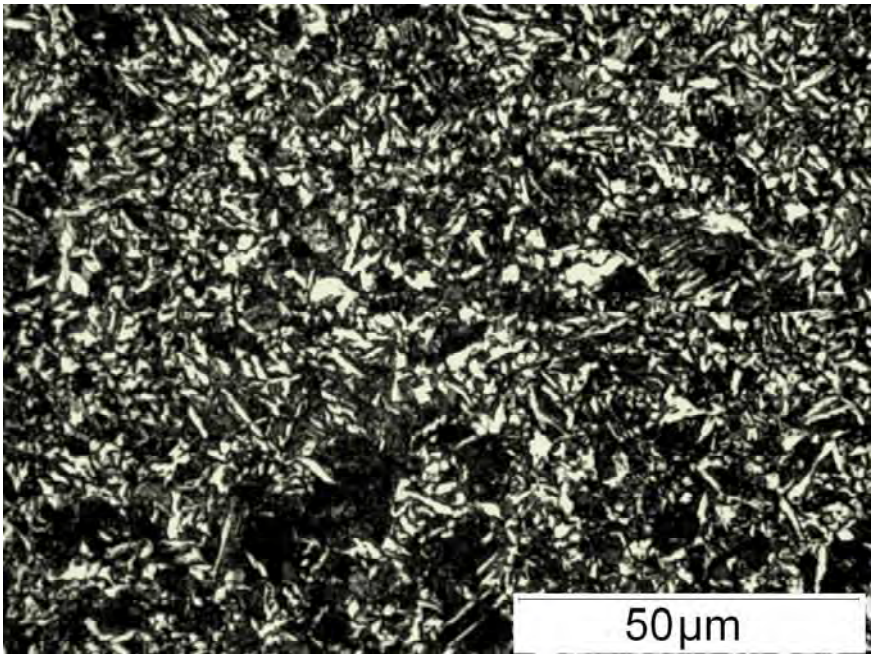

(b)

Figure 4.11 Light optical micrographs of longitudinal sections of heat-treated 10V45 w/Nb samples austenitized at 866 °C and isothermally transformed for 20 minutes at 435 °C. HV=303. (a) Low magnification (b) high magnification. The direction of rolling is horizontal. Etchant is 2 pct nital.

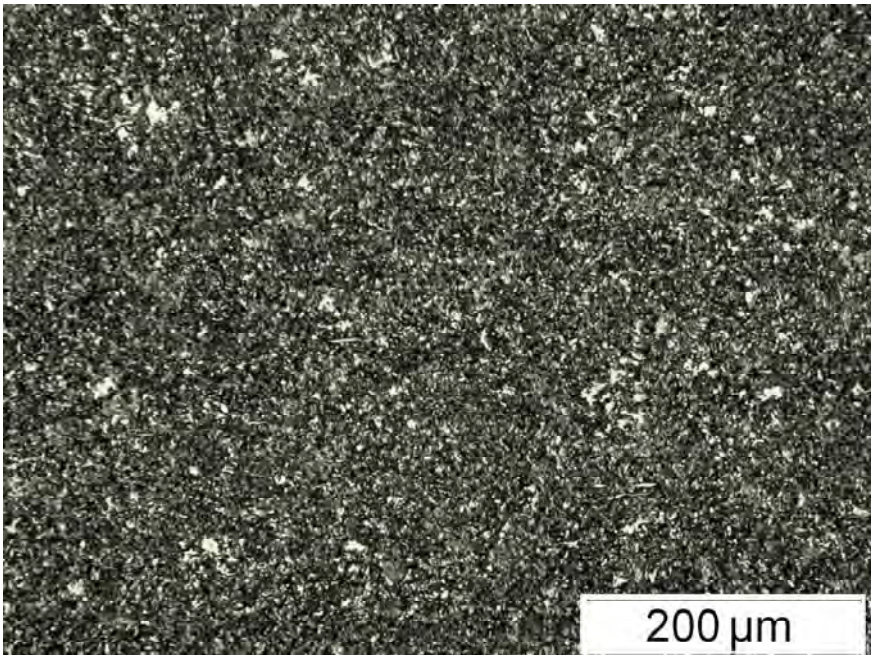

(a)

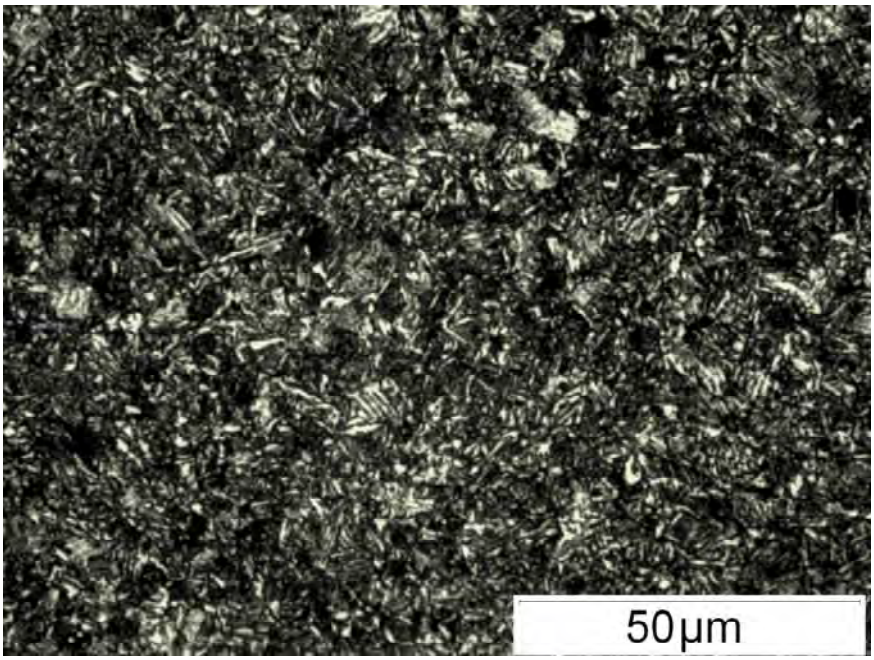

(b)

Figure 4.12 Light optical micrographs of longitudinal sections of heat-treated 10V45 w/Nb samples austenitized at 866 °C and isothermally transformed for 20 minutes at 365 °C. HV=322. (a) Low magnification (b) high magnification. The direction of rolling is horizontal. Etchant is 2 pct nital.

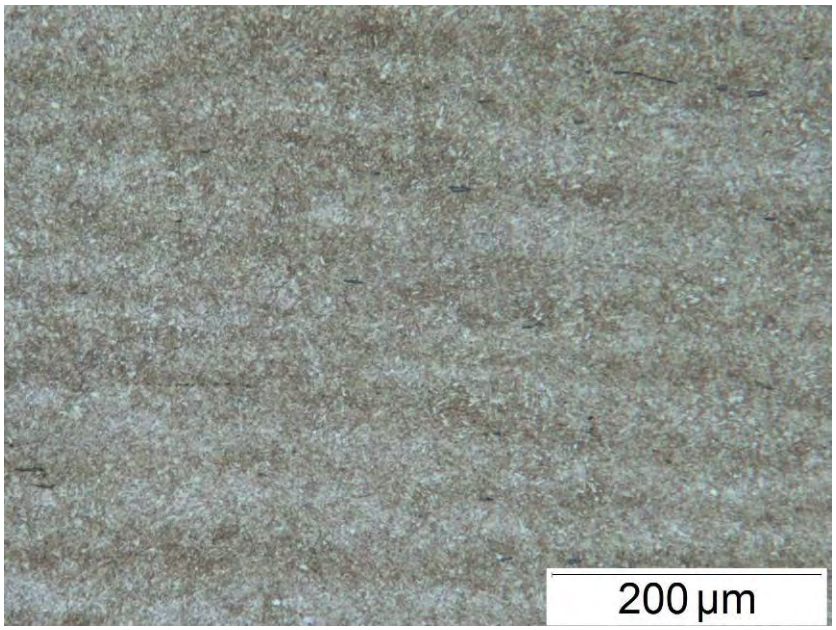

(a)

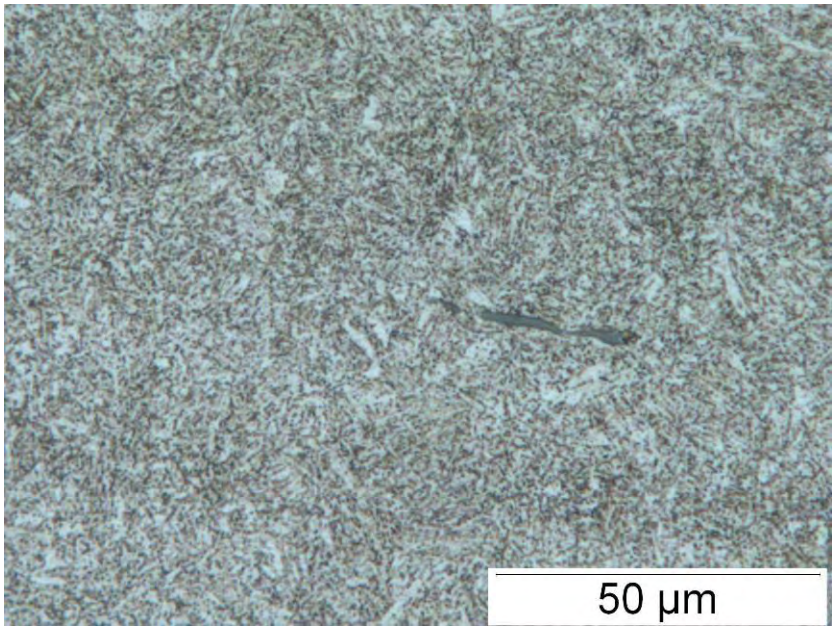

(b)

Figure 4.13 Light optical micrographs of longitudinal sections of the heat-treated 10V45 w/Nb samples austenitized at 870 °C, water quenched and tempered at 615 °C for two hours. HV= 304. (a) Low magnification (b) high magnification. The direction of rolling is horizontal. Etchant is 2 pct nital.

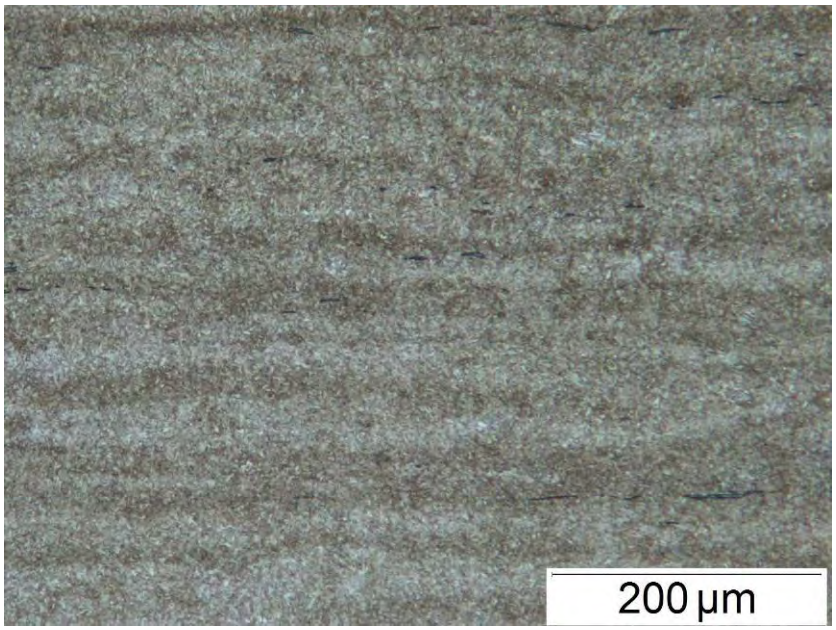

(a)

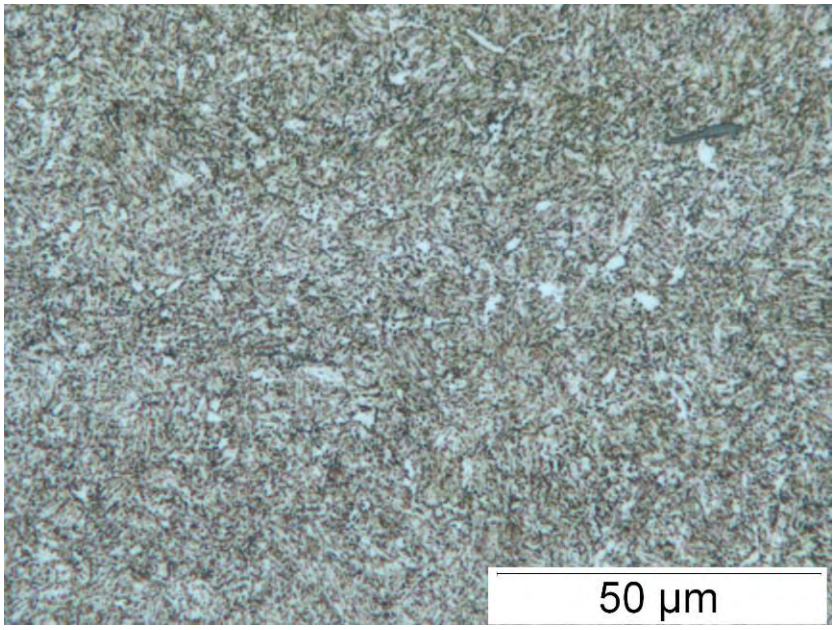

(b)

Figure 4.14 Light optical micrographs of longitudinal sections of the 10V45 w/Nb heat-treated condition austenitized at 870 °C, water quenched and tempered at 590 °C for two hours. HV=320. (a) Low magnification (d) high magnification. The direction of rolling is horizontal. Etchant is 2 pct nital.

4.3 Fracture Limits for As-received Materials

The fracture limits for all the as-received samples were determined by deforming samples of each alloy to preset strains and examining the sample surface in a stereo microscope at 20X. For each alloy set, individual strains varied by 2.5 pct engineering strain and the maximum level of strain at which no cracks are observed is referred to as the fracture limit for the material and is expressed in terms of true compressive strain. It should be noted that the criteria for determining fracture limits is different than that for evaluating effects of strain rate, for which examination of cracks is done at a lower magnification (7X) under a stereo microscope. The fracture limit data are summarized in Table 4.2. The hot-rolled 1045 Al and 10V45 were found to have the best formability out of the 1045 series materials (0.85 true strain for 1045 Al and 0.84 for 10V45). The thermomechanically processed 1045 Al and 10V45 have comparable

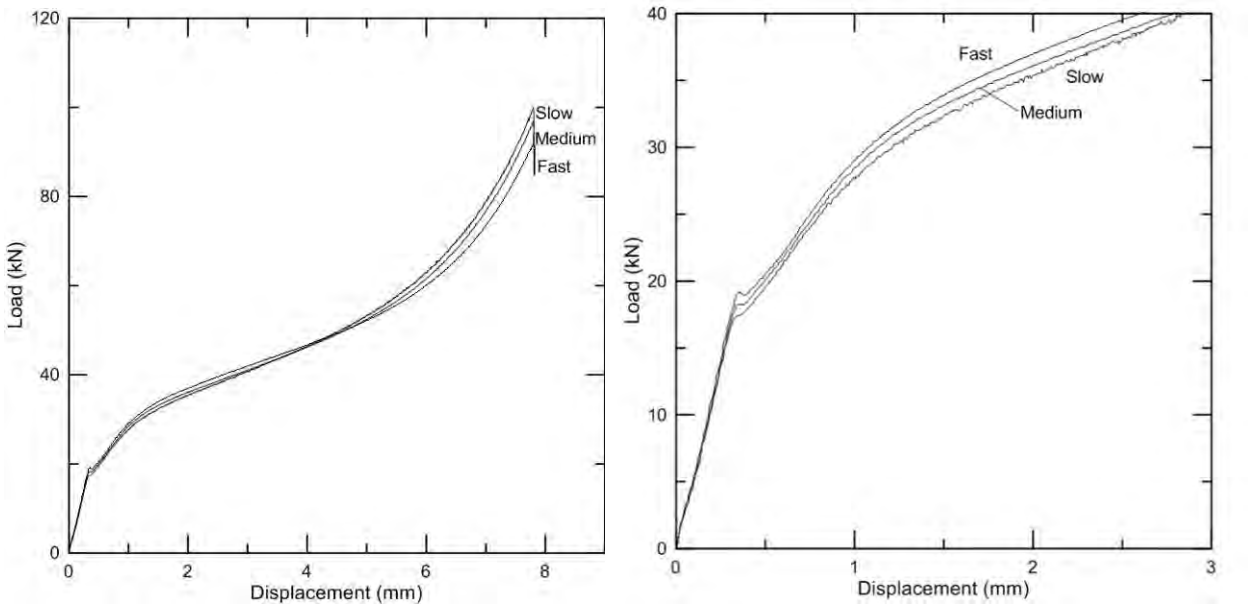

(a) (b)

Figure 4.15 (a) Load-displacement curves for three samples of 10V45 w/Nb tested with the indicated strain rates. (b) A magnified view of the low displacement behavior shown in (a). The curves are not corrected for machine stiffness.

yet lower fracture limits than their hot-rolled counterparts (0.69 and 0.64, respectively). The hot-rolled and thermomechanically processed 10V45 w/Nb materials have very similar fracture limits but a slightly higher one in case of the hot-rolled material (0.69 and 0.63, respectively). Cracks critical to defining fracture limits for all materials were all longitudinal cracks except for hot-rolled 4140 where cracks at strains slightly greater than the strain limit were shear cracks.

The 41XX materials exhibited higher fracture limits than those observed for the 1045 materials. The as-hot-rolled materials have a 1.24, 0.86 and 1.36 compressive true strain fracture limits for the 4135, 4140 and PL41 materials, respectively. For the pre-drawn materials, 4135 has the highest fracture limit

value (1.43 true strain) while the 4140 and PL41 steels have similar lower fracture limits (1.24 true strain for both materials). The spheroidized 41XX materials have the best formability out of all the materials tested. The test methodology devised could not incur cracks even when deformed to the hydraulic frame maximum load limit of 444.8 kN (100 kip).

Testing of the low C materials (HR and CR 16MnCr5) revealed that they have fracture limits higher than the 1045 materials but lower than most 41XX materials. The HR material has a slightly higher fracture limit (0.95 true strain) than the CR material (0.91 true strain) but both materials exhibit values much lower than the pre-drawn 41XX materials. In addition, the high C material (1080V) was found to have a slightly lower fracture limit (0.87 true strain) than the low C materials.

Table 4.2 – Summary of Fracture Limit, Yield Stress and Hardness Data for As-received Materials

Material	Fracture Limit (True Compressive Strain)	Yield Stress (MPa)	Hardness (Vickers)
1045 Al	0.85±0.14	495±7.6	218±5.1
1045 Al TMP	0.69±0.16	503±16.7	196±4.0
10V45	0.84±0.15	641±2.6	255±4.0
10V45 TMP	0.64±0.17	695±15.3	259±5.1
10V45 w/Nb	0.69±0.16	673±12.1	275±3.7
10V45 w/Nb TMP	0.63±0.17	667±9.07	247±6.7
Hot-rolled 4135	1.24±0.10	642±5.2	299±12.1
Pre-drawn 4135	1.43±0.07	559±5.0	277±1.7
Spheroidized 4135	No fracture at 1.98	409±5.7	157±5.3
Hot-rolled 4140	0.86±0.14	774±10.2	319±6.8
Pre-drawn 4140	1.24±0.10	646±9.0	290±1.8
Spheroidized 4140	No fracture at 1.94	477±9.1	160±3.9
Hot-rolled PL41	1.35±0.10	513±14.5	255±4.7
Pre-drawn PL41	1.24±0.13	657±8.1	315±3.9
Spheroidized PL41	No fracture at 2.02	352±20.2	158±1.9
HR 16MnCr5	0.95±0.13	480±7.6	220±8.6
CR 16MnCr5	0.91±14	394±10.0	189±2.6
1080V	0.87±14	893±12.5	361±3.2

4.4 Comparative Study of Fracture Evolution in As-received Materials

In addition to defining fracture limits, tests were also performed for almost all materials at three levels of strain regardless of the fracture limit. The purpose of doing this was to be able to compare different materials relative at the same level of strain and to have and understanding of the relative changes in crack response and surface features with increasing strain. In order to achieve this goal, macrographs were captured of samples cold headed using the 15 mm/s speed at three levels of strain. These strain levels are nominally referred to as low (ranging from 0.85 to 0.91 true compressive strain),

medium (ranging from 1.10 to 1.15 true compressive strain), and high (ranging from 1.38 to 1.52 true compressive strain). Each figure from Figure 4.16 to Figure 4.31 contains images for one as-received material and each sample is photographed at low and high magnifications. The fracture limit is referenced in the discussion of these images to better understand the nature and extent of fracture close to the fracture limit.

Figure 4.16 through Figure 4.19 are of as-received 1045 materials. Samples for 1045 Al TMP and 10V45 w/Nb TMP were unavailable as well as at certain levels of strains for the other 1045 materials as the available samples were used in deformation speed variations effects, establishing a procedure to assess fracture limits. Figure 4.16 contains medium and high strain 1045 Al samples. Even though the fracture limit is 0.89 true compressive strain for the material, no cracks can be seen in the medium strain sample (1.15 true compressive strain). Macrographs of the 10V45 material are shown in Figure 4.17. Even though the fracture limit was 0.85 true compressive strain, the medium strain sample (1.15 true compressive strain) in Figure 4.16 (a) and (b) exhibited no observable cracks at these magnifications. In the high strain level sample in Figure 4.16 (c) and (d), multiple 'mixed mode' (i.e. shear and longitudinal) cracks were easily visible on the free surface. The cracks propagated at a 45° angle but shifted direction with displacement and propagated longitudinally. The surface of both samples exhibited the 'orange peel' phenomenon where the roughening of the examined surface occurs.

Figure 4.17 shows samples of the three strain levels for the 10V45 material (fracture limit 0.69 true compressive strain). No visible cracks are present in the low strain level in the image at these magnifications (Figure 4.17 (a) and (b)). At the medium level strain, small longitudinal cracks were easily observed and are highlighted by arrows in Figure 4.17 (d). At the high strain level (Figure 4.17 (e) and (f)), large cracks that are of a mixed longitudinal and shear character are observed. The surface of 10V45 materials underwent some degree of surface roughening (i.e. formation of orange peel) but not to the extent of the 1045 Al material. Figure 4.18 and Figure 4.19 show sample from the 10V45 TMP and the 10V45 w/Nb materials at the low strain level, respectively. A small incipient crack highlighted by an arrow can be seen in Figure 4.18 (b) for the 10V45 TMP material. The surface exhibited some surface roughening. No cracks were observed in the 10V45 w/Nb sample at these magnifications (Figure 4.18 (a) and (b)). However, the sample exhibited a greater extent of surface roughening than the 10V45 w/Nb.

Figure 4.20 through Figure 4.28 are of all the 41XX materials at the three strain levels. In addition to the surface features previously described for 1045 materials, some 41XX exhibited longitudinal surface relief bands on the examined surfaces. An example is seen in Figure 4.20 (f) of the hot-rolled 4135 material. Hot-rolled and pre-drawn 4135 and 4140 materials in addition to the spheroidized 4140 exhibited surfaces with parallel longitudinally elongated surface relief features unlike the equiaxed orange peel surface roughening in 1045 materials. These features are observed as multiple

longitudinal bands distributed around the sample circumference. The number of these bands increases with increasing strain. Incipient cracks critical to defining fracture limits mostly occur longitudinally along these longitudinal surface bands for materials with such features. The remaining 41XX materials have surfaces that do not have these longitudinal surface features but exhibit surface roughening to various extents.

Figure 4.20 shows samples of the hot-rolled 4135 material (1.24 true strain fracture limit). No cracks were present at the low (0.87 true strain) and medium (1.13 true strain) strain levels. However, incipient cracks that are not visible in images of these magnifications (Figure 4.20 (e) and (f)) were observed in the high strain level sample along the longitudinal surface relief bands. For pre-drawn 4135 material in Figure 4.21, the material was formed to the three levels of strain without the occurrence of any cracks as the high strain level (Figure 4.21 (e) and (f)) represented the fracture limit for this material (i.e. the lowest strain at which cracks were not detected). The density of surface bands was less for pre-drawn 4135 than the hot-rolled 4135 materials. For spheroidized 4135 shown in Figure 4.22, surface roughening (i.e. orange peel) without the presence of longitudinal bands was observed. The extent of surface roughening is independent of strain. No cracks are present at the three levels of strain as a fracture limit could not be defined for the material.

The hot-rolled 4140 materials in Figure 4.23 exhibited an unusual propensity for developing shear cracks. These cracks propagated at a 45° angle to the longitudinal surface bands. No cracks were present in the low strain level (Figure 4.23 (a) and (b)) as it represented the fracture limit for the material. A single crack at 45° to the axis of loading was present in the medium strain level in Figure 4.23 (c) and (d). At the high strain level (Figure 4.23 (e) and (f)), multiple shear and longitudinal cracks parallel to the longitudinal surface bands were present. The shear crack at the left of the image was similar to that at the medium strain level. The longitudinal crack evident in both images was parallel to the longitudinal surface features with a component of shear fracture toward the bottom of the image. The density and depth of longitudinal surface features was higher for the hot-rolled 4140 material as compared with the pre-drawn material in Figure 4.24. The pre-drawn 4140 material in Figure 4.24 did not exhibit a tendency towards shear fracture and the density of longitudinal surface features was much less than for the hot-rolled material. Small not-easily detectable crack openings along longitudinal surface features are present at the high strain level Figure 4.24 (e) and (f). For the spheroidized 4140 material shown in Figure 4.25, the low level of strain is not shown but a higher level of strain (1.73 true compressive strain) is added. No cracks are observed at all levels of strain as a fracture limit could not be defined for this material. Longitudinal surface bands of less numbers and depths than the pre-drawn material for a given strain were observed but no cracks were observed along any of these bands.

The hot-rolled and pre-drawn PL41 materials are shown in Figure 4.26 and Figure 4.27 and have no cracks at the low and medium strain levels. However, small longitudinal cracks that are not easily detectable cracks are observed at the high level strains for both materials. These cracks are highlighted by arrows in Figure 4.26 (f) and Figure 4.27 (f) for the hot-rolled and pre-drawn PL41 materials, respectively. The spheroidized PL41 material in Figure 4.28 shows no cracks at all strain levels as a fracture limit could not be defined for this material. No longitudinal surface features are observed in the PL41 materials. Instead, equiaxed orange peel or surface roughening is apparent on the surfaces of the samples. Contrasting the 41XX materials with 1045 materials at the three levels of strain shows that 41XX have superior formabilities with the exception of hot-rolled 4140 material.

Figure 4.29 and Figure 4.30 are of the low carbon materials (HR and CR 16MnCr5, respectively). Both materials exhibited longitudinal surface features (bands) which become more pronounced at higher strains. Both materials had similar formabilities as no cracks were observed at the low and medium strain levels but small cracks that were not readily apparent from the images were detected at the magnifications shown in the high strain levels for both materials. These incipient cracks occurred along the longitudinal surface features similar to 41XX materials that exhibited longitudinal surface bands. Figure 4.31 shows samples of the high carbon material (1080V). The low strain level (Figure 4.31 (a) and (b)) represented the fracture limit for the material so no cracks were detected at that level of strain. No cracks are visible in the medium level strain (Figure 4.31 (c) and (d)) at this magnification. However, small longitudinal cracks were detected under a stereo microscope at 20X when determining fracture limits. A large longitudinal crack and a small longitudinal crack are highlighted by arrows in the high strain level sample in Figure 4.31 (e) and (f). Equiaxed surface roughening (i.e. orange peel) takes place in all samples.

4.5 Cold Heading Response for 10V45 w/Nb Heat-treated Materials

Testing of heat-treated materials was unable to define definite fracture limits with high certainty. Incipient cracks were detected at lower strains than the fracture limit of the as-received 10V45 w/Nb material by examining the sample under a stereo microscope at 20X. Decreasing the amount of strain did not completely inhibit the presence of incipient cracks that are detectable by the procedure prescribed for defining fracture limits. These incipient cracks, however, did not turn into large cracks easily visible with the naked eye unless significantly higher strains are imposed. For this reason, samples were photographed at three levels of strains for each material to evaluate and contrast the cold heading behavior of heat-treated 10V45 w/Nb samples.

Figure 4.32 through Figure 4.39 are of 10V45 w/Nb heat-treated samples. All the samples in these figures exhibited longitudinal cracking by the procedure for defining fracture limits. In some of the low strain level samples, cracks were readily visible in the images at the magnification used to take

pictures. Figure 4.32 shows spheroidized 10V45 w/Nb samples which were heat treated to a Vickers hardness of 194. Samples are shown at three strain levels in the figure. At a true compressive strain of 0.89 Figure 4.32 (a) and (b), no cracks are easily visible in the micrographs at these magnifications. However, small longitudinal cracks were detected under a stereo microscope at 20X magnification. The 1.15 true compressive strain for spheroidized 10V45 w/Nb material (the medium strain level) in Figure 4.32 (c) and (d) shows easily visible longitudinal cracks one of which is highlighted by an arrow in the high magnification image in Figure 4.32 (d). This crack was very thin but propagated longitudinally approximately 0.5 mm without measurable opening. In the high level of strain sample in Figure 4.32 (e) and (f), many cracks similar to those observed in Figure 4.32 (d) were distributed around the surface. Selected cracks are highlighted by arrows in Figure 4.32 (f). The surfaces of spheroidized samples were relatively smooth as it exhibited minimal surface roughening.

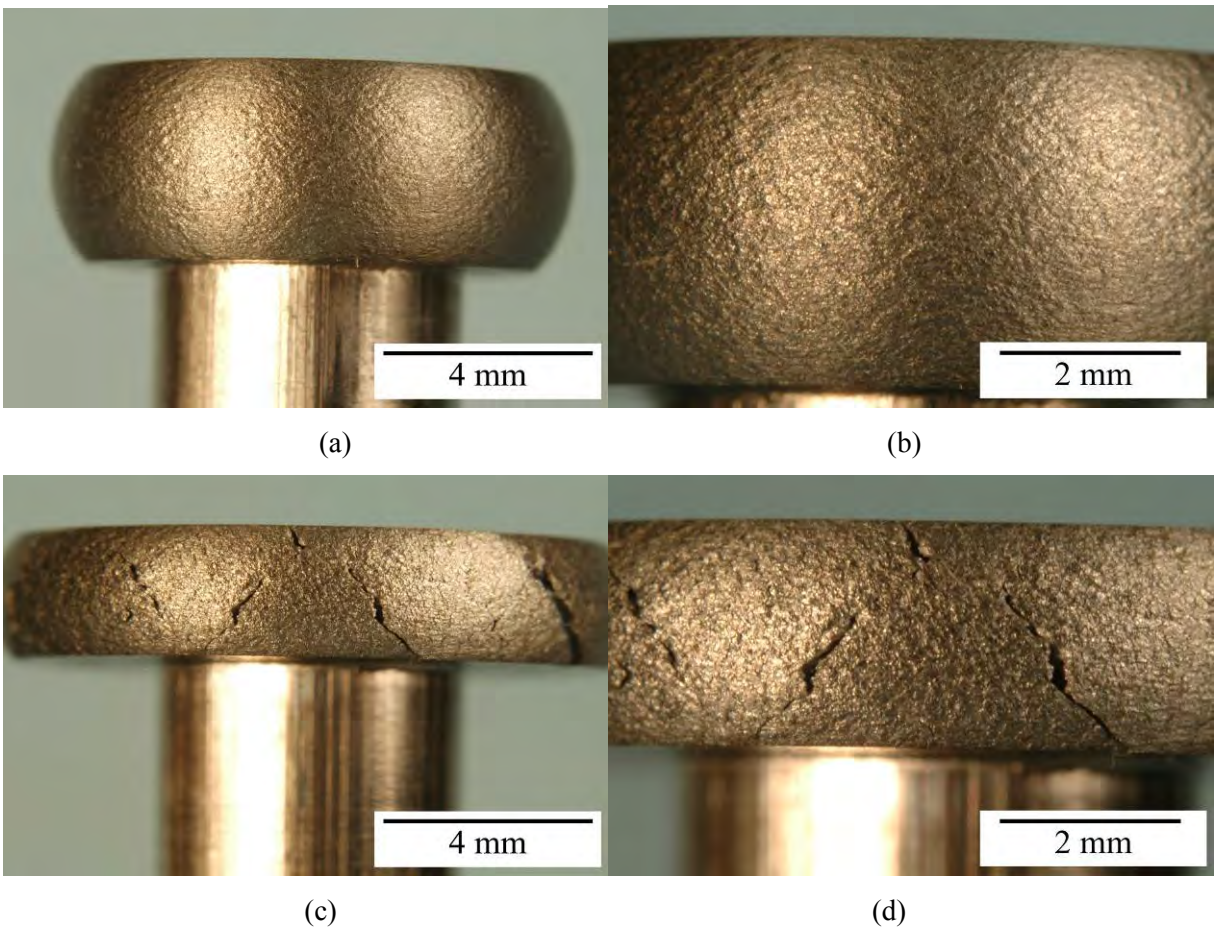

Figure 4.16 Macrographs of 1045 Al cold-headed samples at two levels of strain and two magnifications. Fracture limit is 0.85 true compressive strain. (a) and (b) 1.15 true compressive strain (c) and (d) 1.52 true compressive strain.

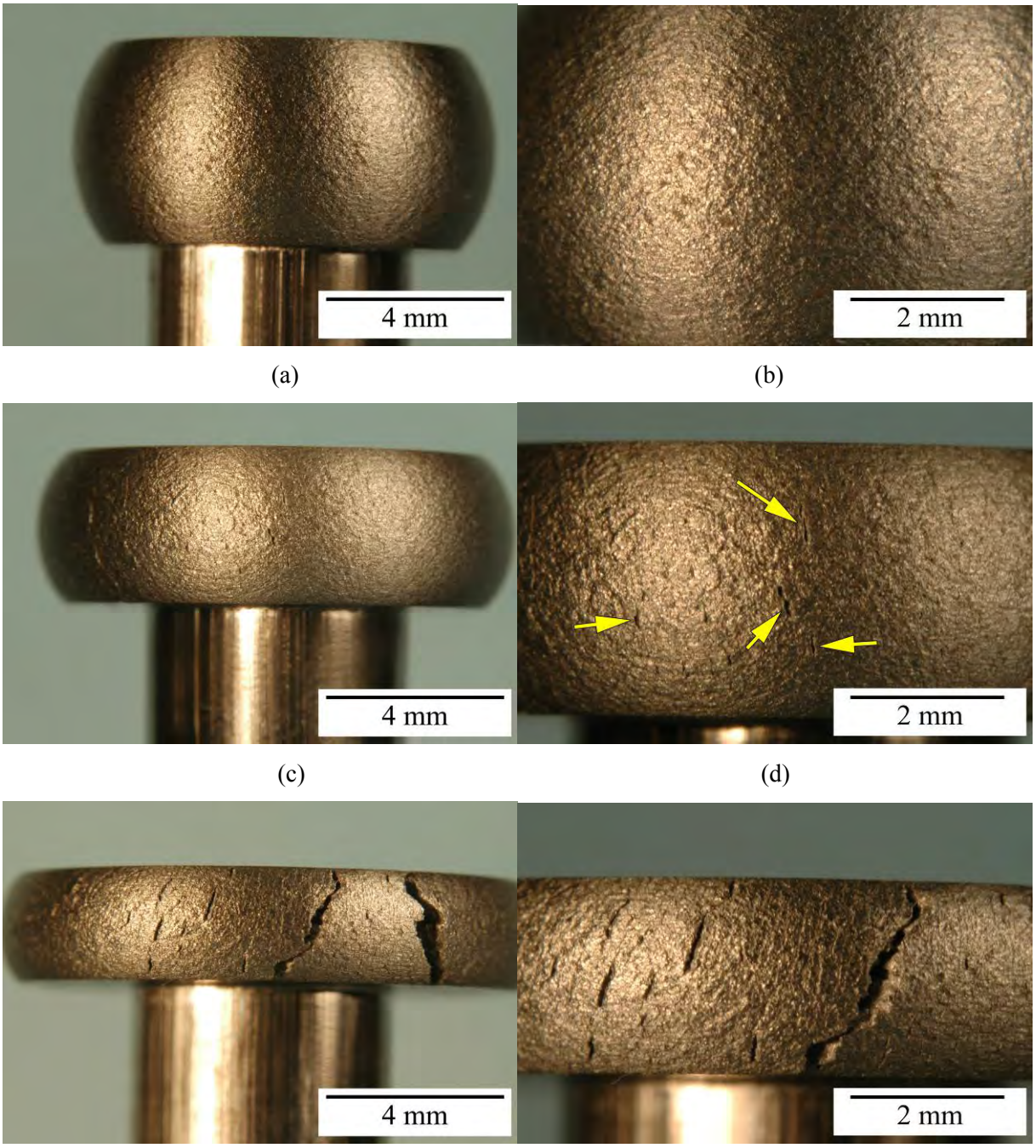

Figure 4.17 Macrographs of 10V45 cold-headed samples at three levels of strain and two magnifications. Fracture limit is 0.69 true compressive strain. (a) and (b) 0.89 true compressive strain (c) and (d) 1.15 true compressive strain (e) and (f) 1.52 true compressive strain.

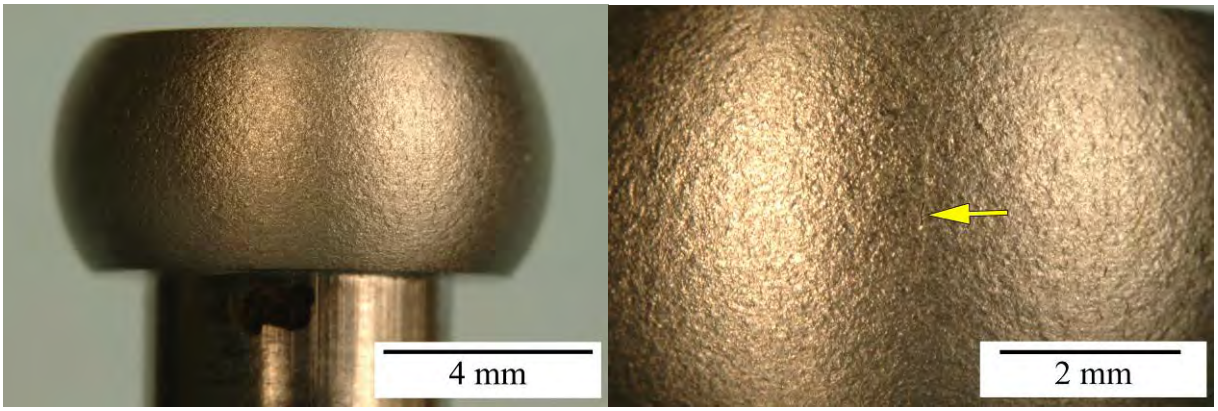

(a) (b)

Figure 4.18 Macrographs of 10V45 TMP cold-headed samples at one level of strain and two magnifications. Fracture limit is 0.64 true compressive strain. (a) and (b) 0.89 true compressive strain.

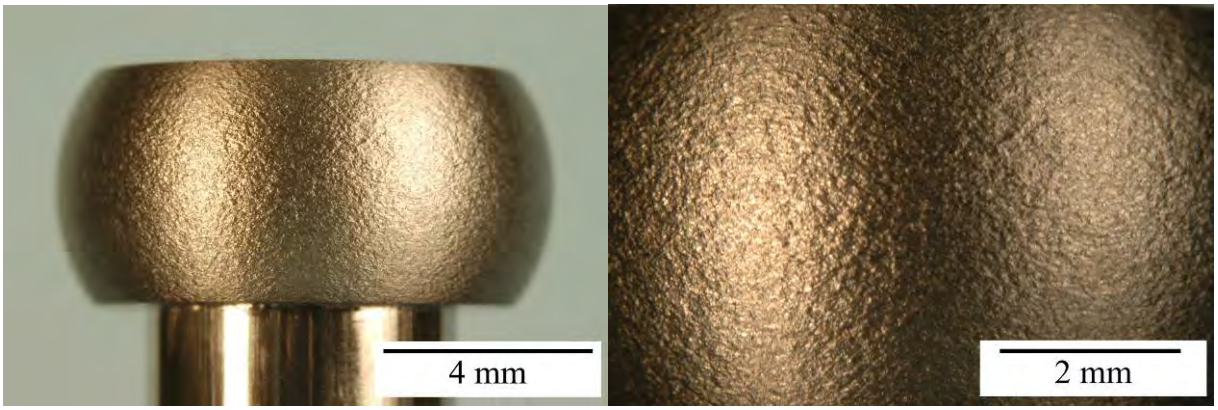

(a) (b)

Figure 4.19 Macrographs of 10V45 w/Nb cold-headed samples at one level of strain and two magnifications. Fracture limit is 0.69 true compressive strain. (a) and (b) 0.89 true compressive strain.

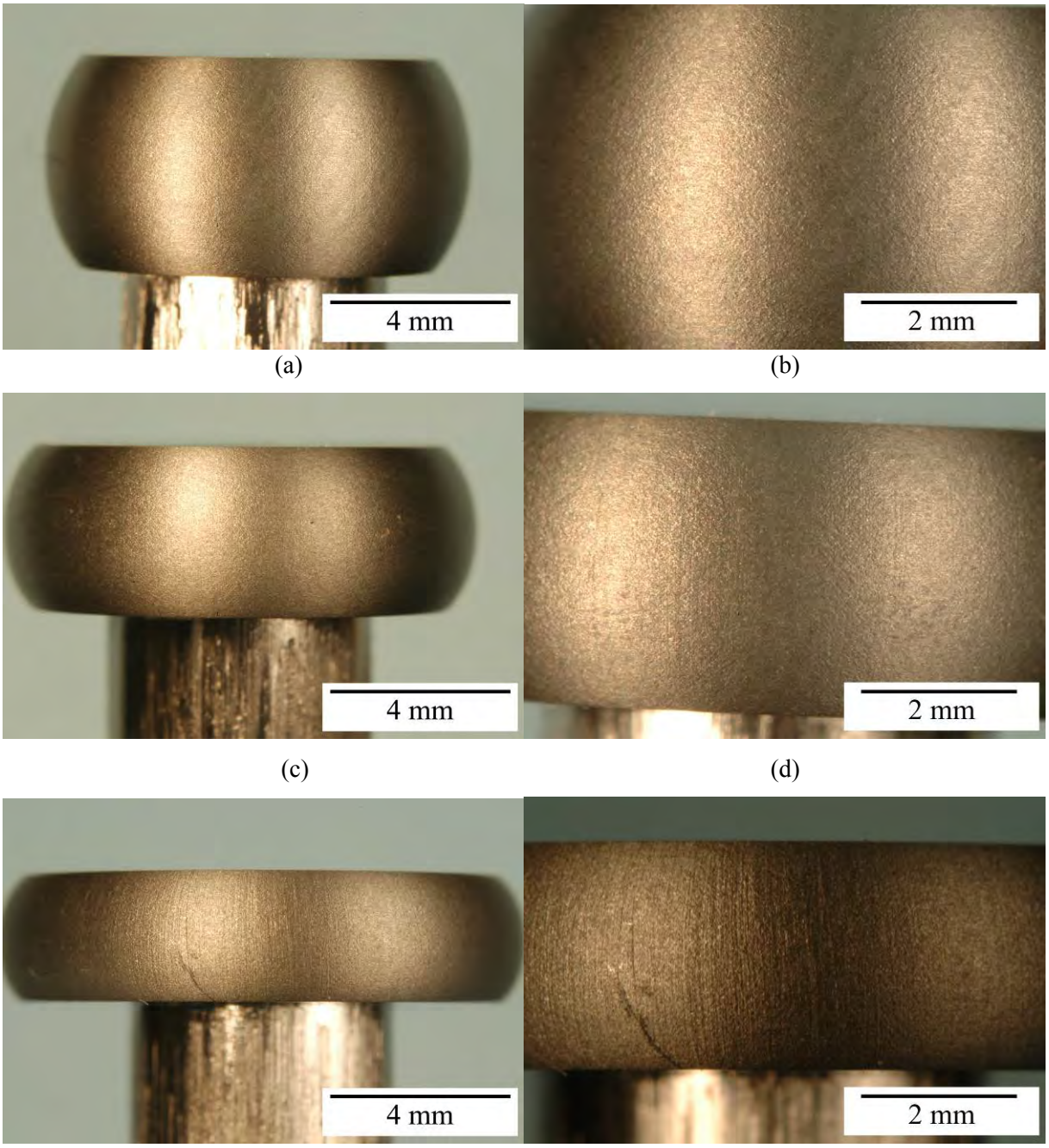

Figure 4.20 Macrographs of hot-rolled 4135 cold-headed samples at three levels of strain and two magnifications. Fracture limit is 1.24 true compressive strain. (a) and (b) 0.87 true compressive strain (c) and (d) 1.13 true compressive strain (e) and (f) 1.38 true compressive strain.

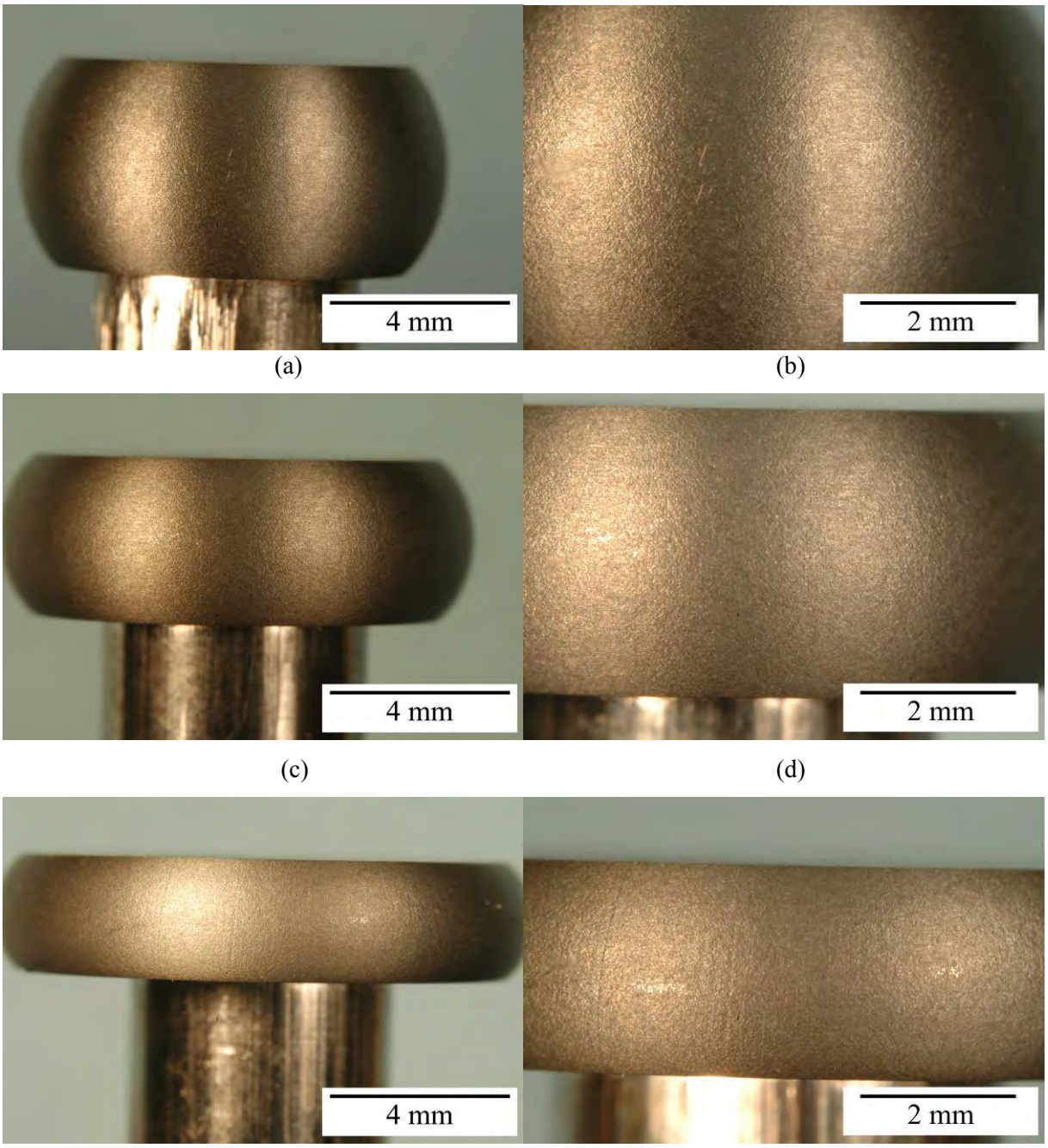

Figure 4.21 Macrographs of pre-drawn 4135 cold-headed samples at three levels of strain and two magnifications. Fracture limit is 1.43 true compressive strain. (a) and (b) 0.89 true compressive strain (c) and (d) 1.15 true compressive strain (e) and (f) 1.43 true compressive strain.

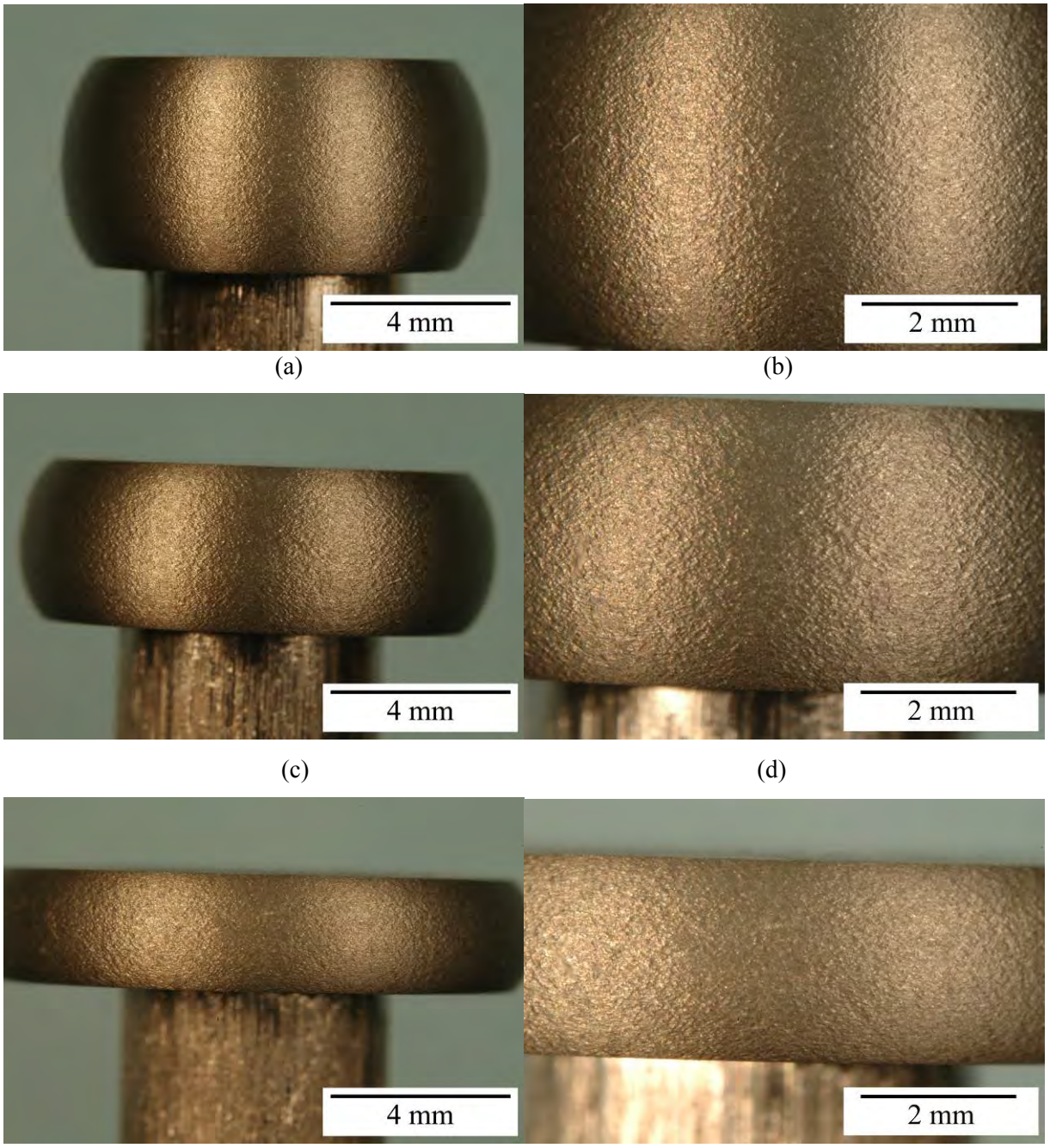

Figure 4.22 Macrographs of spheroidized 4135 cold-headed samples at three levels of strain and two magnifications. No cracks were detected at 20X magnification on a stereo microscope at a true compressive strain as high as 1.98 true compressive strain. (a) and (b) 0.89 true compressive strain (c) and (d) 1.15 true compressive strain (e) and (f) 1.52 true compressive strain.

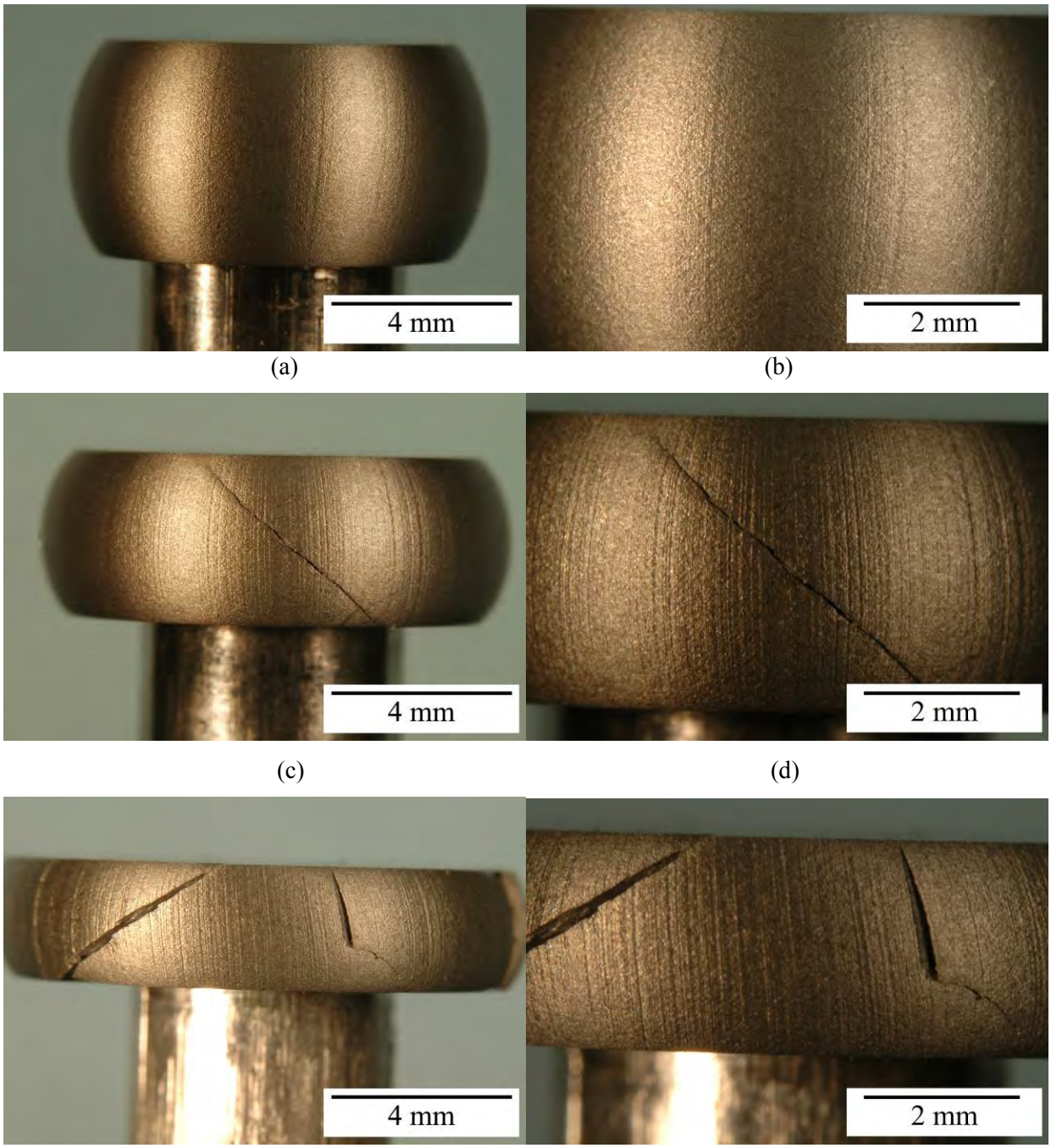

Figure 4.23 Macrographs of hot-rolled 4140 cold-headed samples at three levels of strain and two magnifications. Fracture limit is 0.86 true compressive strain. (a) and (b) 0.86 true compressive strain (c) and (d) 1.15 true compressive strain (e) and (f) 1.52 true compressive strain.

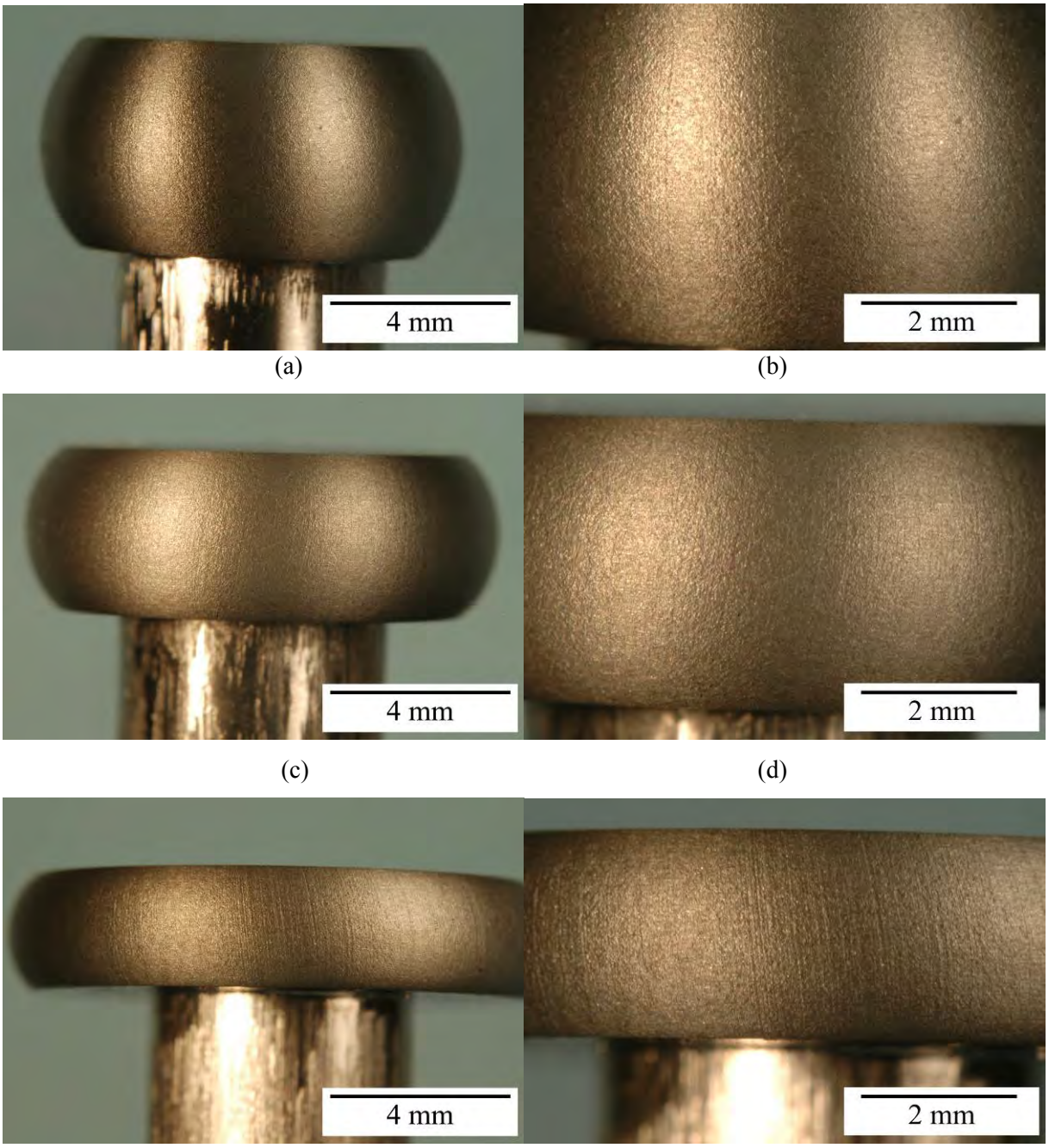

Figure 4.24 Macrographs of pre-drawn 4140 cold-headed samples at three levels of strain and two magnifications. Fracture limit is 1.24 true compressive strain. (a) and (b) 0.87 true compressive strain (c) and (d) 1.11 true compressive strain (e) and (f) 1.52 true compressive strain.

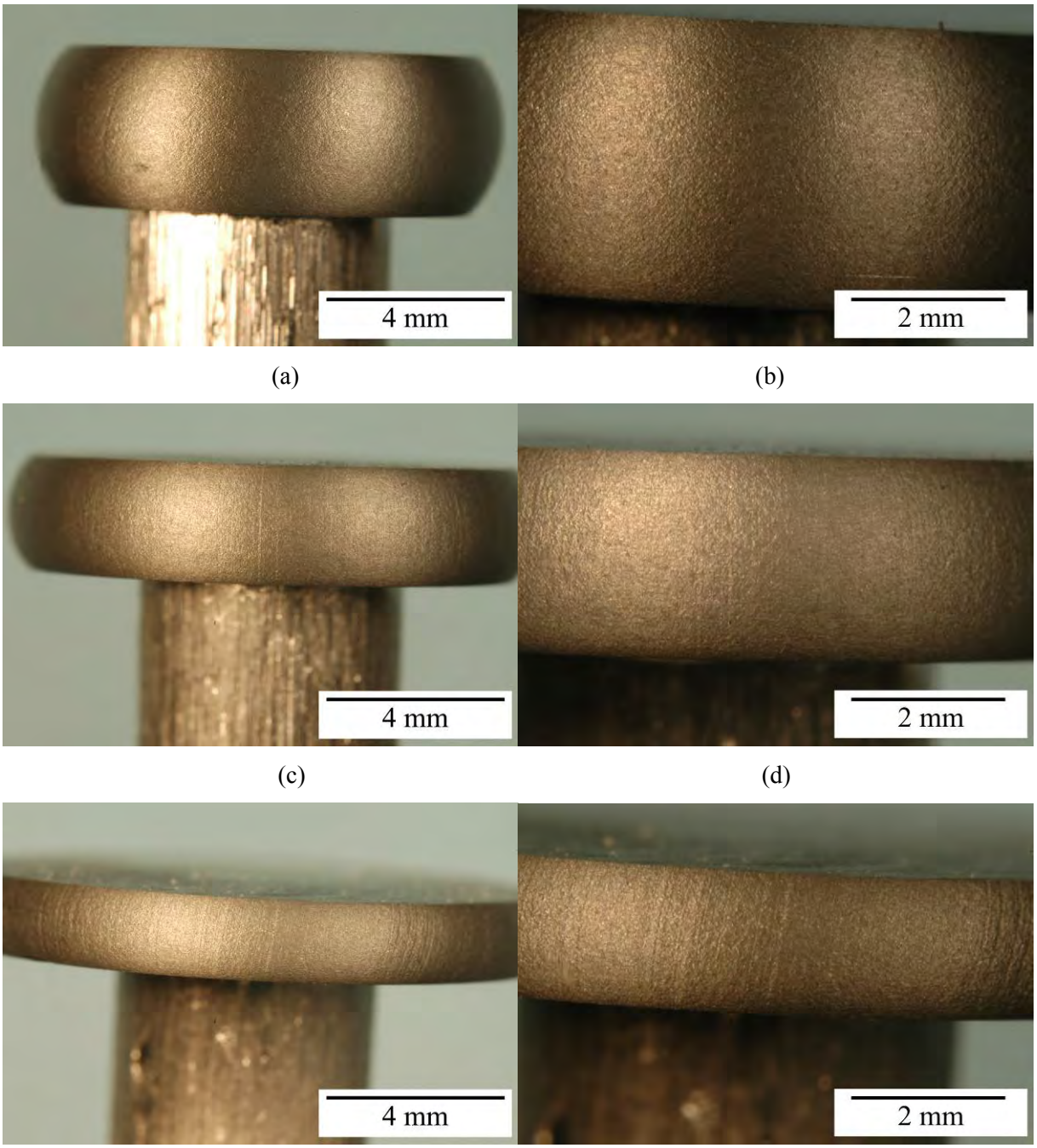

Figure 4.25 Macrographs of spheroidized 4140 cold-headed samples at three levels of strain and two magnifications. No cracks were detected at 20X magnification on a stereo microscope at a true compressive strain as high as 1.94 true compressive strain. (a) and (b) 1.15 true compressive strain (c) and (d) 1.52 true compressive strain (e) and (f) 1.73 true compressive strain.

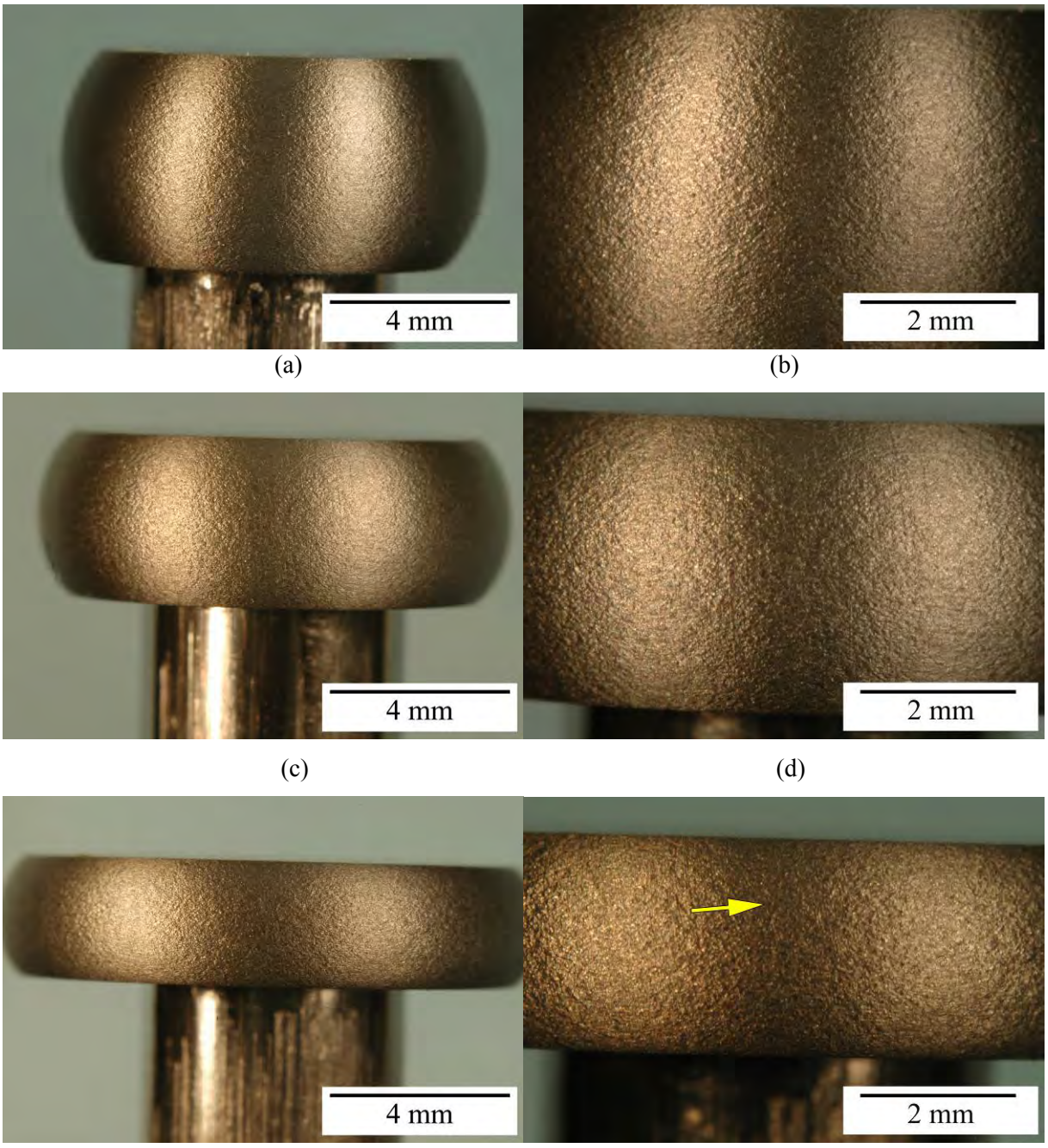

Figure 4.26 Macrographs of hot-rolled PL41 cold-headed samples at three levels of strain and two magnifications. Fracture limit is 1.35 true compressive strain. (a) and (b) 0.89 true compressive strain (c) and (d) 1.13 true compressive strain (e) and (f) 1.43 true compressive strain.

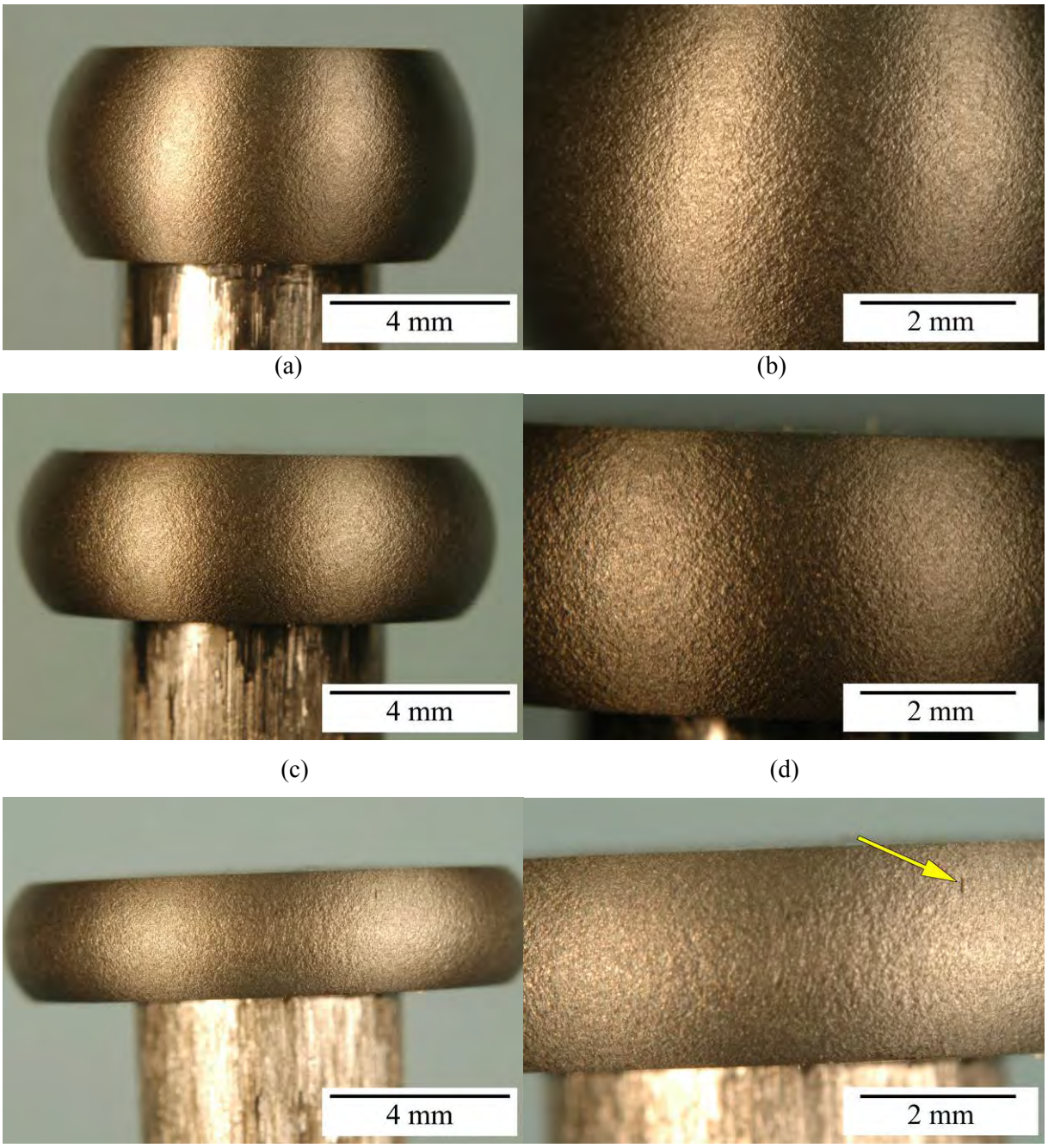

Figure 4.27 Macrographs of pre-drawn PL41 cold-headed samples at three levels of strain and two magnifications. Fracture limit is 1.24 true compressive strain. (a) and (b) 0.89 true compressive strain (c) and (d) 1.14 true compressive strain (e) and (f) 1.52 true compressive strain.

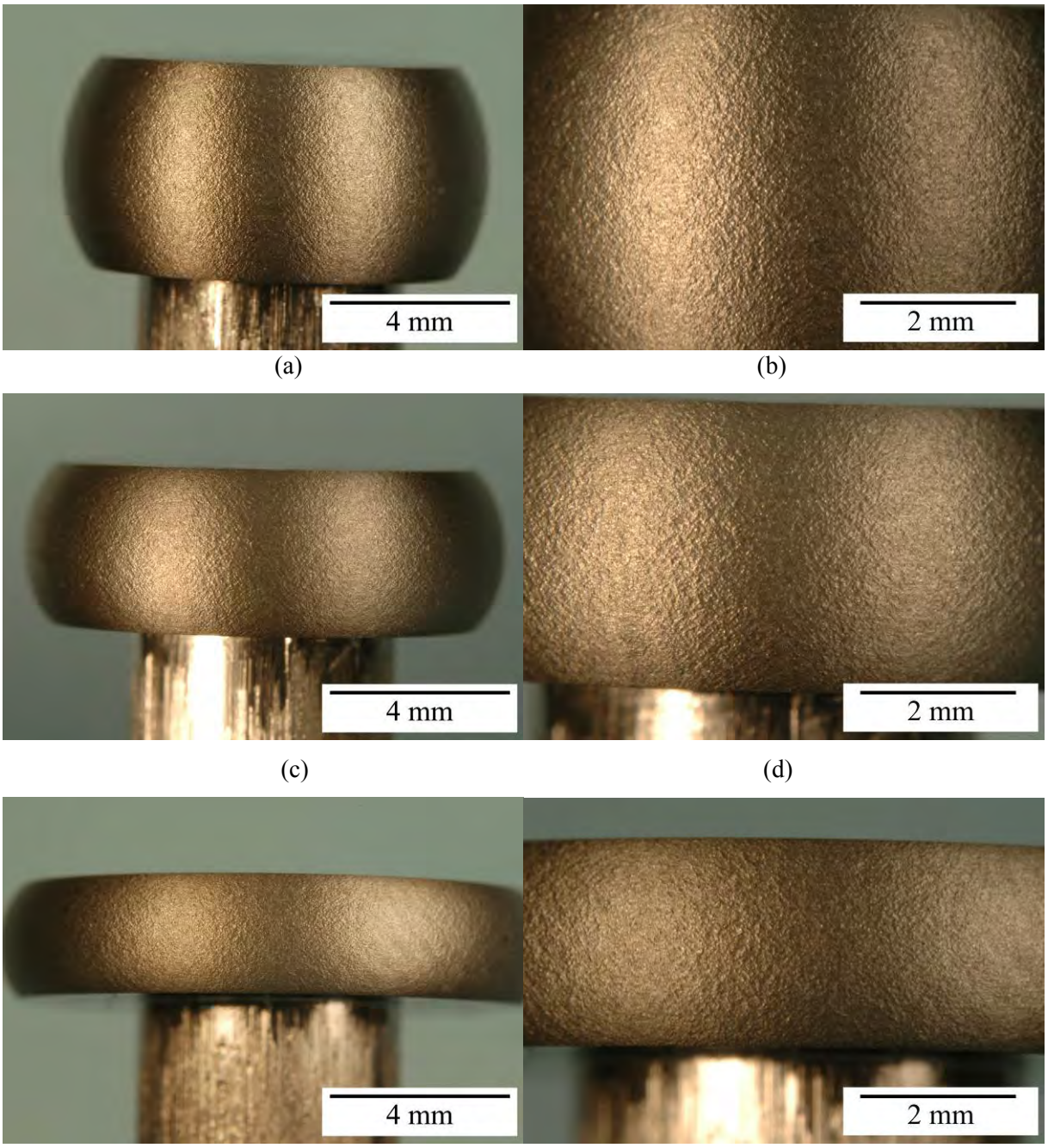

Figure 4.28 Macrographs of spheroidized PL41 cold-headed samples at three levels of strain and two magnifications. No cracks were detected at 20X magnification on a stereo microscope at a true compressive strain as high as 2.02 true compressive strain. (a) and (b) 0.89 true compressive strain (c) and (d) 1.15 true compressive strain (e) and (f) 1.52 true compressive strain.

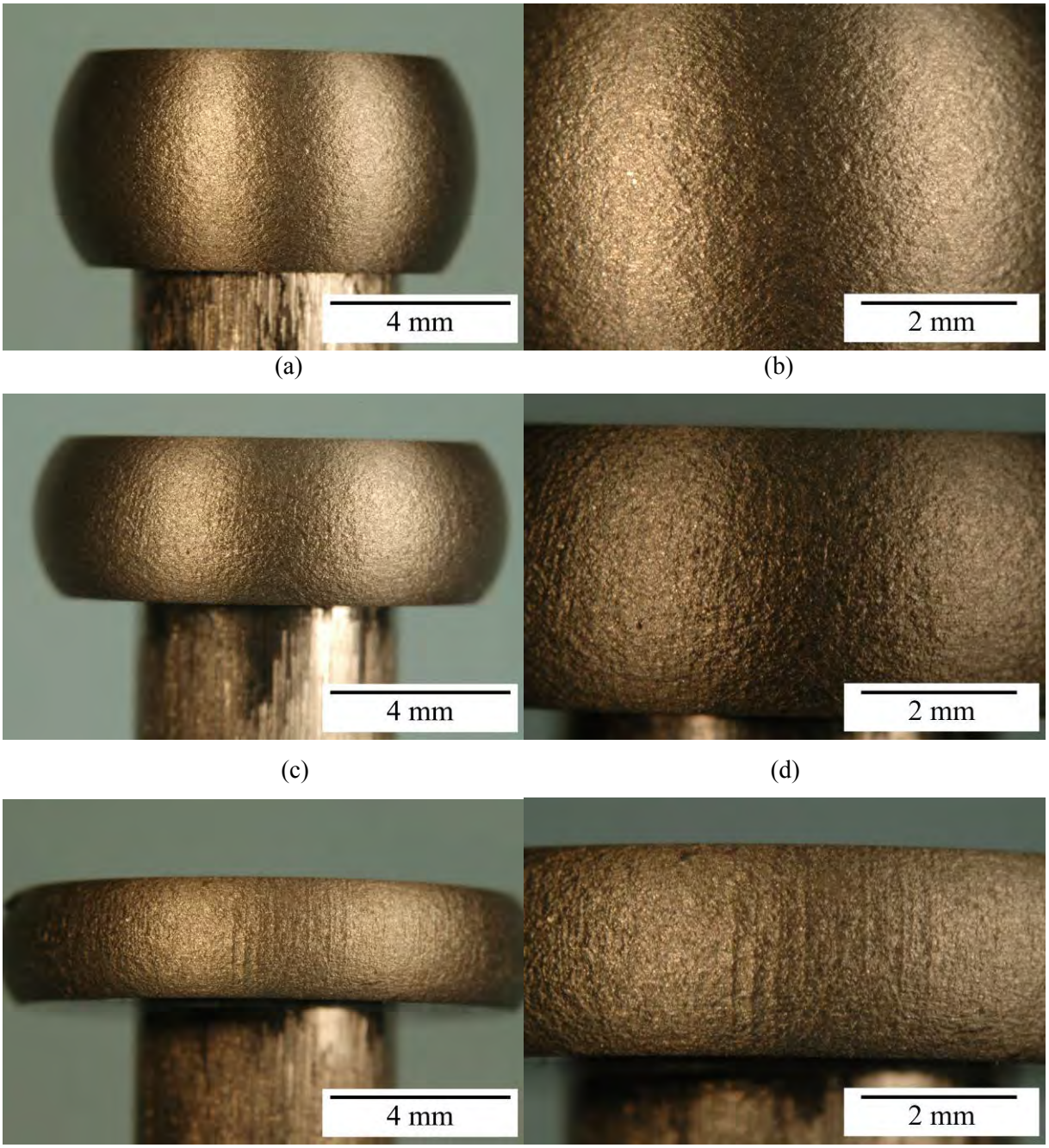

Figure 4.29 Macrographs of HR 16MnCr5 cold-headed samples at three levels of strain and two magnifications. Fracture limit is 0.95 true compressive strain. (a) and (b) 0.89 true compressive strain (c) and (d) 1.15 true compressive strain (e) and (f) 1.52 true compressive strain.

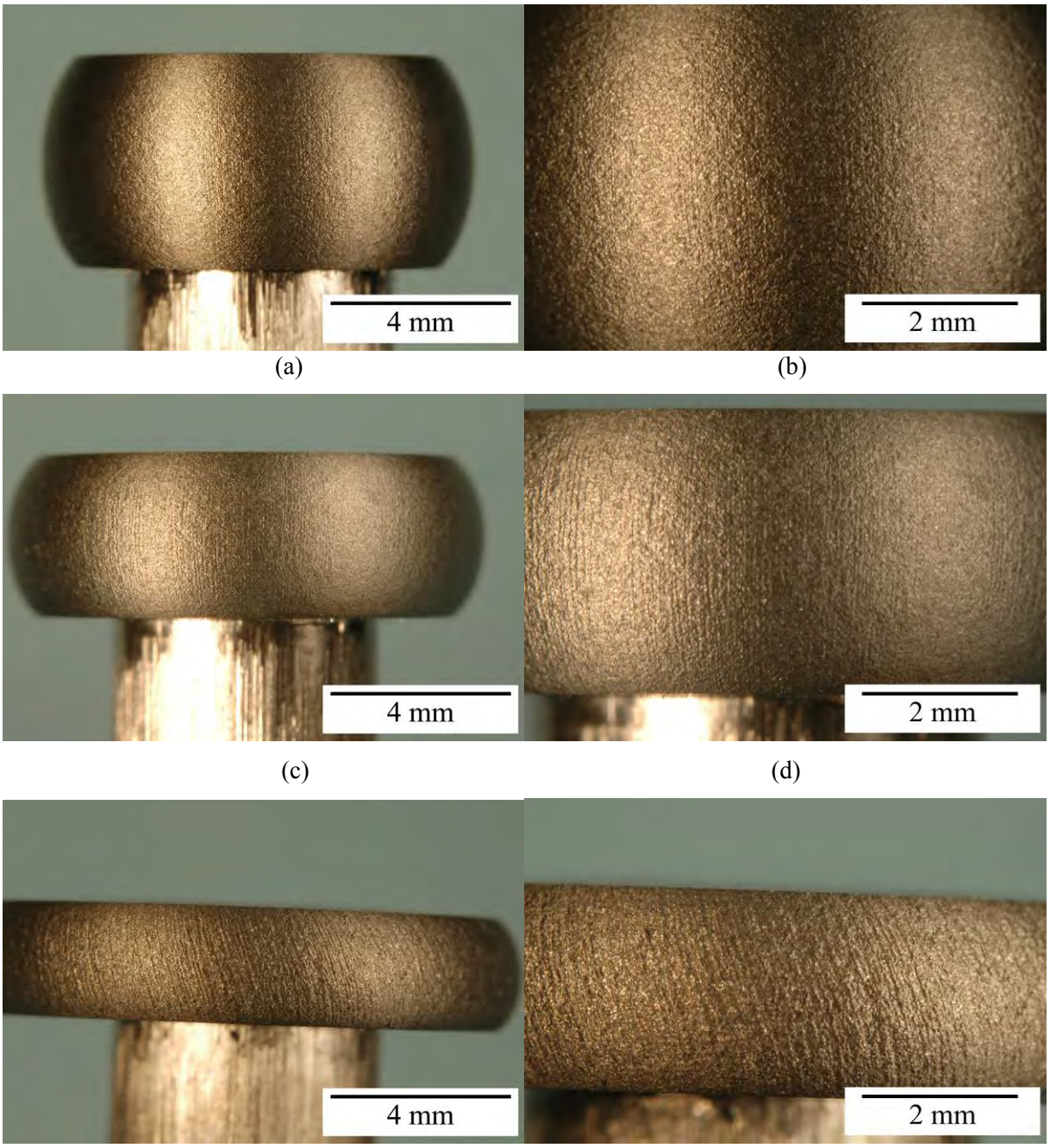

Figure 4.30 Macrographs of CR 16MnCr5 cold-headed samples at three levels of strain and two magnifications. Fracture limit is 0.91 true compressive strain. (a) and (b) 0.89 true compressive strain (c) and (d) 1.15 true compressive strain (e) and (f) 1.52 true compressive strain.

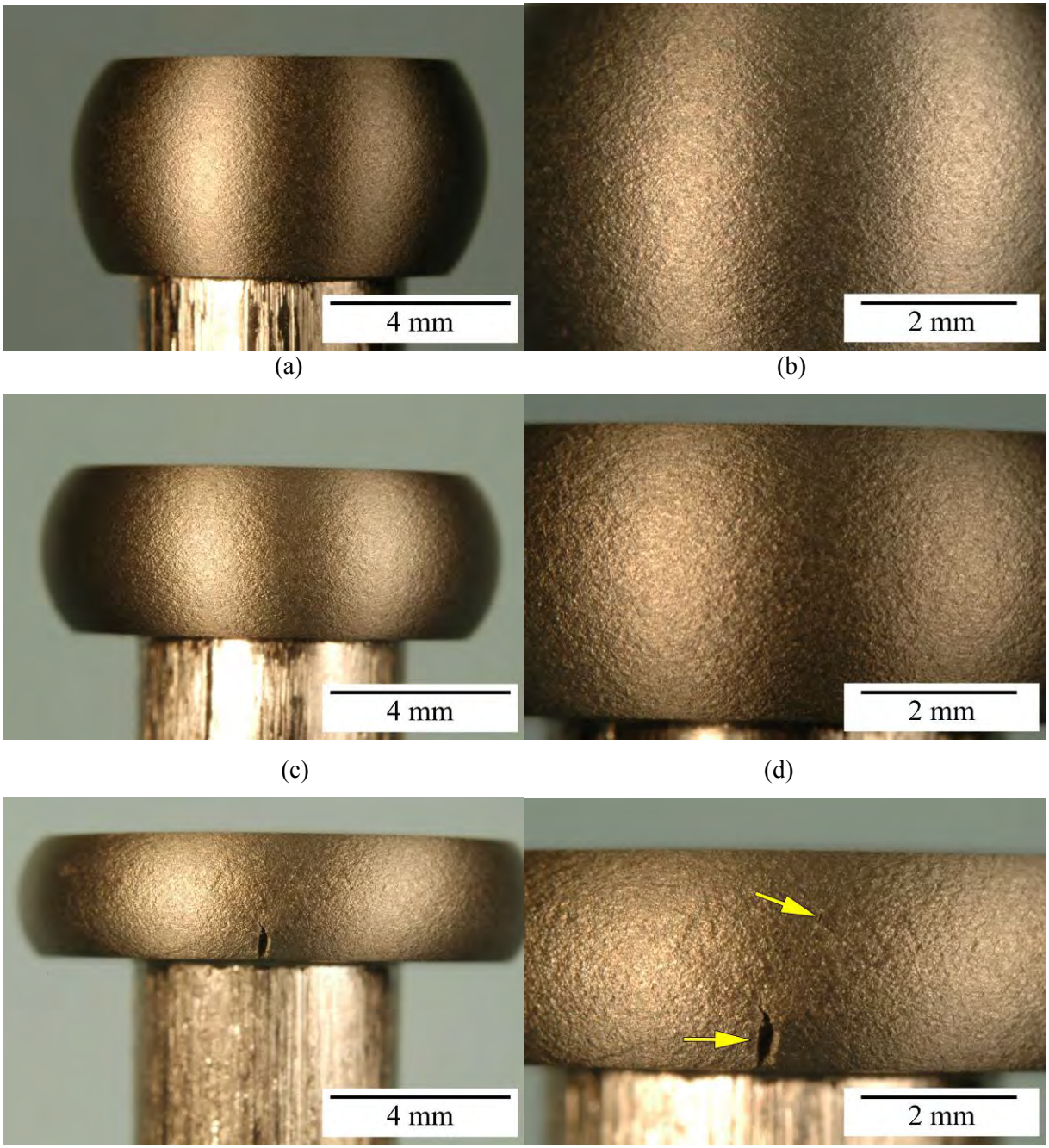

Figure 4.31 Macrographs of 1080V cold-headed samples at three levels of strain and two magnifications. Fracture limit is 0.86 true compressive strain. (a) and (b) 0.89 true compressive strain (c) and (d) 1.15 true compressive strain (e) and (f) 1.52 true compressive strain.

Contrasting the low strain level samples of the spheroidized with the normalized conditions in Figure 4.32 and Figure 4.33, respectively, shows easily visible longitudinal cracks (highlighted by arrows) for the normalized condition compared with the spheroidized condition. The number and size of longitudinal cracks increases with increasing strain in the medium and high strain levels in the normalized condition. The number and severity of cracks are greater in the normalized material compared with the spheroidized material for all levels of strain. The surface exhibits surface roughening but only to a small extent. From the micrographs, the surface is rougher for normalized samples compared to spheroidized samples.

The normalized and aged material in Figure 4.34 shows no clear cracks at the low strain level (Figure 4.34 (a) and (b)) but an easily visible longitudinal crack in the medium strain level to the left of the Figure 4.34 (d) and a mixed mode crack (longitudinal and shear) to the right of the image. Cracks are larger in the high strain level sample and are also of a mixed longitudinal and shear nature. The material exhibits a degree of surface roughening comparable to that of the normalized material. The normalized and over-aged sample set (Figure 4.35) does not show cracks at the low strain level Figure 4.35 (a) and (b) but a major longitudinal crack at the medium level strain. Interestingly, at the high level strain, multiple small cracks are observed across the sample surface. These cracks were significantly smaller than the crack in the medium level strain sample. The normalized and over-aged material also exhibited a degree of surface roughening similar to the normalized material. The normalized, the normalized and aged, and the normalized and over-aged materials have Vickers hardness values of 292, 292 and 262, respectively.

Figure 4.36 shows images from the high-temperature isothermal hold samples. A few incipient cracks (highlighted by arrows) were present in the low strain level (Figure 4.36 (a) and (b)) while multiple cracks were present in the medium strain level sample (Figure 4.36 (c) and (d)). The high strain sample (Figure 4.36 (e) and (f)) had many large mixed mode (shear and longitudinal) cracks and a very large longitudinal crack. The surface exhibited a minimal degree of surface roughening comparable to the spheroidized material and less lower than the normalized, normalized and aged, and normalized and over-aged materials.

The low-temperature isothermal hold samples showed a similar cracking behavior as the high-temperature isothermal hold sample. In Figure 4.37 (a) and (b), a few longitudinal cracks were observed and are highlighted by arrows in the high magnification image. The medium strain level sample (Figure 4.37 (c) and (d)) showed many longitudinal cracks similar to the medium level strain high-temperature isothermal hold sample. However, these cracks are larger in the low-temperature isothermal hold than in the medium strain level for the high-temperature isothermal hold sample. These cracks develop into large longitudinal cracks in the high strain level sample. The low-temperature isothermal

hold samples exhibit a surface similar to the high-temperature isothermal hold samples with a minimal surface roughening. Vickers hardness for the high and low isothermal hold heat treatment conditions are 303 and 322, respectively.

The quenched and high-temperature temper material in Figure 4.38 showed very small incipient cracks at the low strain level which are highlighted by arrows in the high magnification image (Figure 4.38 (b)) but two large longitudinal cracks at the medium strain level (Figure 4.38 (c) and (d)). The high strain level (Figure 4.38 (e) and (f)) had a larger crack than the medium strain level and also many small longitudinal cracks. The surface of the quenched and high-temperature temper material exhibits a very smooth surface with minimal surface roughening comparable to the isothermally-transformed materials.

The quenched and low-temperature temper material in Figure 4.39 exhibits subtle small incipient cracks at the low strain level (Figure 4.39 (a) and (b)) but large cracks that are of a mixed shear-longitudinal character for the medium strain level. The high strain level sample (Figure 4.39 (e) and (f)) has large and small longitudinal cracks. The quenched and low-temperature materials exhibited minimal surface roughening similar to the quenched and high-temperature temper material. Vickers hardness for the quenched and high and low temperature temper conditions are 304 and 320, respectively.

By contrasting surfaces of the heat-treated 10V45 materials in Figure 4.32 through Figure 4.39, the degree of surface roughening is low and comparable for the spheroidized, isothermally-transformed and quenched and tempered materials as smooth surfaces are observed for these materials. The normalized, normalized and aged, and normalized and over-aged materials exhibit a greater degree of surface roughening in comparison to the rest of the 10V45 w/Nb heat-treated materials. However, the surface roughening is not as severe as seen in the as-received material for any of the heat-treated materials.

Table 4.3 – Summary of Fracture Limit, Yield Stress and Hardness Data for Heat-treated 10V45 w/Nb Samples

Material	Fracture Limit (True Compressive Strain)	Yield Stress (MPa)	Hardness (Vickers)
As-received	0.69±0.16	673±12.1	275±3.7
Spheroidized	cracks as low as 0.57	599±15.6	194±4.1
Normalized	cracks as low as 0.57	832±12.7	292±5.2
Normalized and Aged	cracks as low as 0.57	838±3.2	292±3.3
Normalized and Over-aged	cracks as low as 0.57	726±9.9	262±2.7
High Temperature Isothermal Hold	cracks as low as 0.49	885±22.7	303±3.5
Low Temperature Isothermal Hold	cracks as low as 0.49	905±2.1	322±2.4
Quenched and High-Temperature Temper	cracks as low as 0.49	1013±11.2	304±5.0
Quenched and Low-Temperature Temper	cracks as low as 0.49	1116±18.4	320±2.0

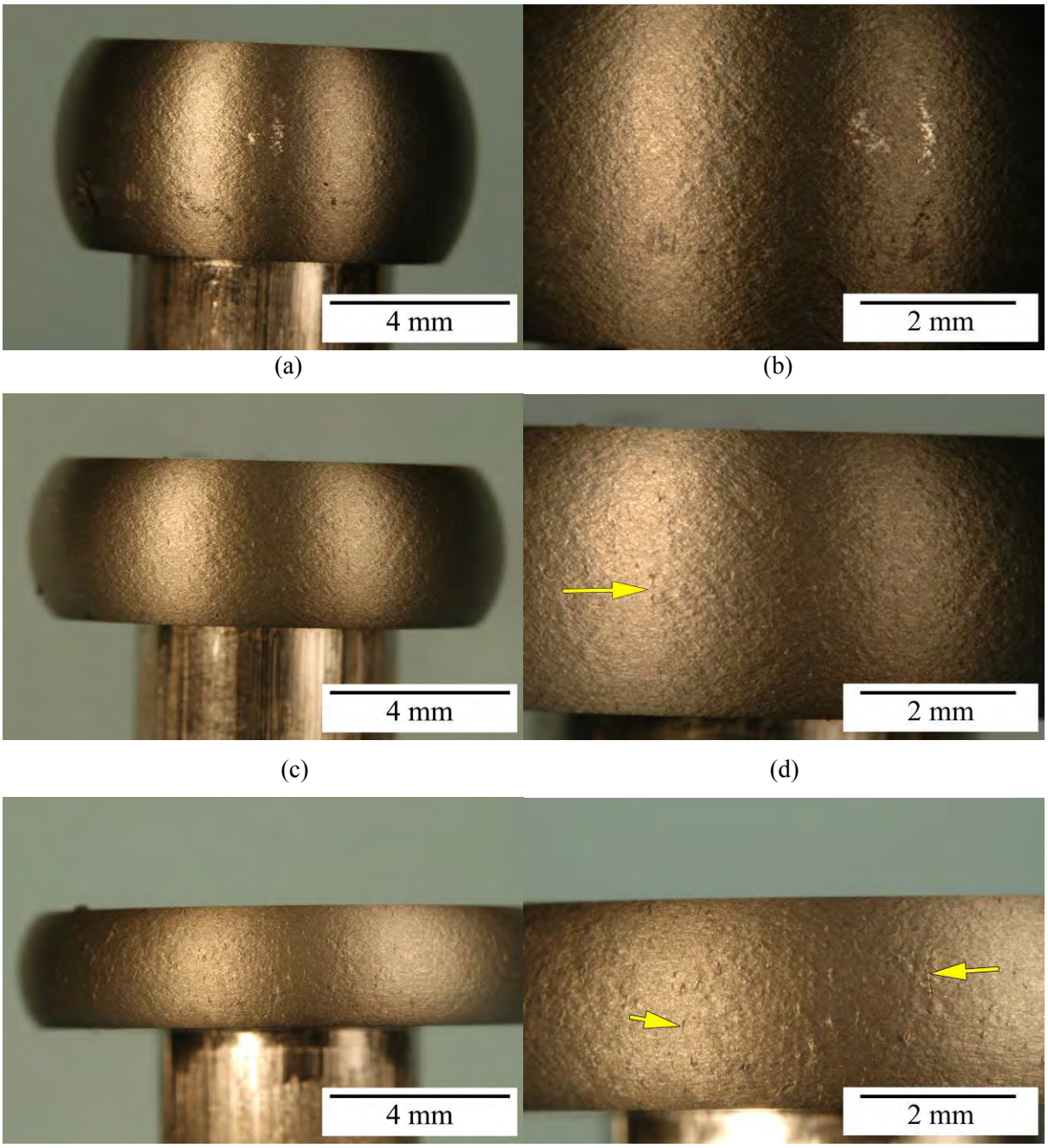

Figure 4.32 Macrographs of spheroidized (austenitized at a 1000 °C for an hour, water quenched, heated to 700 °C for 48 hours and air cooled) 10V45 w/Nb cold-headed samples at three levels of strain and two magnifications. Cracks are observed at 20X on a stereo microscope at a strain level as low as 0.57 true compressive strain. (a) and (b) 0.89 true compressive strain (c) and (d) 1.15 true compressive strain (e) and (f) 1.52 true compressive strain.

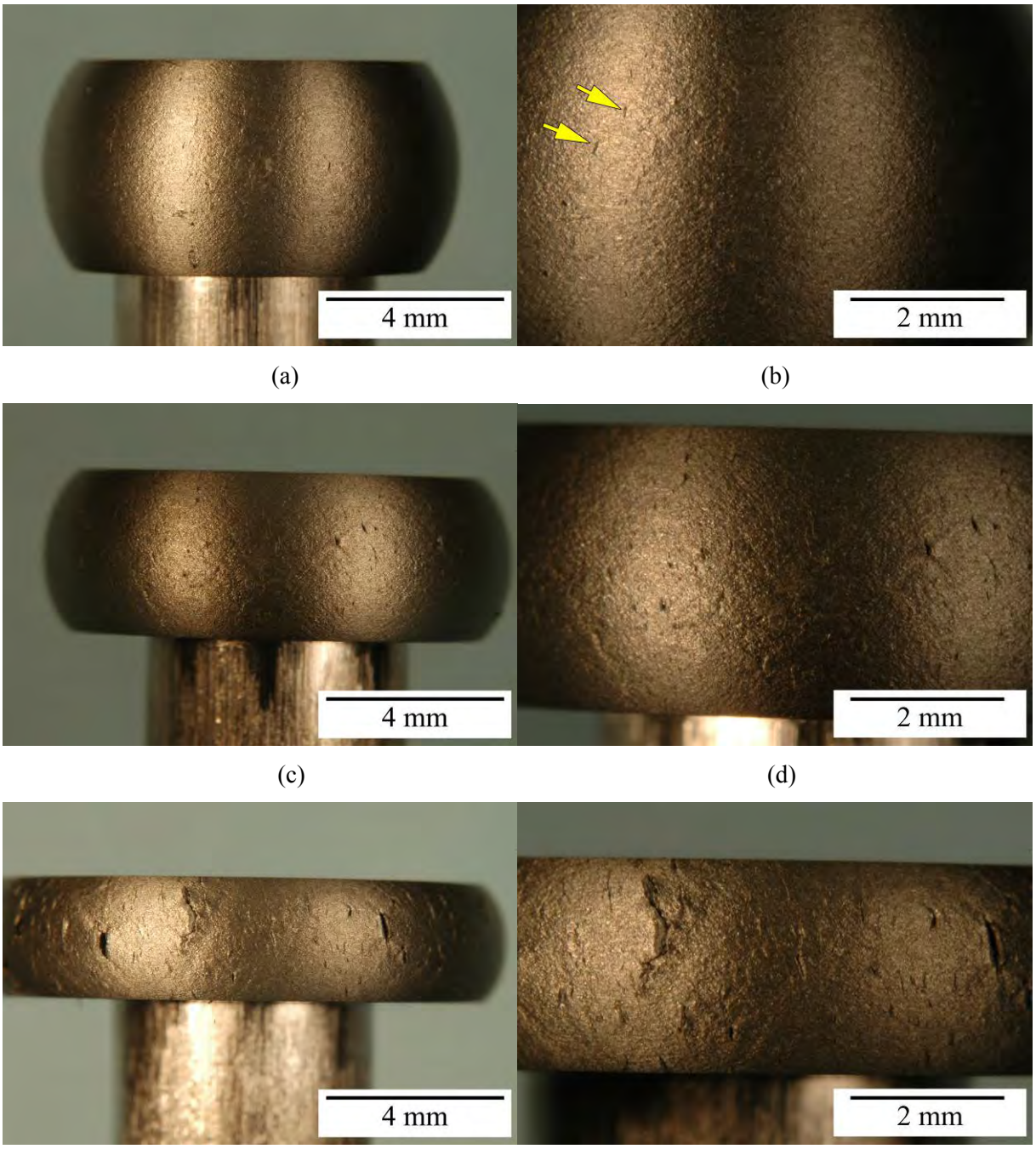

Figure 4.33 Macrographs of normalized (austenitized at 1000 °C for an hour and air cooled) 10V45 w/Nb cold-headed samples at three levels of strain and two magnifications. Cracks are observed at 20X on a stereo microscope at a strain level as low as 0.57 true compressive strain. (a) and (b) 0.89 true compressive strain (c) and (d) 1.15 true compressive strain (e) and (f) 1.52 true compressive strain.

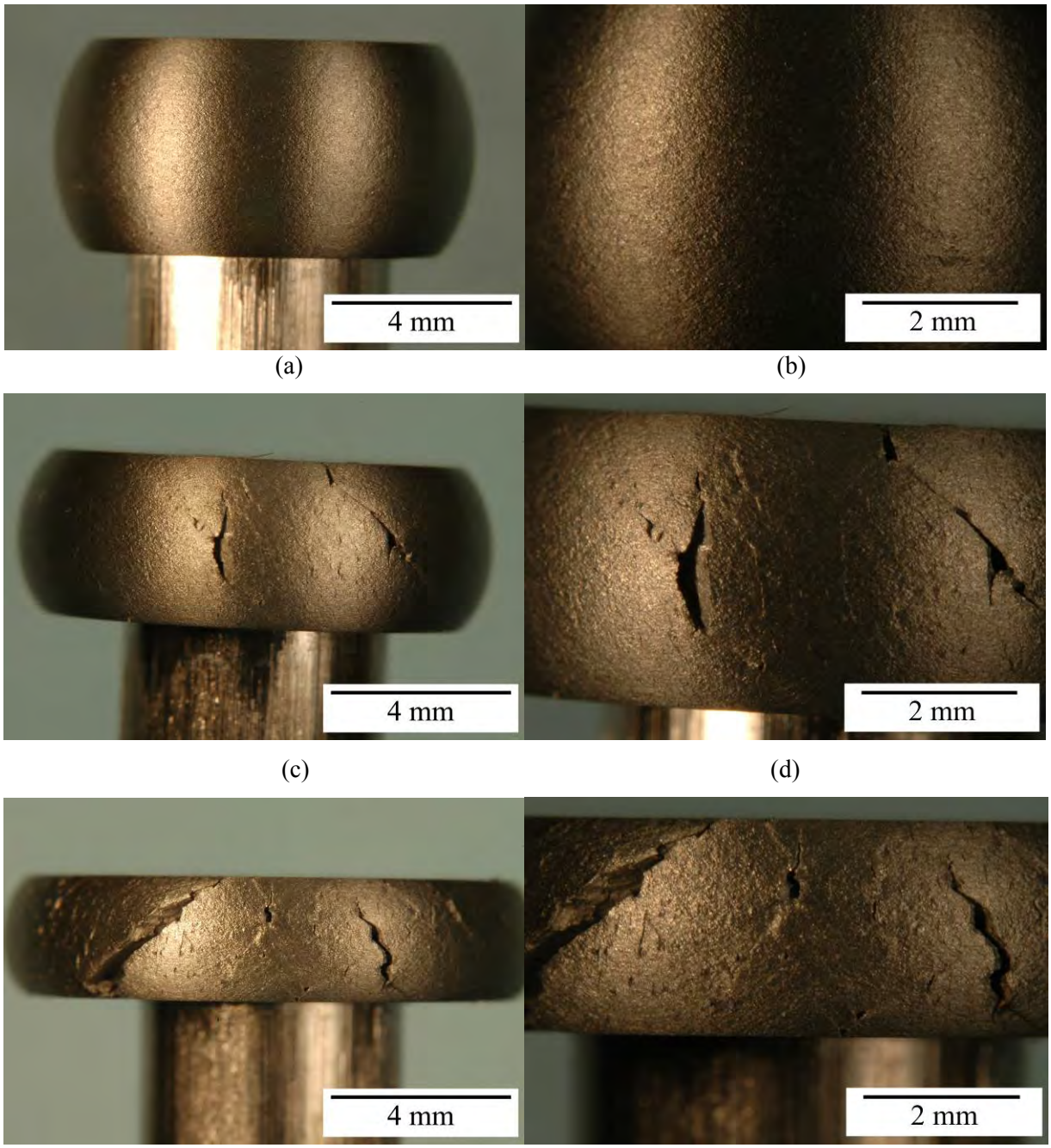

Figure 4.34 Macrographs of normalized and aged (austenitized at 1000 °C for an hour, air cooled, heated to 625 °C for an hour and air cooled) 10V45 w/Nb cold-headed samples at three levels of strain and two magnifications. Cracks are observed at 20X on a stereo microscope at a strain level as low as 0.57 true compressive strain. (a) and (b) 0.89 true compressive strain (c) and (d) 1.15 true compressive strain (e) and (f) 1.52 true compressive strain.

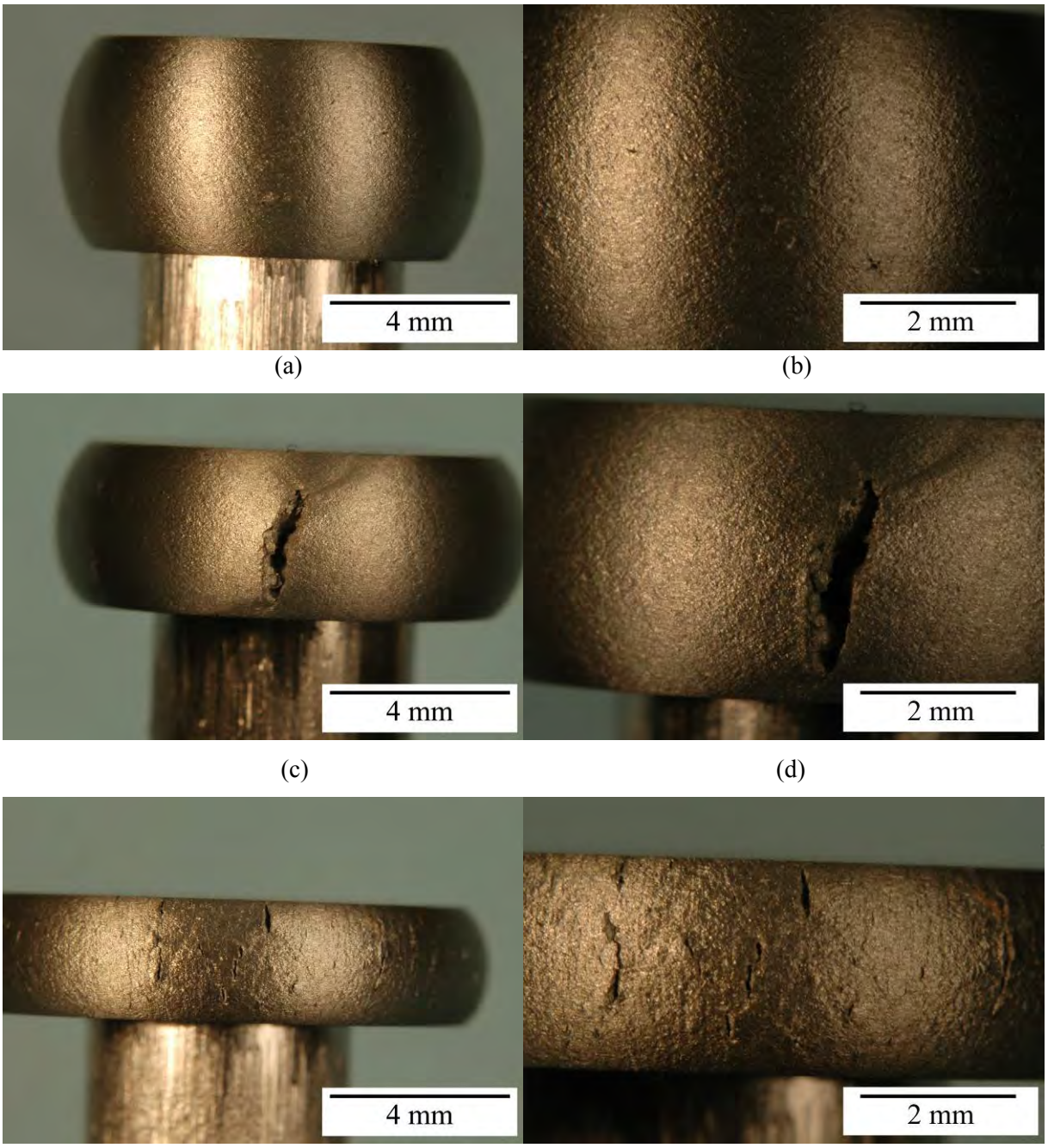

Figure 4.35 Macrographs of normalized and over-aged (austenitized at 1000 °C for an hour, air cooled, heated to 675 °C for an hour and air cooled) 10V45 w/Nb cold-headed samples at three levels of strain and two magnifications. Cracks are observed at 20X on a stereo microscope at a strain level as low as 0.57 true compressive strain. (a) and (b) 0.89 true compressive strain (c) and (d) 1.15 true compressive strain (e) and (f) 1.52 true compressive strain.

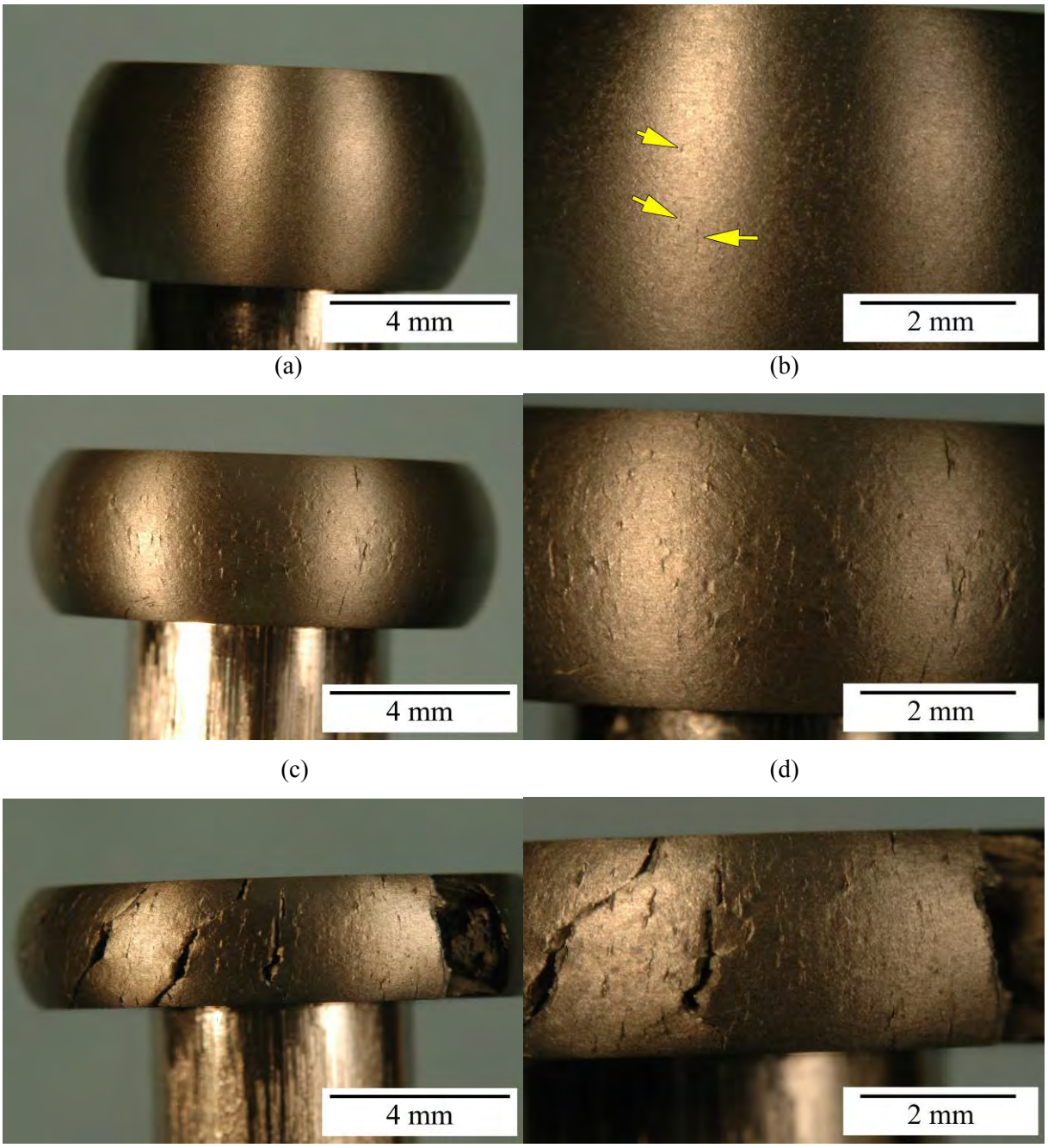

Figure 4.36 Macrographs of higher-temperature isothermal hold (austenitized at 866 °C for 10 minutes, rapidly cooled to 435 °C and held for 20 minutes and air cooled) 10V45 w/Nb cold-headed samples at three levels of strain and two magnifications. Cracks are observed at 20X on a stereo microscope at a strain level as low as 0.49 true compressive strain. (a) and (b) 0.89 true compressive strain (c) and (d) 1.15 true compressive strain (e) and (f) 1.52 true compressive strain.

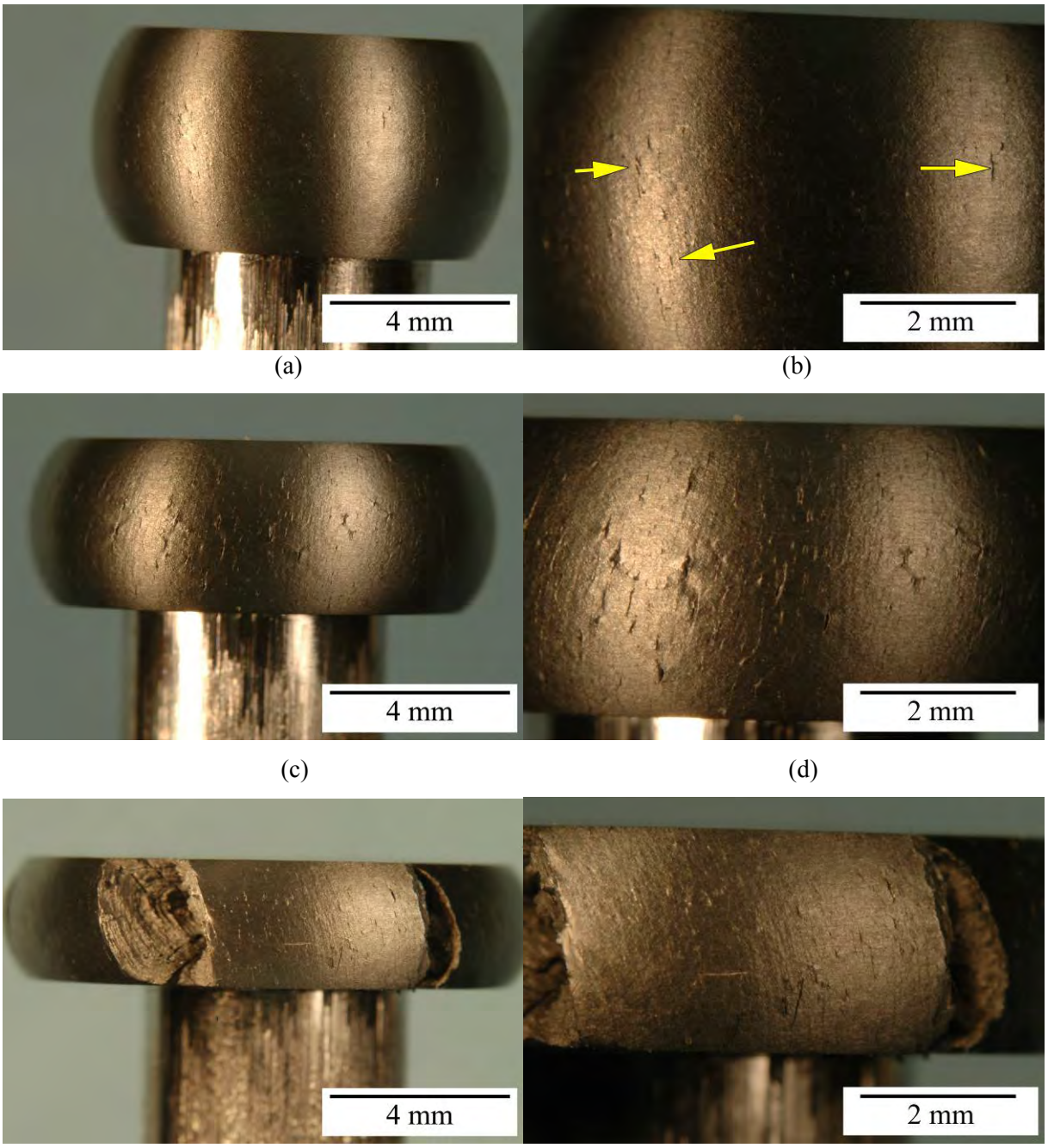

Figure 4.37 Macrographs of lower-temperature isothermal hold (austenitized at 866 °C for 10 minutes, rapidly cooled to 365 °C and held for 20 minutes and air cooled) 10V45 w/Nb cold-headed samples at three levels of strain and two magnifications. Cracks are observed at 20X on a stereo microscope at a strain level as low as 0.49 true compressive strain. (a) and (b) 0.89 true compressive strain (c) and (d) 1.15 true compressive strain (e) and (f) 1.52 true compressive strain.

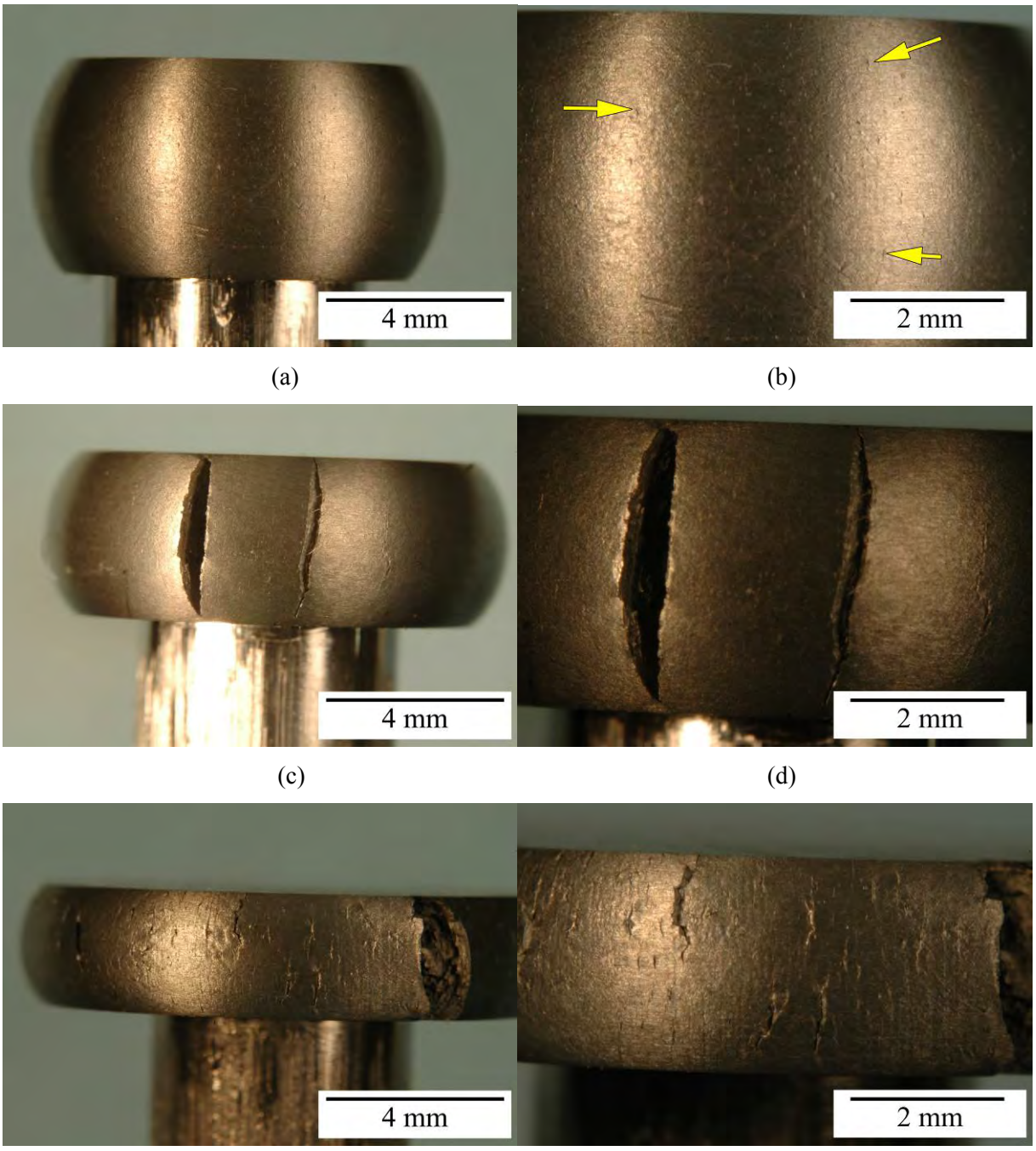

Figure 4.38 Macrographs of quenched and higher-temperature temper (austenitized at 870 °C for 10 minutes, water quenched, tempered at 615 °C for two hours and air cooled) 10V45 w/Nb cold-headed samples at three levels of strain and two magnifications. Cracks are observed at 20X on a stereo microscope at a strain level as low as 0.49 true compressive strain. (a) and (b) 0.89 true compressive strain (c) and (d) 1.15 true compressive strain (e) and (f) 1.52 true compressive strain.

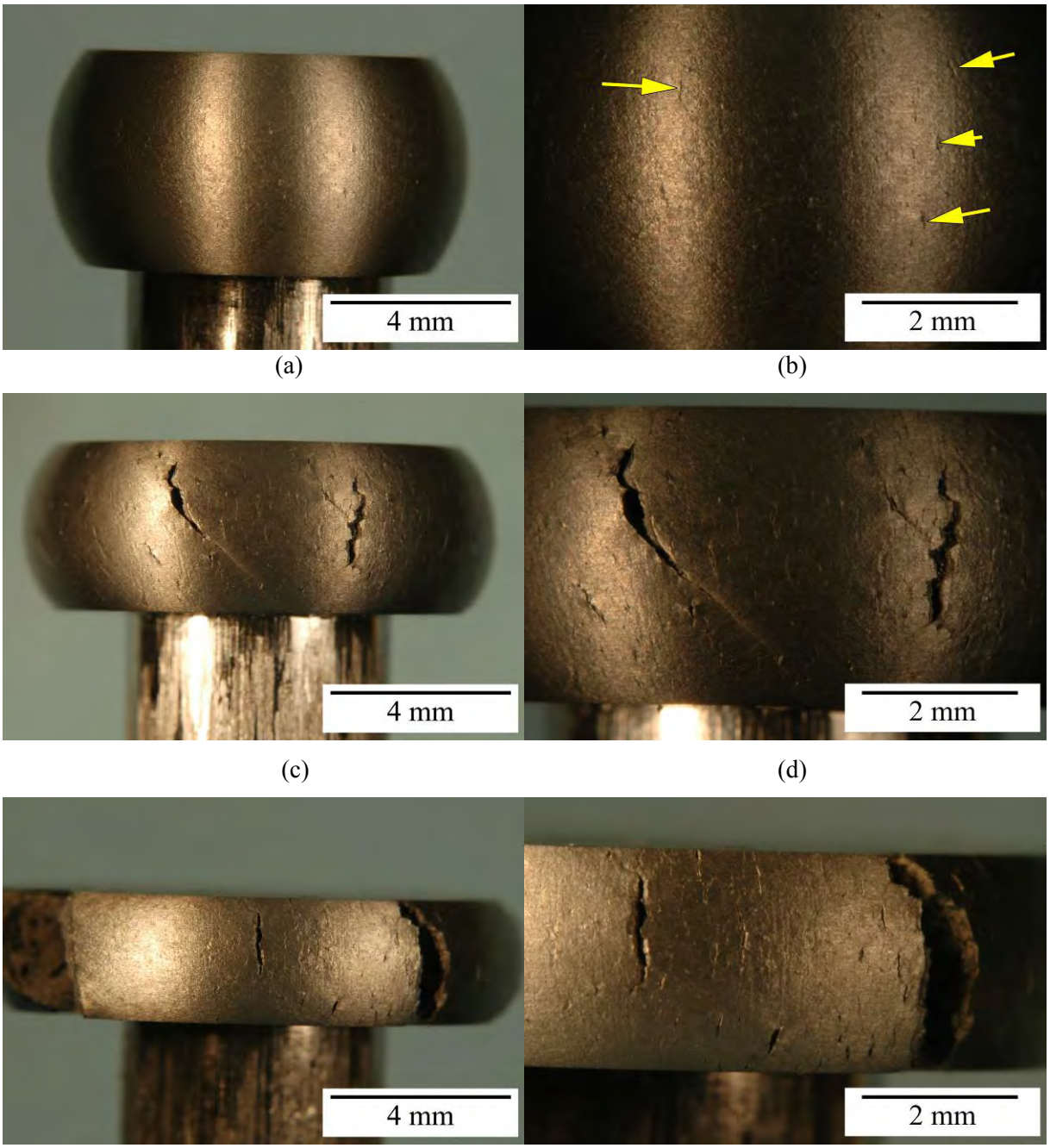

Figure 4.39 Macrographs of quenched and lower-temperature temper (austenitized at 870 °C for 10 minutes, water quenched, tempered at 590 °C for two hours and air cooled) 10V45 w/Nb cold-headed samples at three levels of strain and two magnifications. Cracks are observed at 20X on a stereo microscope at a strain level as low as 0.49 true compressive strain. (a) and (b) 0.89 true compressive strain (c) and (d) 1.15 true compressive strain (e) and (f) 1.52 true compressive strain.

4.6 Grain Flow and Stress-Strain Curves

The grain flow pattern associated with the developed testing procedure and conditions is shown in the macro-etched macrographs in Figure 4.40. The figure contains images of two 1045 Al cold-headed samples deformed to 1.15 and 1.52. The samples were longitudinally sectioned through the center and macroetched in a solution of 50 vol pct hydrochloric acid and 50 vol pct dionized water at approximately 75 °C. Both samples exhibit a symmetric deformation pattern confirming the efficacy of the removal of residual oil for a symmetric deformation behavior. Strain lines indicate the presence of a 'dead metal zone' at the top and bottom of the deformed height of the sample due to high friction conditions. The deformation is concentrated at the outer surface of the sample and the midplane of the deformed height.

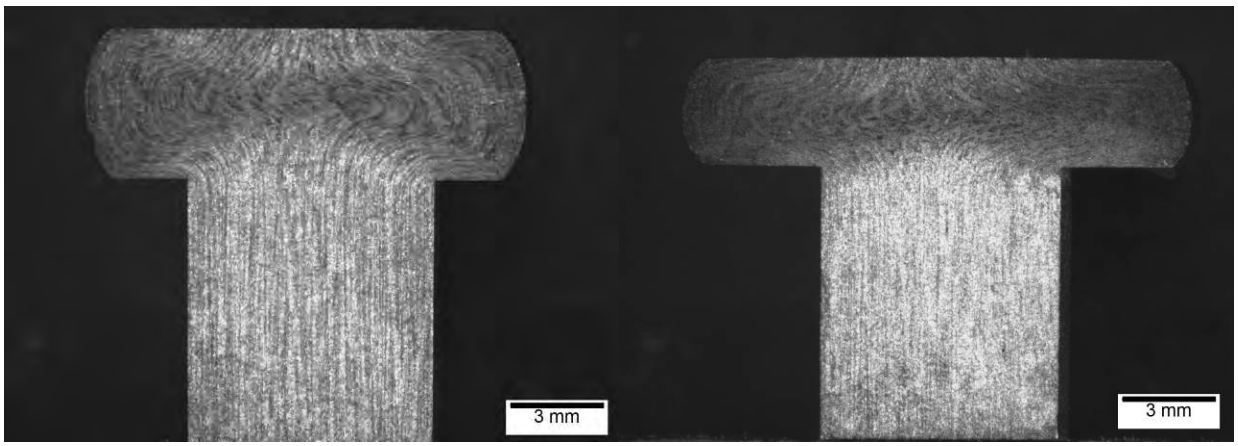

(a) (b)

Figure 4.40 Stereo microscope images of 1045 Al samples cold headed at 15 mm/s to (a) 1.15 and (b) 1.52 true compressive strains. Samples were longitudinally sectioned and macroetched in a solution of 50 vol pct HCl and 50 vol pct DI water at a temperature range between 70 and 80 °C.

Figure 4.41 through Figure 4.44 are a series of representative true stress-strain curves generated from data collected from cold heading tests from the different families of as-received and heat-treated materials. The figures show initial deformation up to 0.2 true strain to illustrate the differences in yielding and flow behavior. Figure 4.41 shows true stress-strain curves for as-received 1045 materials. All the materials exhibit discontinuous yielding behavior. The data divide into two groups. The microalloyed steels (10V45 and 10V45 w/Nb in both hot-rolled and TMP conditions exhibit strengths that are approximately 200MPa greater than the 1045 Al steels. The hot-rolled and thermomechanically processed 1045 Al materials exhibit essentially identical yield stresses and flow curves. For the microalloyed steels, the yield strength and stress-strain curve shapes are essentially independent of processing with the 10V45 steel exhibiting overall average higher strengths.

Figure 4.42 contains representative true stress-strain curves of 41XX materials. Hot-rolled materials have the highest yield and flow stresses while spheroidized materials have the lowest yield and flow stresses. The properties of the pre-drawn 41XX materials are between hot-rolled and spheroidized materials with respect to yield and flow stresses. The spheroidized materials are the only steels in this family of materials that exhibit discontinuous yielding behavior. For the 4135 and 4140 alloys, pre-drawing causes a significant decrease in yield and flow stresses while pre-drawn PL41 does not differ much from hot-rolled PL41 with respect to yield and flow stresses. Specific to the spheroidized materials, 4135 and PL41 have very comparable yield and flow stresses while 4140 has a higher yield stress but similar flow stress compared with the rest of the spheroidized materials.

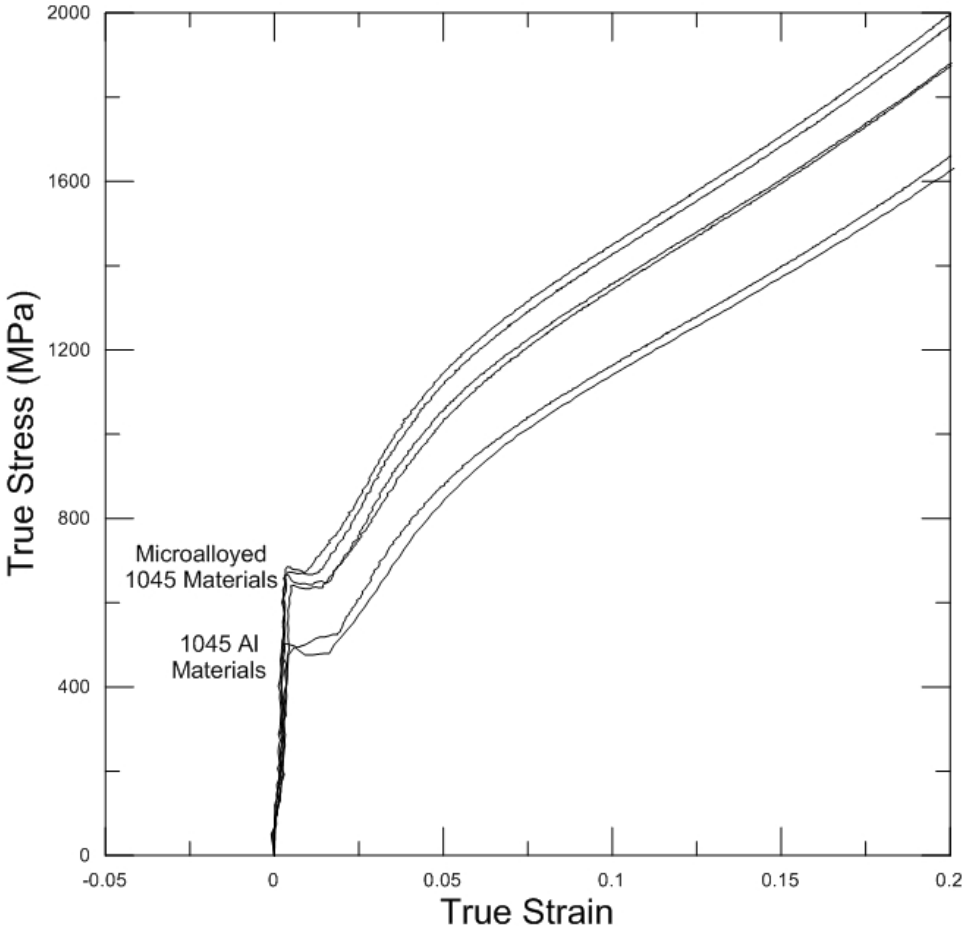

Figure 4.41 True stress-strain curves for representative samples of the 1045 series.

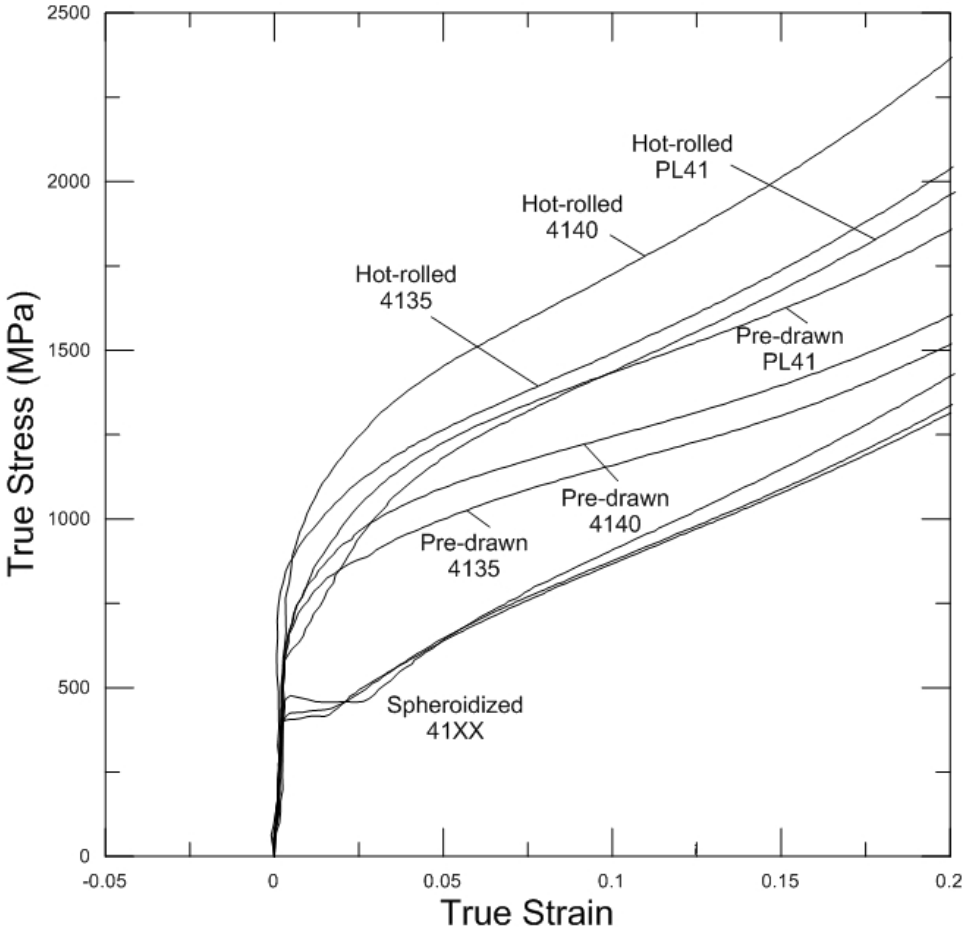

Figure 4.42 True stress-strain curves for representative samples of the 41XX series.

Figure 4.43 shows true stress-strain curves for the low and high carbon materials. The hot-rolled 16MnCr5 has a higher yield and flow stress than the control-rolled 16MnCr5. The 1080V (high carbon steel) has the highest yield (893 MPa) and flow curve out of all the as-received materials. All of these materials exhibited continuous yielding behavior.

Figure 4.44 summarizes the true stress-strain curves for all 10V45 w/Nb heat-treated materials in addition to the as-received material. Irrespective of processing history, all processing conditions resulted in material with discontinuous yielding and all yield stresses are summarized in Table 4.3. The spheroidized material has the lowest yield and flow stresses. The materials arranged in terms of the increasing yield stress are the spheroidized, as-received, normalized and over-aged, normalized, normalized and age-hardened, higher isothermal hold, lower isothermal hold, quenched and higher temperature temper and quenched and lower temperature temper. The as-received material and the normalized and over-aged material have similar yield stresses with the normalized and over-aged being slightly higher. Yield stress and flow curves are also close for the normalized and aged material and the normalized material with the normalized and aged material having a slightly higher yield stress. The two

austenitized and isothermally-transformed materials have similar flow curves to the quenched and tempered materials despite the yield stresses being significantly lower than the two quench and temper materials. The yield stress for the quenched and lower temper material (the highest yield stress) is greater than two times the yield stress for the spheroidized material while the remaining materials exhibit strengths between these two materials.

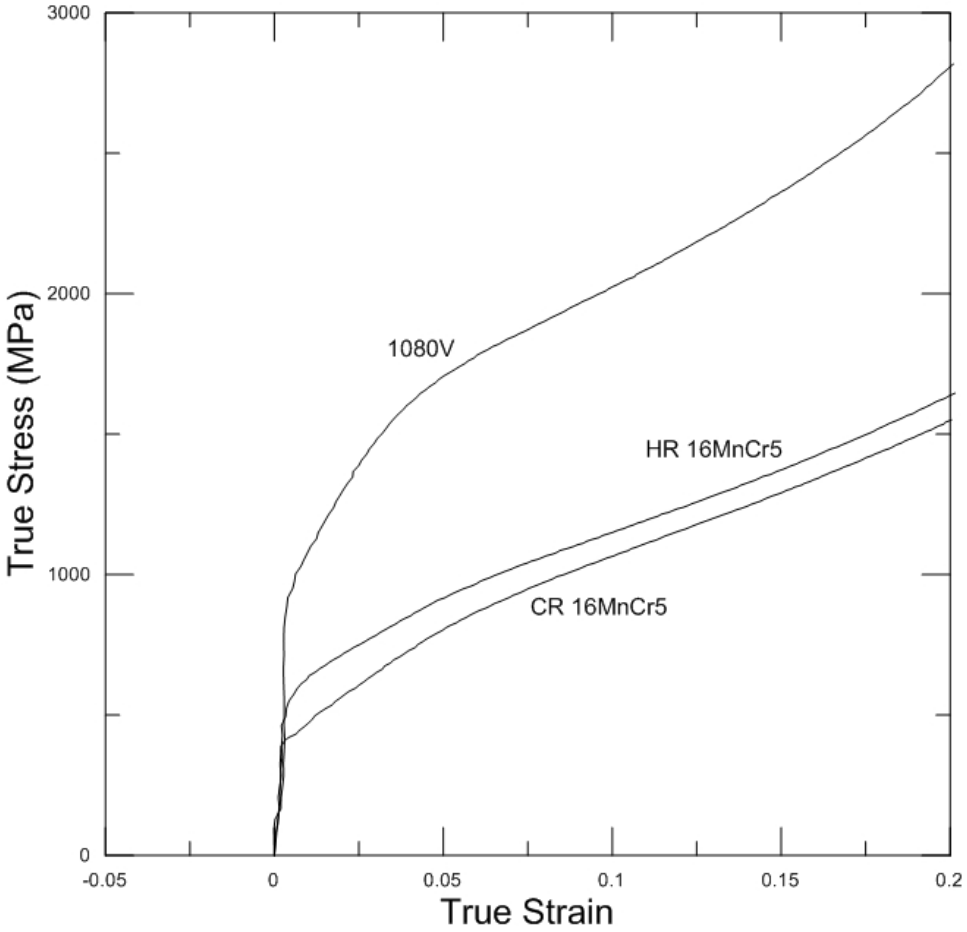

Figure 4.43 True stress-strain curves for representative samples of the low and high carbon materials (HR and CR 16MnCr5 and 1080V).

4.1 Fractography and Fracture Analysis

SEM fractography was carried out on selected samples representing all the different classes of materials. Figure 4.45 to Figure 4.46 are low and high magnification fractographs of three samples illustrating typical characteristics frequently observed of visibly open cracks on the surface. Dimples characteristic of ductile fracture by void nucleation, growth and coalescence were the main theme for all materials. Traces of manganese sulfide inclusions were verified in the 1045 Al and quenched and

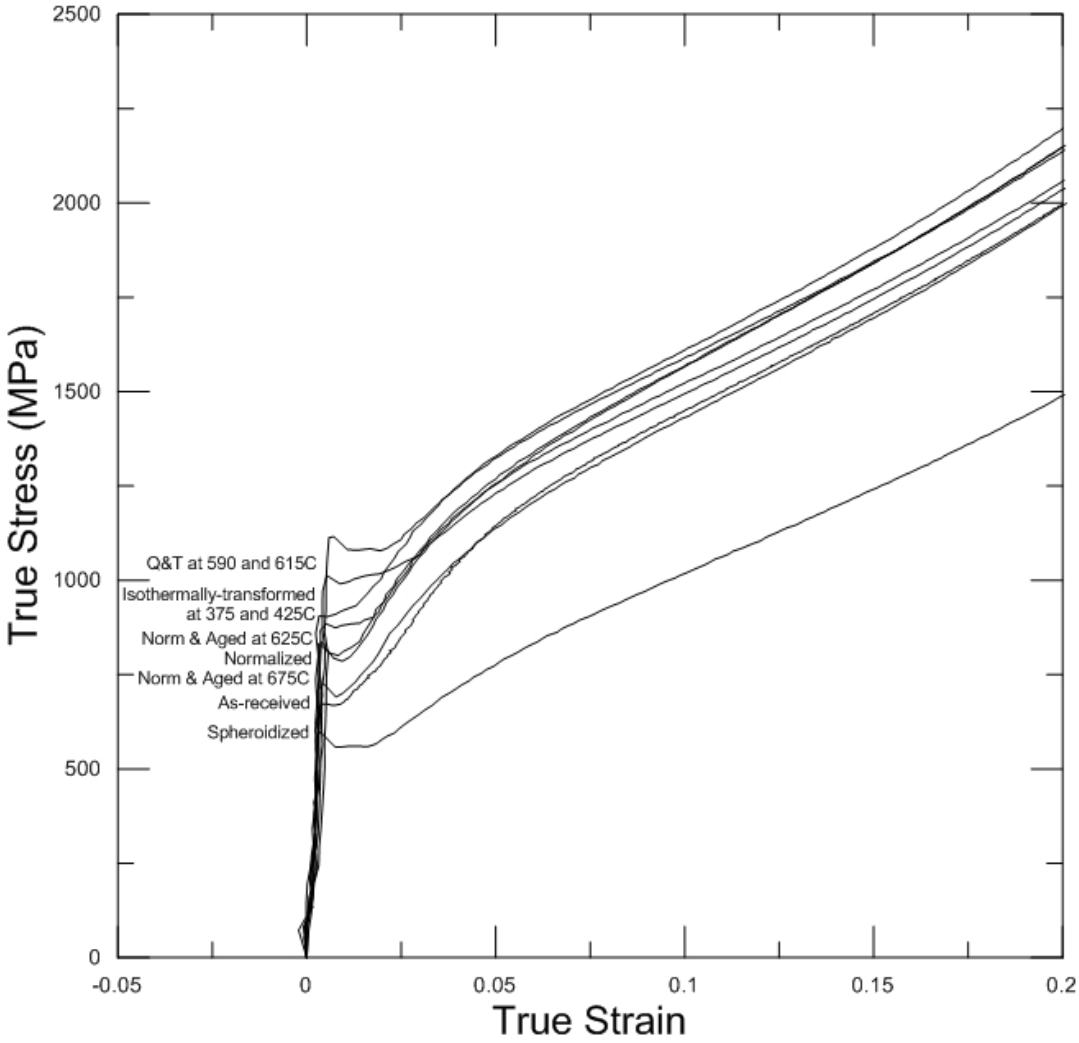

Figure 4.44 True stress-strain curves for representative samples of the heat-treated 10V45 w/Nb materials.

and Figure 4.46 and are highlighted by arrows. For the 1045 Al sample in Figure 4.45, traces of the inclusion are broken from their original form in the steel while in Figure 4.46 of the heat-treated 10V45 w/Nb material, the inclusion stringers are evident and continuous on the fracture surface and elongated along the rolling direction as frequently observed in the microstructure. In Figure 4.46 (b), equiaxed dimples are observed in between inclusions but not at inclusion-steel interfaces. Flow lines are observable in the low magnification image (Figure 4.46 (a)) on the fractured surface that shows a similar pattern than that observed in macroetched samples in Figure 4.40.

Figure 4.47 shows a fractured pre-drawn 4140 material. Longitudinal surface features can be seen on the surface in the low magnification image (Figure 4.47 (a)) and are highlighted by arrows. The crack is longitudinal parallel to the longitudinal surface features. At higher magnification (Figure 4.47 (b)) dimples are observed on the fractured surface. This mode of cracking along elongated surface features

was observed at strains slightly higher than the fracture limits. However, such cracks are of lesser severity. Figure 4.48 shows a shear crack from a hot-rolled 4140 sample. Macrographs of this sample are available in Figure 4.23 (c) and (d). Shear bands parallel and perpendicular to the shear crack and longitudinal stress relief features are highlighted by arrows in the figure. Specific to 41XX materials, shear cracks are observed exclusively in the hot-rolled 4140 material. In other materials, cracks were mostly longitudinal and along longitudinal surface features, when present. Both types of cracks are ductile as dimples are always observed on fractured surfaces.

Due to the low fracture limits of the as-received 1045 materials (0.63 to 0.85 true compressive strain) and heat-treated 10V45 w/Nb materials (fracture limits less than 0.57 true compressive strain) compared to 41XX materials, special attention was given to understanding the cracking mechanism in these materials. The relationship between microstructure and crack nucleation and path was evaluated by removing, via grinding and polishing, one half of the upset height. The samples were mounted, polished and etched and the surface locations that corresponded to initially visible cracks were identified and evaluated. Results are overviewed to illustrate the progression stages for crack nucleation and propagation.

Early stages of void nucleation were observed to occur close to the free surface, not exclusively at the surface, predominantly at inclusion sites. Void nucleation occurs by decohesion of the inclusion-metal interface and the formation of a consequent void, breaking of an inclusion or a mixture of these two mechanisms. An example of void nucleation by decohesion of the inclusion metal interface is shown in Figure 4.49 in a normalized 10V45 w/Nb sample (macrographs available in Figure 4.34 (c) and (d)). The inclusion is separated from the proeutectoid ferrite grain by a thin distance indicating early onset of void nucleation. A part of the inclusion is also broken near its top in the image. Note that the inclusion is quite close to the surface but not at the surface. An example of an inclusion breaking to form a void can be seen in Figure 4.50 of a normalized and aged 10V45 w/Nb sample (macrographs available in Figure 4.35 (e) and (f)). A micrograph containing examples of both mechanisms can be found in Figure 4.51 of a spheroidized 10V45 w/Nb sample (macrograph available in Figure 4.32 (e) and (f)). The figure shows a broken inclusion at the surface and void nucleation by decohesion of the inclusion-metal interface away from the surface. Figure 4.52 also shows a crack at the surface and many instances of void nucleation away from the surface. It should be noted that there were a few instances in which it was difficult to locate traces of inclusion at voids as can be seen in Figure 4.53 of a 10V45 w/Nb quenched and high temperature temper condition (macrographs available in Figure 4.38 (e) and (f)) where a void nucleates sub-surface. However, an overwhelming majority of voids are observed to occur at inclusion sites. It is probable that inclusions in these cases were broken and deformed to a point where it is not detectable or that the decohesion mechanism had progressed far enough to a point where the inclusion was no longer in

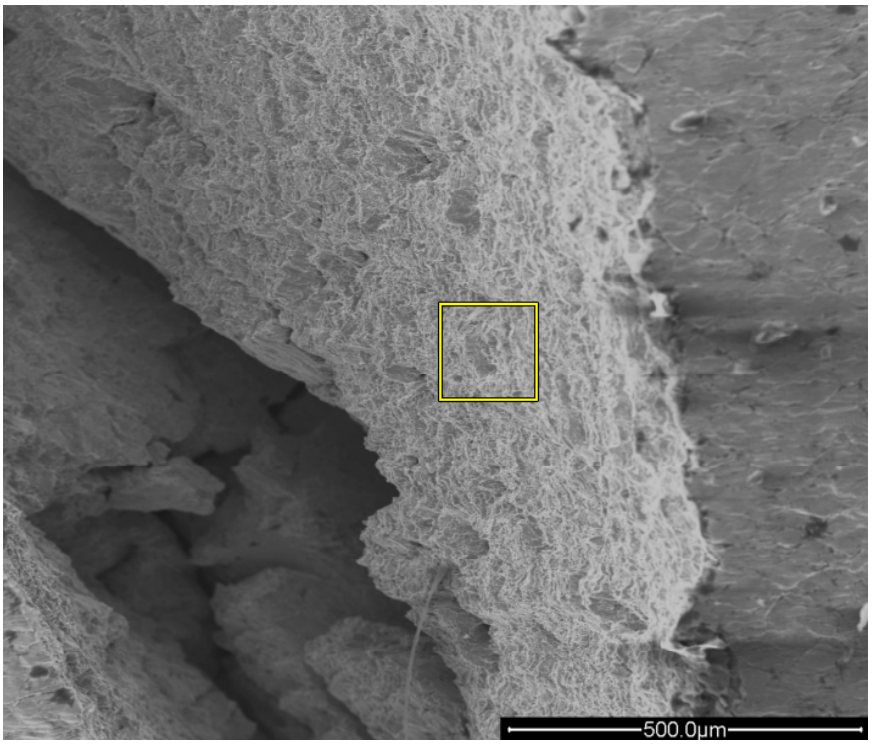

(a)

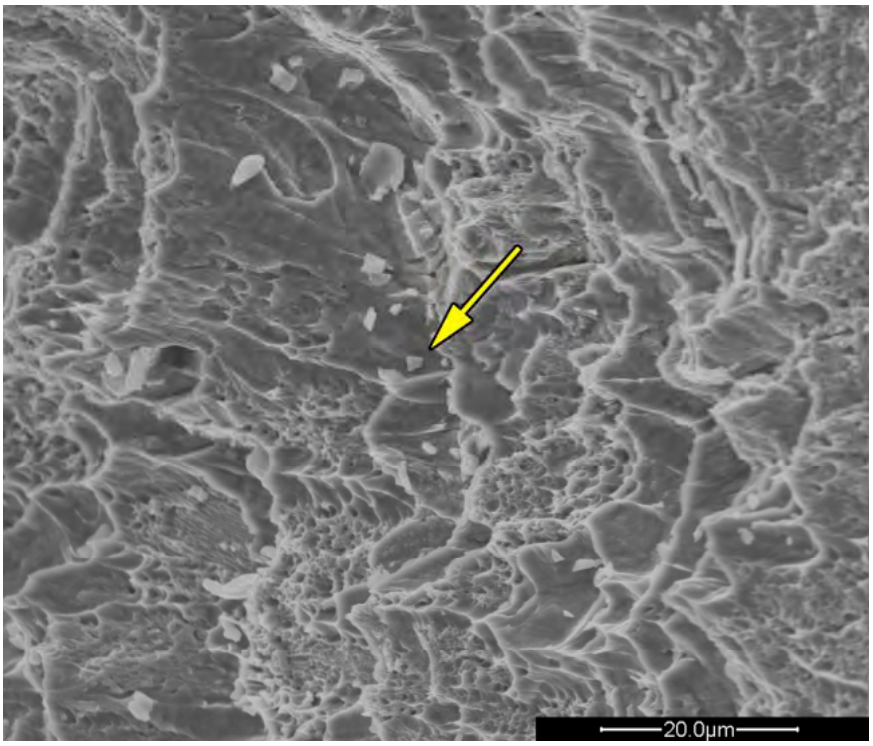

(b)

Figure 4.45 (a) Low and (b) high magnification SEM fractographs of a cold headed 1045 Al sample. Area boxed in (a) is magnified in (b) A trace of an MnS inclusion was verified in (b) and is highlighted by the arrow. Axis of loading is vertical.

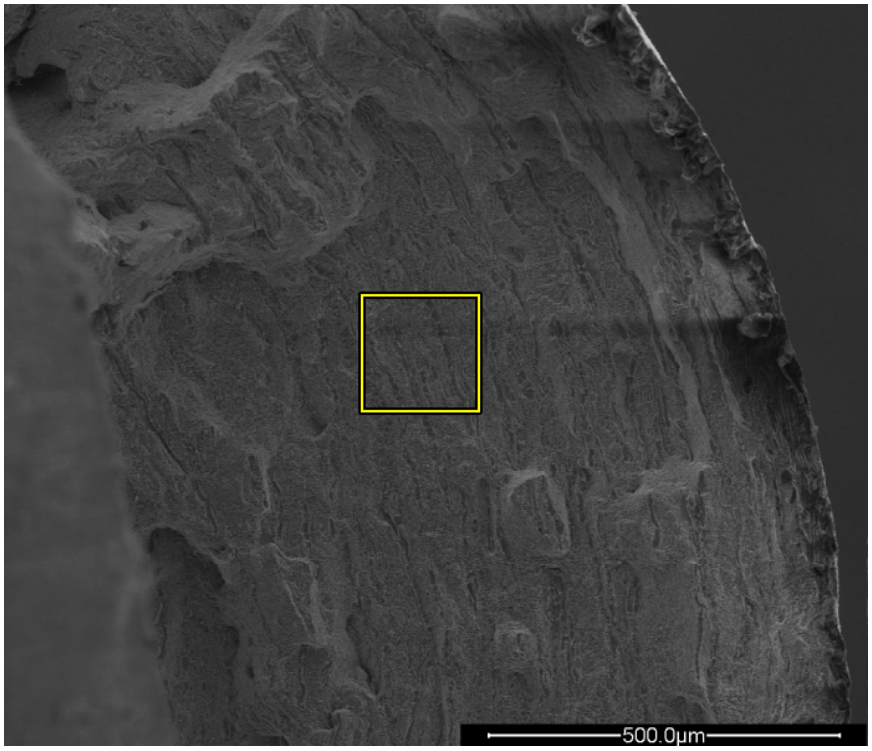

(a)

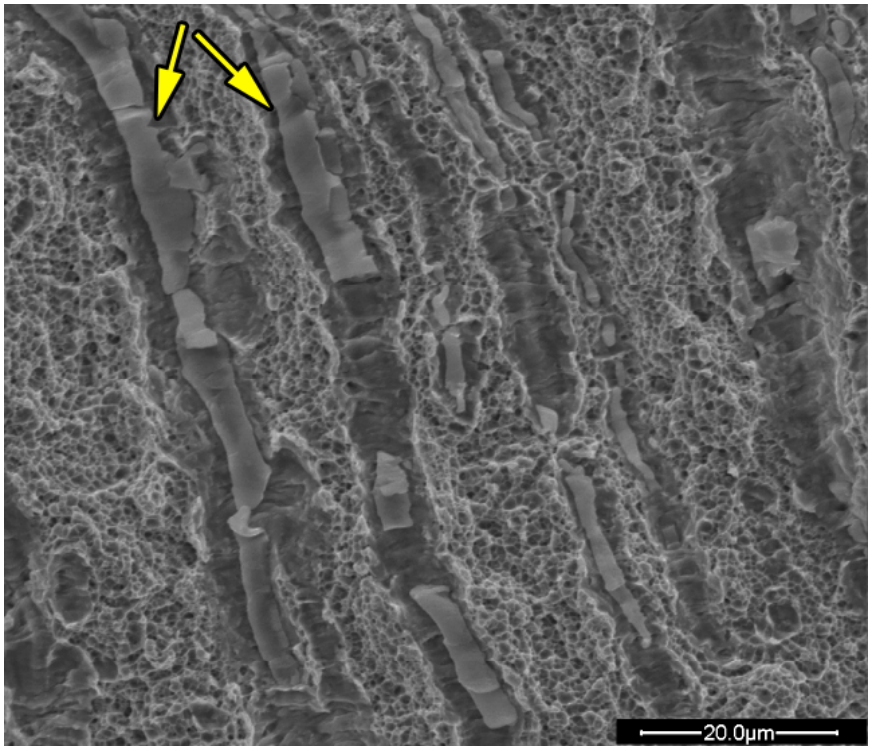

(b)

Figure 4.46 (a) Low and (b) high magnification SEM fractographs of a cold-headed heat-treated 10V45 w/Nb sample (quenched and high temperature temper). Area boxed in (a) is magnified in (b). Manganese sulfide inclusions have been verified in (b). Axis of loading is vertical.

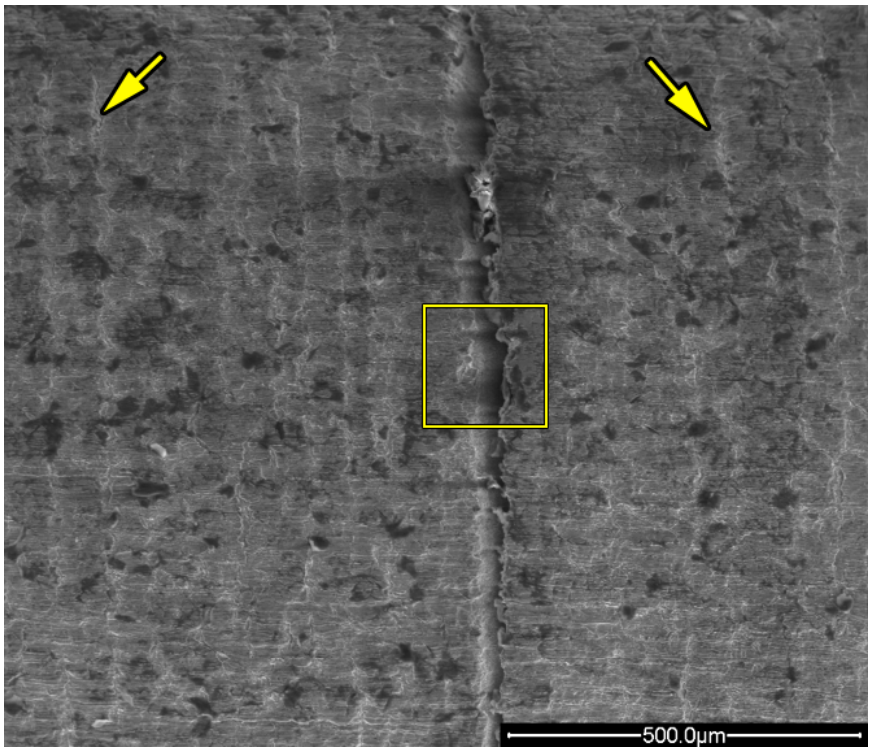

(a)

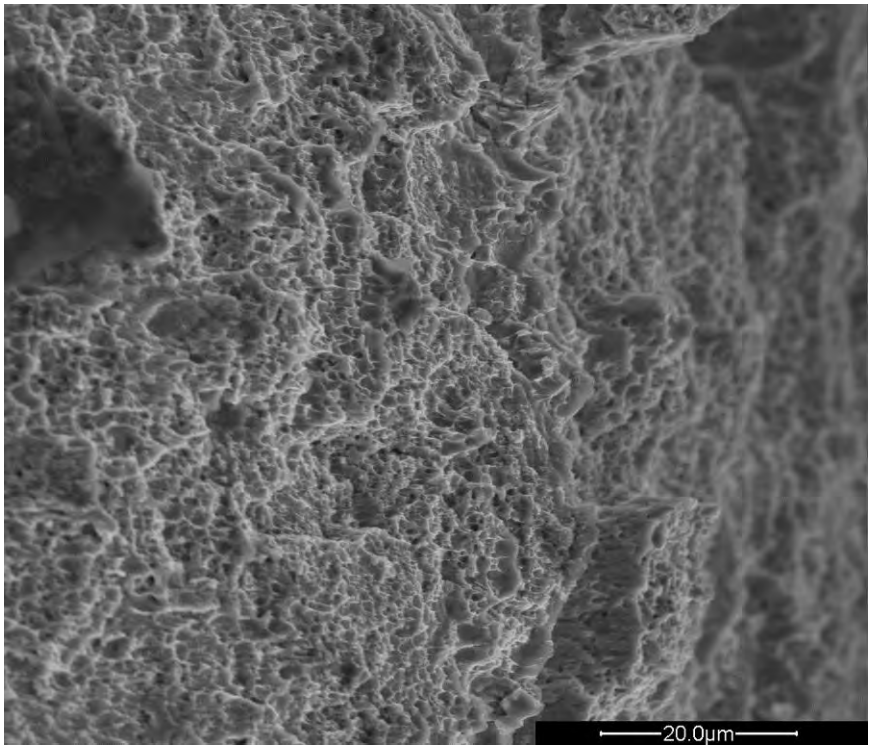

(b)

Figure 4.47 (a) Low and (b) high magnification SEM fractographs of a cold headed pre-drawn 4140 sample. Vertical longitudinal surface relief bands parallel to the crack can be seen in (a). Area boxed in (a) is magnified in (b). Axis of loading is vertical.

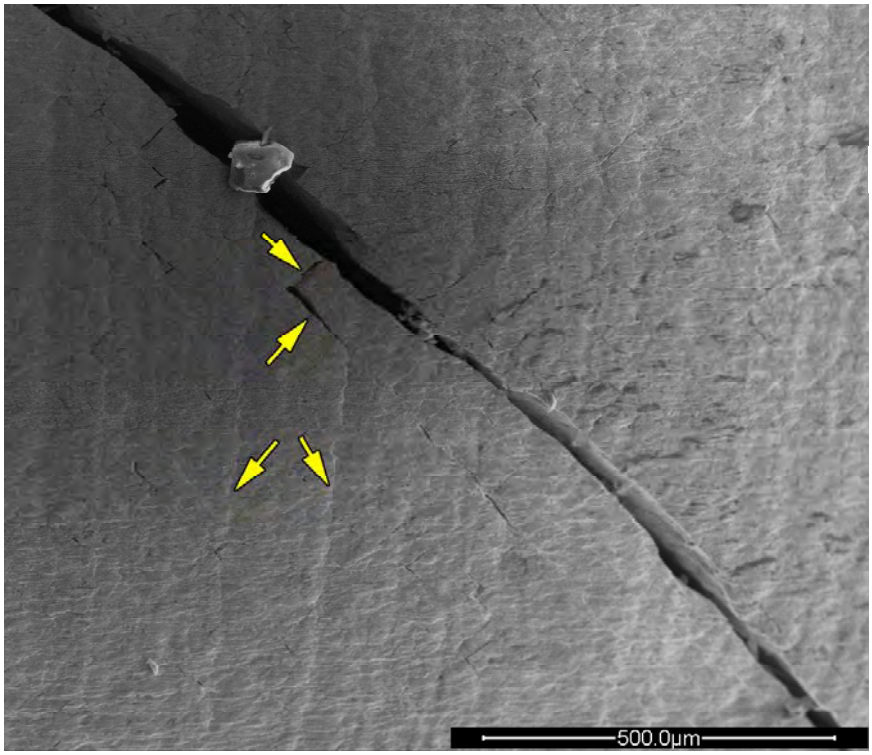

Figure 4.48 SEM fractograph of a cold headed hot-rolled 4140 sample. Longitudinal surface features are highlighted by arrows as well as shear bands. A shear crack propagates diagonally through the image. Axis of loading is vertical.

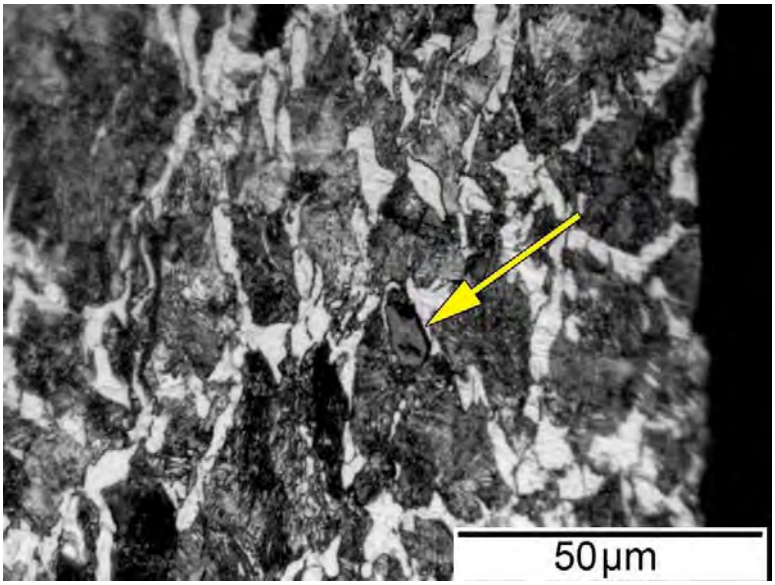

Figure 4.49 Optical micrograph of a normalized 10V45 w/Nb sample illustrating void nucleation at a broken inclusion. The micrograph is taken approximately midway through the cold-headed height near the outer surface. Axis of loading is normal to the cross section.

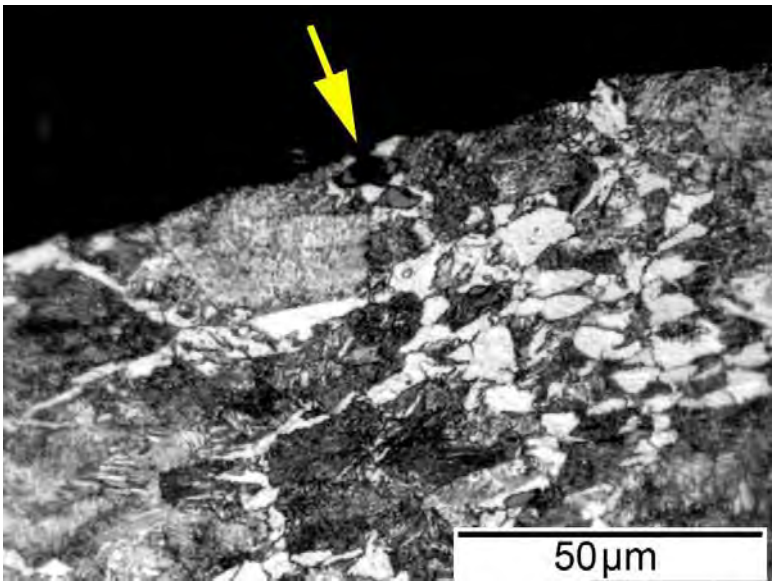

Figure 4.50 Optical micrograph of a normalized and aged 10V45 w/Nb sample illustrating void nucleation at a broken inclusion. The micrograph is taken approximately midway through the cold-headed height at the outer surface. Axis of loading is normal to the cross section.

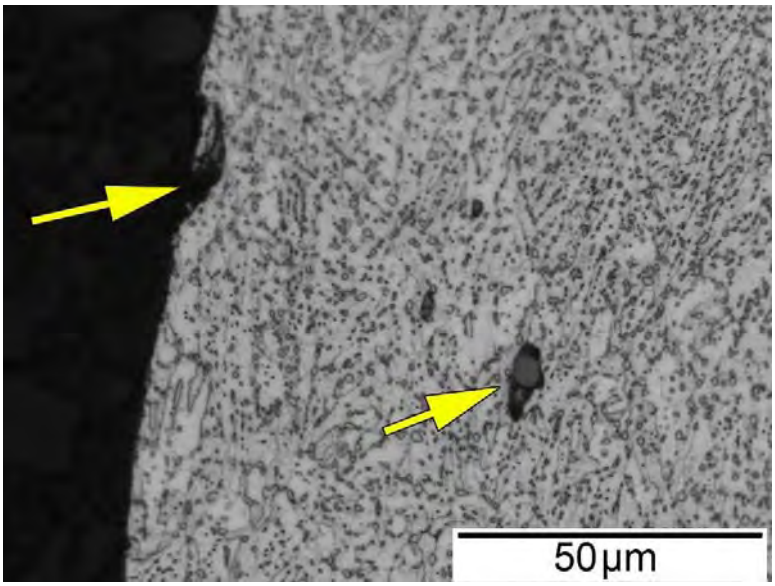

Figure 4.51 Optical micrograph of a spheroidized 10V45 w/Nb sample illustrating initial void nucleation at a probable inclusions site. The micrograph is taken approximately midway through the cold-headed height at the outer surface. Axis of loading is normal to the cross section.

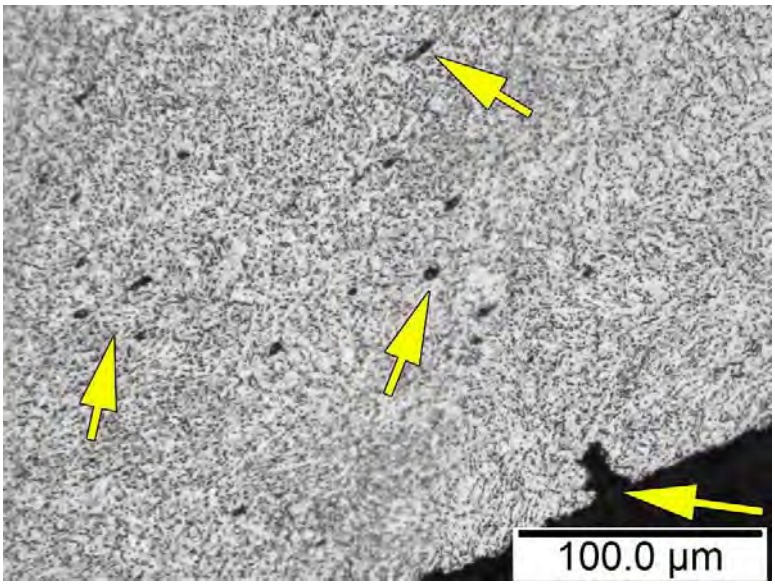

Figure 4.52 Optical micrograph of a spheroidized 10V45 w/Nb sample illustrating void nucleation inclusions and a crack at the surface. These features are indicated by arrows. The micrograph is taken approximately midway through the cold-headed height at the outer surface. Axis of loading is normal to the cross section.

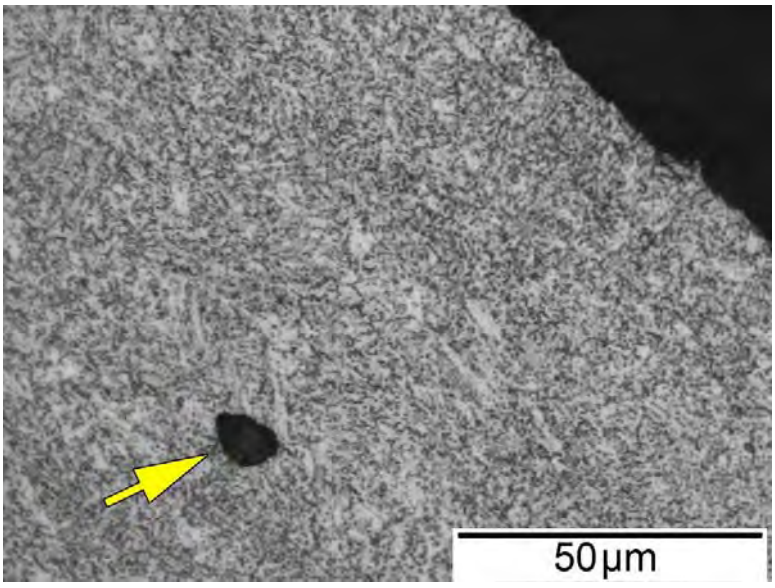

Figure 4.53 Optical micrograph of a quenched and high temperature temper 10V45 w/Nb sample illustrating void nucleation at the area highlighted by the arrow. The micrograph is taken approximately midway through the cold-headed height at the outer surface. Axis of loading is normal to the cross section.

contact with the metal matrix. In addition, voids are more likely to nucleate closer to the surface where the strain is highest. However, the void is far away from the surface suggesting there was likely an inclusion at the site of the void.

Figure 4.54 contains two micrographs from an as-received 10V45 w/Nb sample. In Figure 4.54 (a), a crack is located by the surface at an inclusion surrounded by idiomorphic ferrite. The crack enters the sample with a 45° angle but changes its path near the inclusion. This is an example of void nucleation. However, in Figure 4.54 (b) of the same sample, a greater extent of cracking is observed. Similarly with Figure 4.54 (a), the crack enters with an angle but then propagates to inclusions sites. A small void nucleating at an inclusion that does not link with the crack can be seen in Figure 4.54 (b). Another example can be seen in Figure 4.55 of a normalized and over-aged 10V45 w/Nb sample (macrographs available in Figure 4.35 (e) and (f)). The crack also enters at a 45° angle but then changes its path. Crack opening at a 45° is not always the case as shown in Figure 4.56 of a quenched and high temperature temper sample. In this instance, the crack propagates to link up two voids nucleated at two inclusions near the surface. A large crack can be seen in Figure 4.57 in a 1045 Al TMP sample. The crack enters the sample at a 45° angle but propagates perpendicular to the surface independent of microstructural features. Large cracks that propagate far from the surface into the samples were not helpful in understanding the void nucleation characteristics.

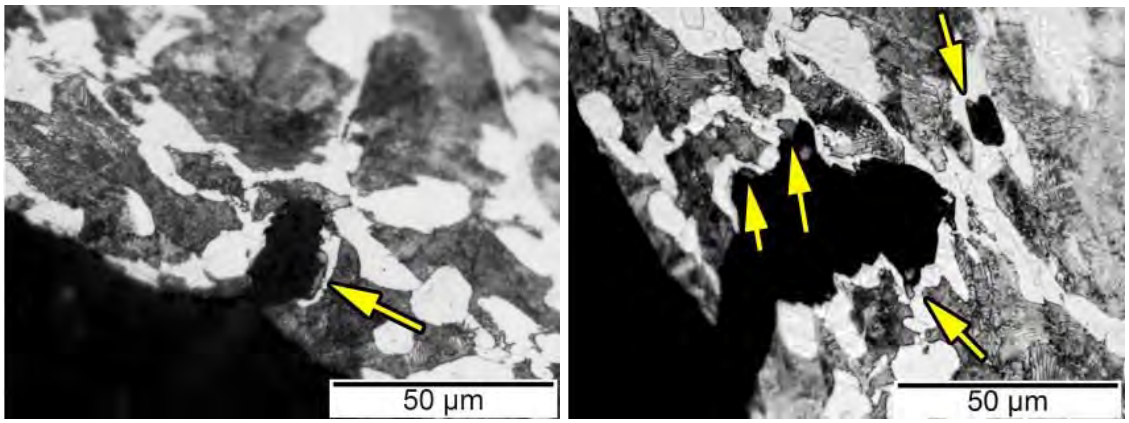

(a) (b)

Figure 4.54 (a), (b) Optical micrographs of as-received 10V45 w/Nb sample illustrating void nucleation at inclusions sites. Micrographs are taken approximately midway through the cold-headed height at the outer surface. Axis of loading is normal to the cross section.

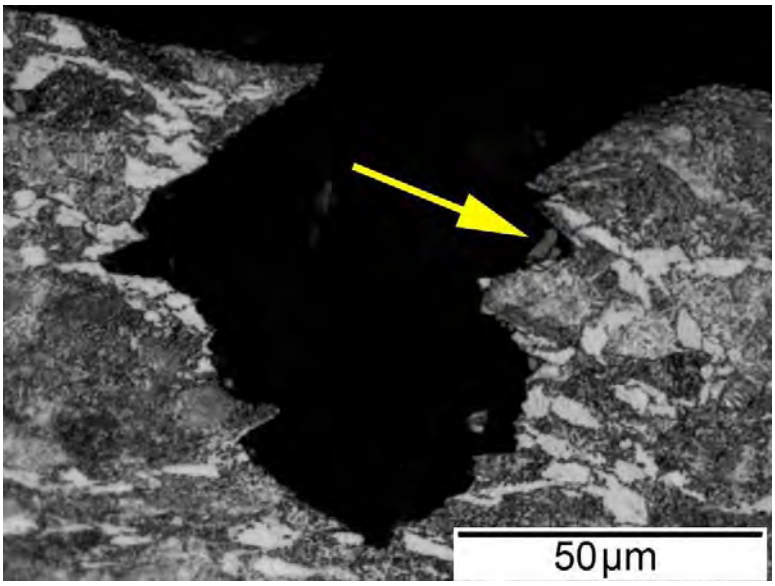

Figure 4.55 Optical micrograph of an over-aged 10V45 w/Nb sample illustrating initial void nucleation and a probable trace of an inclusion. The micrograph is taken approximately midway through the cold-headed height at the outer surface. Axis of loading is normal to the cross section.

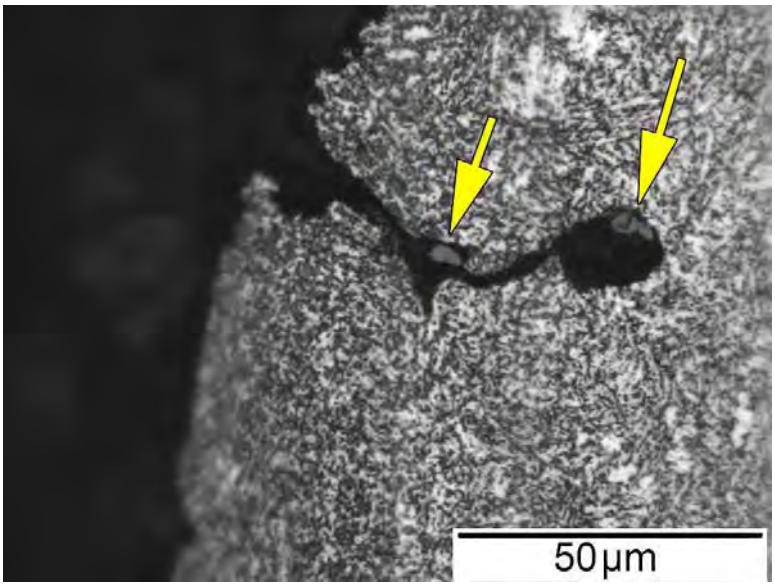

Figure 4.56 Optical micrograph of a quenched and high temperature temper 10V45 w/Nb sample illustrating initial void nucleation and preferential crack propagation to inclusion sites. The micrograph is taken approximately midway through the cold-headed height at the outer surface. Axis of loading is normal to the cross section.

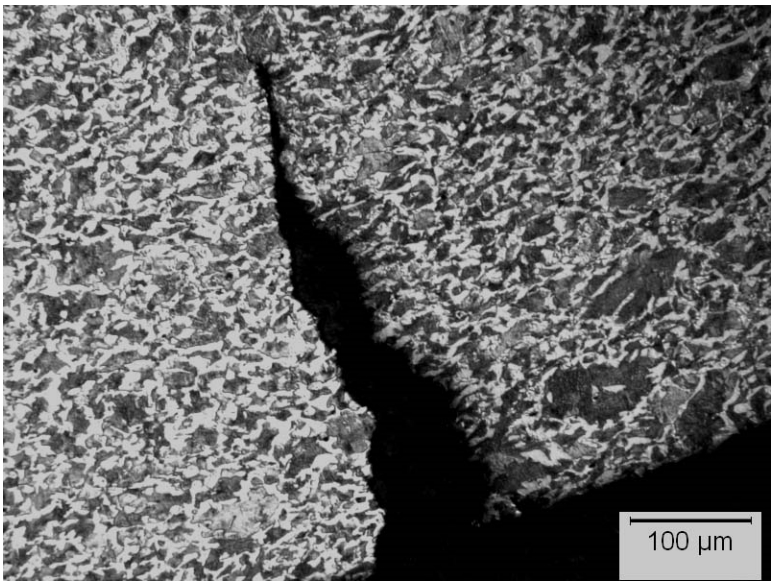

Figure 4.57 Optical micrograph of a 1045 Al TMP showing a large crack. The micrograph is taken approximately midway through the cold-headed height at the outer surface. Axis of loading is normal to the cross section.

4.2 Inclusion Analysis

Inclusion analyses were carried out for 1045 materials, hot-rolled 4135, control-rolled (CR) 16MnCr5 and 1080V. Samples were sectioned longitudinally parallel to the rolling direction, ground and polished to conduct the analysis. Sulfides shorter than 4 µm were excluded from the reported data due to high noise in the data. Table 4.4 summarizes total length of sulfides, total sulfide area and sulfide area pct. Total sulfide lengths were the summation of sulfide lengths with respect to the rolling direction. Total sulfide areas were the total area of scanned sulfides that were used for the calculation of total length. Sulfide area pct is the area occupied by scanned sulfides with respect to the total scanned area. The 10V45 w/Nb material has the highest sulfide area pct at 0.118. The remaining 1045 materials range from 0.066 to 0.084. These values are high compared with the rest of the materials. Note the sulfide area is the same for 1045 Al TMP and 10V45 materials (0.066 sulfide area pct) despite the sulfide length being different for the two materials (18,928 and 23,593 µm for 1045 Al TMP and 10V45, respectively). The hot-rolled 4135 has the lowest sulfide content out of all materials examined. The sulfide area pct is 0.005. The inclusion contents in the alloy steel were less than all 1045 materials. The CR 16MnCr5 material has 0.033 sulfide area pct which is significantly less than the sulfide inclusion content of the 1045 materials. The inclusion content of 1080V is the second lowest after the hot-rolled 4135. The sulfide area pct is at 0.006 which is slightly higher that than of the hot-rolled 4135 material at 0.005.

Figure C.1 contains two sulfide length distribution charts for the 10V45 w/Nb and hot-rolled 4135. Charts for the remaining materials are listed in APPENDIX C. For all the materials, the pattern is

that there was a greater number of shorter sulfides and fewer sulfides of high lengths. Contrasting the 1045 series charts in Figure C.1 to Figure C.3 with hot-rolled 4135 in Figure C.4 and 1080V in Figure C.5 (b) shows the significantly higher inclusion content in 1045 materials.

Table 4.4 – Inclusion Analysis Data

Material	Wt Pct Sulfur	Total Sulfide Length (μm)	Total Sulfide Area (μm^2)	Sulfide Area Pct
1045 Al	0.025	26,302	37,049	0.074
1045 Al TMP	0.025	18,928	33,090	0.066
10V45	0.027	23,593	33,184	0.066
10V45 TMP	0.029	25,209	41,947	0.084
10V45 w/Nb	0.030	22,895	35,330	0.070
10V45 w/Nb TMP	0.030	36,886	58,782	0.118
Hot-rolled 4135	0.0086	1,614	2,587	0.005
CR 16MnCr5	0.025	11,080	16,845	0.033
1080V	0.007	2,117	2,908	0.006

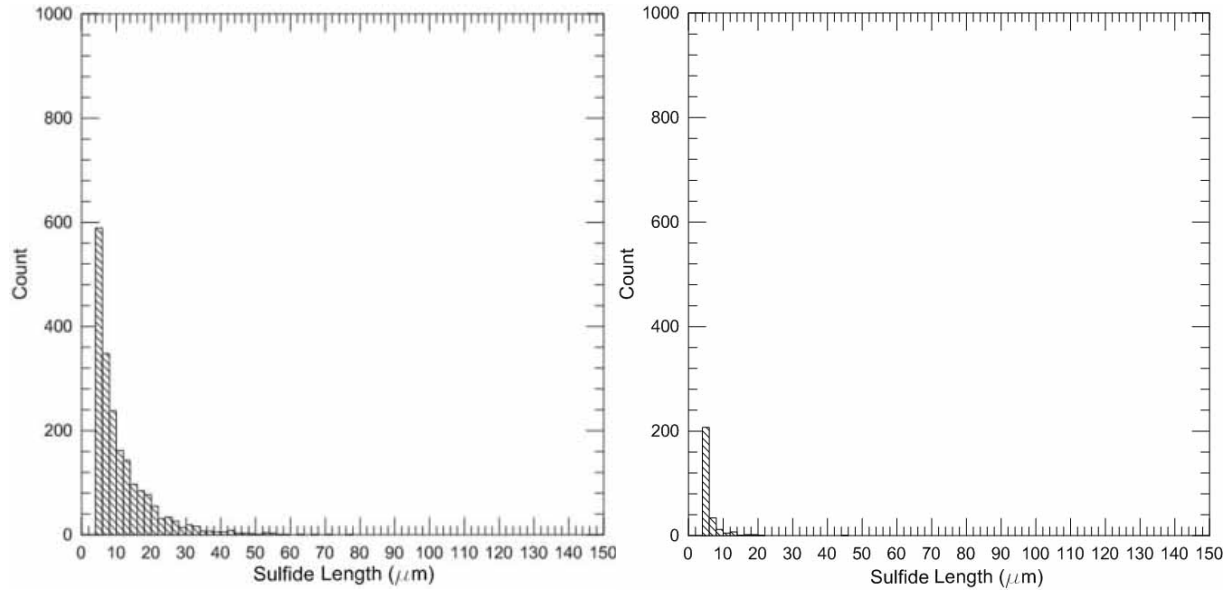

(a) (b)

Figure 4.58 Sulfide length distribution charts for a) 10V45 w/Nb b) hot-rolled 4135.

CHAPTER 5 : DISCUSSION OF EXPERIMENTAL RESULTS

5.1 Introduction

This chapter discusses key results in Chapter 4 and provides additional analysis and interpretation of the results. The objective of this project was to evaluate the cold heading response of alternative microstructures not traditionally used that could improve the economy of the process by eliminating or optimizing certain processing steps. The cold heading response is evaluated in terms of these factors.

5.2 Developed Test Procedure

The developed test procedure provided a means for evaluating and comparing cold headability of steel. The loading conditions were similar to commercial processes. In the developed procedure, a compressive force was applied to a supported cylindrical sample resulting in metal flow and forming a head. A similar flow curve to that seen in the commercial process is observed in the developed procedure (i.e. the shape of the stress-strain curve). Additionally, the load-displacement behavior proved to be reproducible for duplicate sample sets tested. Thus, it was concluded that differences in limit strains and cracking behavior reflected the alloying and process-dependent microstructures.

For the laboratory test, the friction conditions and the imposed strain rate were different from commercial processes in which strain rates exceeding 100 s^{-1} are typically achievable [18]. However, the fracture mode was ductile for all materials tested and for all observed cracks consistent with failure in typical heading operations [28]. With respect to friction conditions, barreling of the upset length was observed in samples tested using the devised testing procedure which indicated a high friction condition. This is shown in the sectioned and macro-etched samples in Figure 4.40. The degree of barreling was proportional to the amount of imposed strain as can be seen when comparing the two samples in Figure 4.40 (a) and (b). Barreling results in secondary tensile stresses at the surface that can nucleate longitudinal cracks [27]. Longitudinal cracks were most often the critical factor in the determiniation of fracture limits in all materials with the exception of hot-rolled 4140. However, a distinct strain path was followed for all the various materials tested in this work and the observance of cracks (i.e. reaching the fracture limit) allowed for comparison of various materials.

5.3 Characterization of As-received Materials

The light optical micrographs of the as-received 1045 materials (Figure 4.3) highlighted the differences in microstrctures between the differently alloyed and processed materials. Mechanical properties were evaluated and related to the microstructure in light of Vickers hardness and yield stress values for each material. All as-received 1045 microstructures consist of proeutectoid ferrite and pearlite.

Table 5.1 summarizes proeutectoid volume fraction, yield stresses and Vickers hardness values for as-received 1045 materials. Differences between these materials are in the proeutectoid ferrite volume fraction, morphology and grain size. With respect to the 1045 Al materials, the use of a lower finish-rolling temperature in the case of the thermomechanically processed (791 °C) than the hot-rolled material (997 °C) resulted in reduction of grain size as can be seen from comparing the micrographs of the two materials (Figure 4.3 (a) and (b)). The grain size reduction was due to the restricted prior-austenite grain growth in the case of the thermomechanically-processed material. The equiaxed morphology is indicative of a recrystallized prior-austenite microstructure after deformation. Vickers hardness values for 1045 Al and 1045 Al TMP are 218 and 196, respectively. The decrease of hardness is most likely attributed to the increased proeutectoid ferrite volume fraction. Yield stresses for the two materials are very close at 495 and 503 MPa for 1045 Al and 1045 Al TMP, respectively. The fact that yield stress values are comparable despite the larger fraction of proeutectoid ferrite was interpreted to be due to the finer grain size in the thermomechanically-processed material.

The 10V45 materials (Figure 4.3 (c) and (d)) exhibited equiaxed morphologies in the hot-rolled material (finish-rolling temperature is 1008 °C) compared with an elongated morphology along the direction of rolling in the thermomechanically-processed material (finish-rolling temperature is 796 °C). Due the lower deformation temperture in the thermomechanically-processed material and possibly the vanadium microalloying additions [13], recrystallization of the prior austenite grains was supressed. Proeutectoid ferrite nucleated at the prior-austenite grain boundaries and pearlite formed as the steel cooled to below the A_1 temperature. The high deformation temperature in the hot-rolled material allowed recrystallization of the prior austenite grains resulting in equiaxed prior-austenite grains morphology. On cooling, proeutectoid ferrite then formed at the prior-austenite grain boundaries and pearlite formation. Vickers hardness values for the 10V45 and 10V45 TMP were 255 and 259, respectively. The similar hardness values are probably due to the similar ferrite volume fractions for the two materials (35 vol pct in 10V45 and 43 vol pct in 10V45 TMP). Yield stresses for 10V45 and 10V45 TMP were 641 and 695 MPa, respectively. The differences in yield stresses between the two materials were most likely associated with vanadium strengthening effects.

With respect to the 10V45 w/Nb materials, similar microstructures to those of the 10V45 materials can be seen in Figure 4.3 (e) and (f). The main difference is in the fraction of proeutectoid ferrite that is around 43 vol pct in 10V45 TMP compared to 60 vol pct in 10V45 w/Nb TMP. Vickers hardness values for the 10V45 w/Nb and 10V45 w/Nb TMP were 275 and 247, respectively. The lower hardness in the TMP steels suggests that the strength is controlled by the significantly larger proeutectoid ferrite volume fraction in 10V45 w/Nb TMP than in 10V45 w/Nb. Yield stresses for the two materials are 673 and 667 MPa, respectively.

Table 5.1 – Summary of Volume Fraction Data, Vickers Hardness and Yield Stresses for 1045 Materials

Material	Proeutectoid Ferrite (vol pct)	Yield Stress (MPa)	Vickers Hardness
1045 Al	34	495	218
1045 Al- TMP	50	503	196
10V45	35	641	255
10V45-TMP	43	695	259
10V45 w/Nb	35	673	275
10V45 w/Nb TMP	60	667	247

Microstructures of 41XX materials were presented in Figure 4.4 through Figure 4.6. The microstructure of hot-rolled and pre-drawn 4135 was comprised of proeutectoid ferrite, acicular ferrite and bainite and the microstructural features were elongated in the direction of drawing in the pre-drawn material. The microstructure of the hot-rolled and pre-drawn 4140 materials was comprised of acicular ferrite and bainite. However, the amount of acicular ferrite was much less than in the 4135 materials and the amount of bainite is greater. The differences in microstructures between 4135 and 4140 are attributed to the different chemical composition and cooling rates. Microstructural features were also elongated in pre-drawn 4140 material similar to the pre-drawn 4135 material. The microstructure of the hot-rolled and pre-drawn PL41 materials consisted of small volume fractions proeutectoid ferrite and pearlite, which reflected the decreased hardenability of PL41 as it lacked molybdenum compared with 4135 and 4140 materials. The effect of pre-drawing on the microstructure was quite evident as easily notable elongated features can be seen in the pre-drawn microstructure when compared with the hot-rolled material.

5.4 Characterization of Heat-treated Materials

Light optical microscopy on the heat-treated 10V45 w/Nb samples confirmed the microstructures that resulted from the devised heat treatment schedules. Similar to the evaluation done for the as-received materials, Vickers hardness and yield stress values are used as indicators of strength. For the spheroidized sample (seen in Figure 4.9), the sample set was heated to 1000 °C for an hour, water quenched, heated to 700 °C for 48 hours and air cooled. The microstructure exhibited a uniformly spheroidized structure. Multiple elongated inclusions in the rolling direction were observed. Vickers hardness for the spheroidized sample was 194 which was the lowest among all the heat-treated materials and what would be expected from the spheroidized microstructure. Yield stress is also the lowest for all heat-treated materials at 599 MPa.

Figure 4.10 contains optical micrographs for the normalized, normalized and aged, and normalized and over-aged 10V45 w/Nb samples. The three sample sets were normalized by austenitizing at a 1000 °C for an hour followed by air cooling. The aged sample set was aged at 625 °C for an hour and air-cooled. The over-aged sample set was aged at 675 °C for an hour and cooled. The three microstructures were ferritic-pearlitic and were quite similar as no microstructural changes would be observable on this scale [13]. The grain size is smaller for all three materials than the as-received 10V45 w/Nb material (Figure 4.3 (e)). Vickers hardness values for the normalized, normalized and aged, and normalized and over-aged materials were 292, 292 and 262 MPa, respectively. Yield stress values for the normalized, normalized and aged, and normalized and over-aged were 832, 838 and 726 MPa, respectively. This meant that the aging treatment for the normalized and aged (austenitizing at a 1000 °C for an hour, air cooling, heating to 625 °C for an hour and air cooling) materials was ineffective in increasing strength beyond the level to which the normalizing treatment (austenitizing at a 1000 °C for an hour and air cooling) had achieved. The unchanged strength level meant that vanadium precipitation had taken place and consequent coarsening of vanadium precipitates took place, thereby, decreasing strength. The normalized and over-aged sample (austenitized at a 1000 °C for an hour, air cooled, heated to 675 °C for an hour and air cooled) resulted in a decrease in strength and hardness from the level of the normalized sample. This means that vanadium precipitates formed in the normalizing treatment coarsened, thereby, decreasing hardness and yield stress due to the high aging temperature.

The microstructures of the austenitized and isothermally-transformed samples at intermediate temperatures are shown in Figure 4.11 and Figure 4.12. The two treatments were meant to produce two distinct bainitic microstructures (upper and lower) with a hardness difference. The two sample sets were austenitized at 866 °C and then rapidly cooled to 435 °C (the high isothermal hold sample set) or 365 °C (the low isothermal hold sample set). The high temperature isothermal hold treatment resulted in a mixture of proeutectoid ferrite, pearlite and bainite. This product meant that the cooling rate intended was not achieved by the heat-treatment performed. The low temperature isothermal hold resulted in a completely bainitic microstructure. Both microstructures had elongated inclusions. Despite the presence of proeutectoid ferrite and pearlite in the high-temperature isothermal hold sample set, a Vickers hardness difference of 19 (Vickers hardness values are summarized in Table 4.3) , which was approximately the target hardness difference, was achieved.

Optical micrographs for the microstructures of the quenched and tempered samples examined are shown in Figure 4.13 and Figure 4.14. The two microstructures were found to be heavily tempered martensitic matrices. The microstructures were quite similar to each other in the optical micrographs and were typical of quenched and tempered medium carbon steels. Elongated inclusions were present in both microstructures. Design of heat-treatment schedules for the two sample sets was done in order to match

the hardness for the two isothermally-transformed sample sets. The heat-treatment schedules involved heating the samples to 870 °C for 10 minutes, water quenching, heating one sample set to 615 °C (the high temperature temper) or 590 °C (the low temperature temper). The high temperature temper sample had a Vickers hardness of 304 which was successfully achieved to match the high temperature isothermal hold sample Vickers hardness value of 303. The low temperature temper sample had a Vickers hardness value of 320 which was successfully achieved to match the low temperature isothermal hold sample Vickers hardness value of 322.

Despite the similar hardness values for the isothermally held samples and quenched and tempered samples, the quenched and tempered samples had significantly higher yields stresses. The high isothermal hold sample and the high temperature temper conditions had yield stresses of 885 and 1013 MPa despite having very close hardness values. This was also the case for the low isothermal hold sample and low temperature temper sample which had yield stress of 905 and 1016 MPa, respectively, despite having very close hardness values. However, the materials had comparable flow stresses at higher stresses as the isothermally-transformed samples had greater capacities for strain hardening and match up to the quenched and tempered samples.

5.5 Effects of Deformation Speed Variation for As-received 1045 Materials

Tests were conducted on as-received 1045 materials using three displacement speeds according to the procedure described in Chapter 3 in order to investigate the potential of strain rate variation in enhancing cold headability. The speeds used were 0.15 mm/s, 1.5 mm/s and 15 mm/s. APPENDIX B contains tables summarizing crack response in terms of crack severity for samples tested at the three deformation speeds to various imposed strains. By contrasting load-displacement behavior in Figure 4.15 for three 10V45 w/Nb samples tested at the three deformation speeds, it can be concluded that a higher deformation speed lead to an increase in the load required for further deformation of the sample at low strains. However, at high strains, flow softening took place due to the increased temperature during deformation. The greater the deformation speed, the greater the temperature increase and the load required to further deform the sample was decreased. If the temperature increase during deformation were greater than the A_1 temperature in certain zones, transformation to martensite would occur in these heated zones and upon subsequent rapid cooling, austenite transforms to martensite. Upon further forming steps, martensite zones act as discontinuities in the microstructure and stress risers facilitating fracture [9]. No evidence of such transformation was seen from the metallography done on cold headed samples meaning that the imposed deformation speed was not high enough to cause a temperature increase during impact capable of inducing such a transformation.

The 1045 Al materials exhibited cracking behavior which depended on deformation speed. This is readily apparent by comparing crack severity for samples tested to the same strain at different deformation speeds in Table B.1 and Table B.2. Samples tested at high deformation speeds exhibited cracks with greater severity than samples tested at a slower deformation speeds. The microalloyed 1045 materials (Table B.3 through Table B.6) did not exhibit a dependence of cracking behavior on deformation speed as samples tested to the same strain exhibited similar crack severity patterns independent of deformation speed. The independence of crack severity on strain rate in the microalloyed 1045 materials limited the potential for strain rate variation for improved cold headability.

5.6 Cold Heading Response of As-received Materials

Testing of as-received materials revealed the superior formabilities of the low sulfur 41XX materials (fracture limits ranging from 1.24 to 1.43 true compressive strain for hot-rolled and pre-drawn materials, with the exception of hot-rolled 4140, and fracture limits greater than 1.94 true compressive strain for spheroidized materials) in comparison to the 1045 materials (fracture limits ranging from 0.63 to 0.85 true compressive strain). The low carbon materials (hot-rolled and control-rolled 16MnCr5) and high carbon material (1080V) had intermediate fracture limits between the fracture limits of the 1045 and 41XX materials (0.95, 0.91 and 0.87 true compressive strain for HR 16MnCr5, CR 16MnCr5 and 1080V, respectively).

With respect to as-received 1045 and 41XX materials, cracks at strains slightly higher than the fracture limit strain were longitudinal for all materials. The hot-rolled 4140 material was the only exception as the material exhibited an unusual tendency for shear cracking. The longitudinal cracks may be explained by the secondary tensile stresses that resulted from the high friction conditions and barreling of the equatorial surface of tested samples. However, the longitudinal cracks occurred at much lower strains for as-received 1045 materials compared with 41XX materials as indicated by the fracture limits. This could mean that the tensile stresses at the free surface resulting from friction and barreling of the samples were more effective at initiating void nucleation in 1045 materials than in 41XX materials. Fractography and metallography on cold headed samples were carried out in order to better understand the reason for the different formabilities as indicated by the fracture limits.

Fractography on all as-received materials confirmed a ductile mode of fracture through void nucleation, growth and coalescence for all materials tested. Metallography was carried out near the surface of cold headed as-received 1045 samples was used to evaluate the potential reasons for void nucleation and onset of fracture occurring at lower strains for 1045 materials than 41XX materials. A pattern of void nucleation at inclusions was observed in as-received 1045 materials. Often, cracks were observed to propagate preferentially through idiomorphic ferrite through broken inclusions (examples are

shown in Figure 4.54). Since all 1045 and 41XX materials contained more than 0.72 wt pct Mn, the steels were likely to contain a high inclusion concentration in the presence of a sufficient amount of sulfur forming MnS inclusions. The reported chemical composition and the inclusion analysis results highlighted the greater sulfide inclusion contents in 1045 materials in comparison with the hot-rolled 4135 material.

Due to the strong correlation between sulfide inclusion content and the mechanism of fracture in 1045 materials, fracture limits for as-received materials were plotted as a function of sulfur weight percent (Figure 5.1). Families of materials lied closely together occupying different areas of the plot. The spheroidized 41XX materials had the best cold headability out of all as-received materials as fracture could not be induced by the maximum load of the MTS frame at 444.8 kN (100 kips) for any of these materials (fracture limits greater than 1.94 true compressive strain). This confirms the superiority of spheroidized microstructures for cold heading applications over alternative microstructures. The pre-drawn materials had the best formabilities after the spheroidized materials (fracture limits ranging from 1.24 to 1.43 true compressive strain). Pre-drawing enhances cold headability increasing the fracture limits from 1.24 to 1.43 true compressive strain for 4135 materials and from 0.86 to 1.24 true compressive strain for 4140 materials. The improvement in cold headability of 4140 is significant as pre-drawing eliminated the tendency of 4140 towards shear cracking and longitudinal cracks were observed at strains slightly higher than the fracture limit. Pre-drawing was ineffective at improving cold headability of PL41 material as the fracture limit decreased from 1.35 to 1.24 true compressive strain upon the application of drawing prior to cold heading.

Testing of 1080V illustrated that a high carbon material is capable of undergoing approximately the same amount of deformation as low and medium carbon steels with high sulfur contents provided the sulfur content is as low as 0.007 wt pct. Fracture limits for low carbon materials were 0.95 and 0.91 true compressive strain for hot-rolled and control-rolled 16MnCr5, respectively, and 0.87 true compressive strain for 1080V. The sulfur content in low carbon materials is 0.025 which is the same as the sulfur level in the 1045 Al materials. The 16MnCr5 and as-received1045 materials occupy the bottom right of the plot is Figure 5.1 as they contain high sulfur and the lowest fracture limits out of all the different families of materials. Figure 5.2 is a plot of fracture limit as a function of total sulfide length for materials included in the inclusion analysis. A trend of inverse proportionality between total sulfide lengths and fracture limits can be seen in the plot despite some scatter in the data with respect to 1045 materials. The scatter may be due to the associated uncertainty in total sulfide length measurement with the method of light optical microscopy detection where measurements are sensitive to sample preparation.

Figure 5.3 is a plot of fracture limits of as-received materials as a function of Vickers hardness. For the data points of 41XX materials and the 1080V material, an increase in hardness correlated to a

decrease in fracture limits. These materials exhibited the predicted relationship between hardness and fracture limits schematically illustrated in Figure 3.3. However, the 1045 materials and the 16MnCr5 materials did not fit this trend as they have lower fracture limits than 41XX materials with approximately the same hardness. The lower fracture limits of 1045 and 16MnCr5 are interpreted to be the result of the higher inclusion contents of these steels.

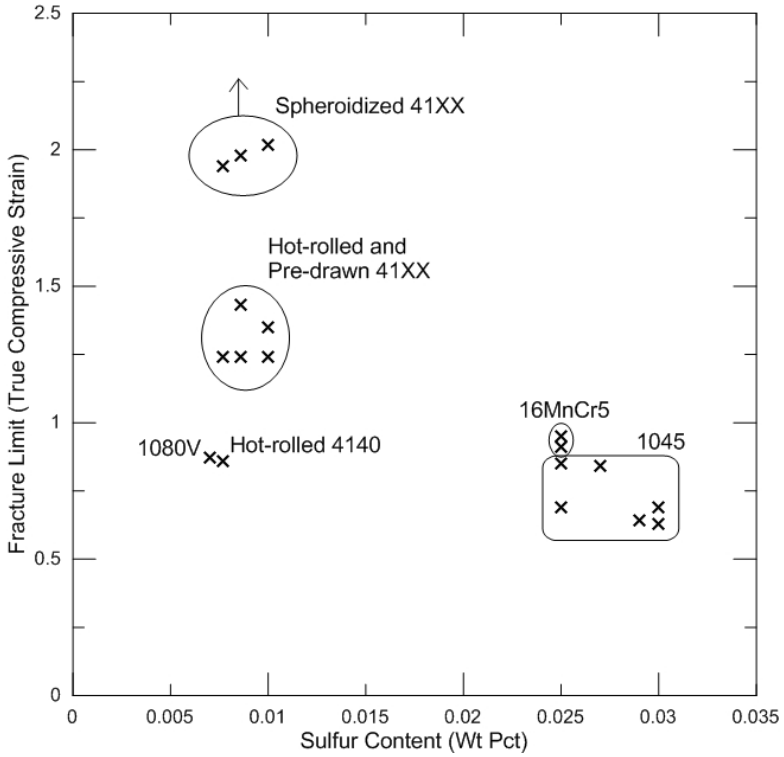

Figure 5.1 Fracture limit as a function of sulfur content for as-received materials. Fracture limits of spheroidized 41XX materials are greater than the data points in the plot.

5.1 Cold Heading Response of Heat-treated Materials

Fracture limits could not be defined for heat-treated 10V45 w/Nb materials even at strains less than the fracture limit for the as-received material (0.69 true compressive strain). The reason for the incipient longitudinal cracks at lower strains than the fracture limit of the as-received materials is not well-understood and requires further investigation. As all the heat-treated samples were machined from the same base materials prior to heat-treatment and with the same surface finish, inclusion content may be ruled out as a reason for the variation in cold heading response and these variations in fracture responses, when present, were entirely due to microstructural differences.

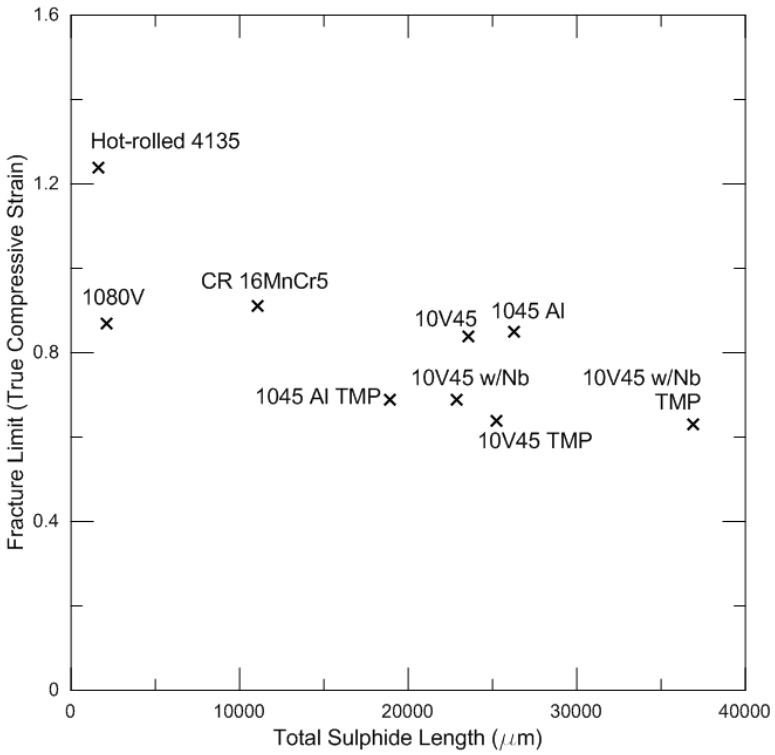

Figure 5.2 Fracture limit as a function of total sulfide length for as-received materials used in the inclusion analysis.

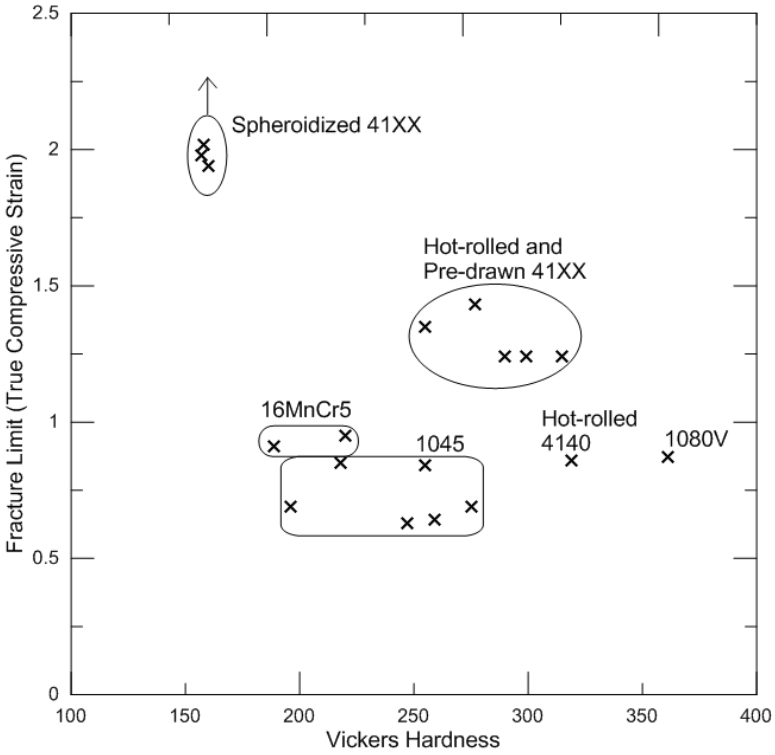

Figure 5.3 Fracture limit as a function of Vickers hardness for as-received materials.

The spheroidized 10V45 w/Nb exhibited the thinnest longitudinal cracks on the free surface than all the other heat-treated materials as seen in Figure 4.32. However, the material contained incipient cracks at a strain as low as 0.57 true compressive strains and easily detectable cracks at higher strains (Figure 4.32) unlike the spheroidized 41XX steels where absolutely no cracks were observed even at strains as high as 1.94 true compressive strain. Also, strength level is the lowest out of all heat-treated materials. Metallography on cold headed spheroidized 10V45 w/Nb samples revealed the important role of inclusions in void nucleation as evidence for crack nucleation by decohesion or/and breaking of inclusions was observed. The remaining heat treatments were successful in increasing strength of the steels but formabilities were degraded as a consequence as shown in Figure 4.33 through Figure 4.39. This means that spheroidization was successful in enhancing cold headability (compared with the as-received material) despite the high inclusion content of the steel. However, for all the remaining heat-treated materials, the heat-treatments were not successful in enhancing strength while maintaining formability. Evidence of predominant void nucleation at second-phase inclusions was observed in all heat-treated materials.

The crack response, however, of heat-treated 10V45 w/Nb materials exhibited differences which are interpreted to be the result of microstructure. In order to compare the crack response of different heat-treated materials, the medium level strain samples (1.15 true compressive strain) shown in Figure 4.32 through Figure 4.39 (c) and (d) are referenced. A few small cracks can be seen in the spheroidized sample in Figure 4.32 (c) and (d). In the normalized material shown in Figure 4.33 (c) and (d), however, more cracks that are larger were observed. The normalized and aged material in Figure 4.34 (c) and (d) shows large cracks of a mixed longitudinal and shear character. Therefore, the aging treatment resulted in the nucleation and propagation of larger cracks despite the same hardness level (Vickers hardness of 292 for both materials). The normalized and over-aged sample Figure 4.35 (c) and (d)) exhibited a large longitudinal crack also showing the ineffectiveness of aging as an option for an improved cold heading behavior when compared with the normalized sample in Figure 4.33 (c) and (d).

With respect to isothermally-transformed and quenched and tempered 10V45 w/Nb materials, comparing medium strain level samples (1.15 true compressive strain) in the macrographs seen in Figure 4.36 (c) and (d) through Figure 4.39 (c) and (d) highlighted the main differences in crack response. The austenitized and isothermally transformed material at high temperature (435 °C) had approximately the same hardness level as the quenched and tempered material at a high tempering temperature (590 °C) (Vickers hardness of 303 and 304, respectively). The austenitized and isothermally-transformed material at a low temperature (365 °C) had approximately the same hardness level as the quenched and tempered material at a high tempering temperature (615 °C) (Vickers hardness of 322 and 320, respectively). The cracking behavior was different despite the similar hardness levels of these materials. The isothermally-

transformed materials exhibited a tendency towards the formation of densely populated small cracks distributed around the free surface of the sample at a medium strain level (1.15 true compressive strain). In contrast, the quenched and tempered materials exhibit few large cracks at the same strain level. The quenched and tempered material at a low tempering temperature exhibited a crack of a mixed longitudinal and shear character as shown in Figure 4.39 (c) and (d). From the tested samples, the difference in the crack response shows that isothermally-transformed microstructures tend to nucleate many small cracks while quenched and tempered steels nucleate larger and fewer cracks (compared with isothermally-transformed materials) despite the materials being at the same hardness level.

5.2 Surface Features

The differences in surface features for the various materials is interpreted to be the result of the microstructural differences between the materials. The as-received 1045 materials exhibit rough surfaces as shown in Figure 4.16 through Figure 4.19. The equiaxed orange peel for these materials was the result of relatively coarse ferritic-pearlitic microstructures (compared with normalized 10V45 w/Nb materials). The difference in strength between the two microconstituents results in a rough surface as ferrite deformed easier at the surface and pearlite exhibited more resistance towards deformation yielding the rough surfaces shown in the figures.

The 41XX exhibited smoother surfaces than 1045 materials as shown in Figure 4.20 through Figure 4.28. The smoother surfaces are attributed to the finer size of microstructural constituents. Hot-rolled and pre-drawn 4135 and 4140 materials exhibited surfaces with longitudinal surface relief features. These features correlate with the elongated areas of ferrite and bainite along the direction of rolling for these materials. During deformation, ferrite regions deform more easily than bainite regions. Therefore, the surfaces exhibited bands bowing in or out of the surface depending on the strength level of the band. Pre-drawing decreased the density of surface relief bands around the surface of the samples for a given strain level. Spheroidization eliminated the presence of surface bands for 4135 and equiaxed orange peel is observed on the surface but surface bands are still present in spheroidized 4140. The equiaxed orange peel in spheroidized 4135 means that spheroidization treatment was effective in eliminating the strength differences between the different microstructural constituents in the parent microstructure (pre-drawn 4135). In spheroidized 4140, however, the presence of longitudinal surface relief meant that the spheroidized treatment was ineffective in eliminating the strength differences between the microstructural constituents. Despite the microstructure being completely spheroidized, the carbide distribution is likely to be greater in bainitic regions of the parent microstructure, thus, not entirely eliminating the strength differences between the ferrite and bainite regions of the parent microstructure. In the context of cold headability cracks were found to nucleate parallel to the longitudinal surface relief as seen in Figure 4.47

and may cause failure at lower strains than in a sample with equiaxed orange peel. PL41 materials exhibited equiaxed surface relief. The equiaxed surface roughening is attributed to the ferritic-pearlitic microstructures of hot-rolled and pre-drawn PL41 and the spheroidized microstructure in spheroidized PL41.

Surfaces of heat-treated 10V45 w/Nb materials all exhibited equiaxed surface roughening to various extents (Figure 4.32 through Figure 4.39). The normalized, normalized and aged, and normalized and over-aged materials exhibit the roughest surfaces out of all heat-treated materials. However, the surfaces are smoother than as-received 1045 materials. The appearance of smoother surfaces in normalized, normalized and aged and normalized and over-aged are attributed to the finer ferritic-pearlitic microstructure in these heat-treated materials than in as-received materials. The spheroidized material exhibited a surface with surface roughening but not to the extent of the normalized materials. The isothermally-transformed and the quenched and tempered materials had smooth surfaces with minimal surface roughening. The smooth surfaces for these materials are attributed to the more uniform microstructure for these materials in contrast to the normalize, normalized and aged and normalized and over-aged materials.

CHAPTER 6 : CONCLUSIONS

The objective of this project was to evaluate the cold headability of medium carbon steels processed with different microstructures and to determine the relationships between starting microstructures and susceptibility to fracture during cold heading operations. In order to achieve this goal, a family of 1045 materials, 41XX materials, hot-rolled and control-rolled 16MnCr5 steel, a 1080V steel and heat-treated 10V45 w/Nb steels were cold headed according to a test procedure designed for this project. Important conclusions from this work are summarized below.

1. A laboratory cold heading test procedure in which imposed strain, capable of inducing cracks for most test materials, was developed. All the aforementioned materials were tested and fracture limits values were defined for all materials tested with the exception of spheroidized 41XX and heat-treated 10V45 w/Nb materials. In the test procedure, surface finish was not a variable as consistent 16G surface finishes were used for all machined samples. Lubrication was found to cause an unstable deformation mode in the developed test procedure and, therefore, samples were wiped with acetone prior to testing to minimize the presence of oil films and ensure consistent friction conditions.
2. Over the range of displacement rates evaluated (i.e. 0.15 to 15 mm/s), data on 1045 microalloyed materials revealed that the fracture behavior was essentially independent of displacement rate. Thus, the effects of systemic microstructural variations were evaluated at the highest displacement rate.
3. In the experimental materials, three types of cracks were observed. These types are longitudinal, shear or ‘mixed mode’ (i.e. mixed longitudinal and shear character) cracks. However, in all materials, except hot-rolled 4140, fracture limits were defined based on detecting longitudinal cracks at strains slightly greater than the fracture limit. The fracture limit of hot-rolled 4140 was determined based on detecting shear cracks at strains slightly greater the fracture limit.
4. Fracture limits, defined as the maximum strain at which no cracks are observed upon examination under a stereo microscope at 20X, varied according to hardness and sulfur content. Data from low sulfur materials (0.007 to 0.01 wt pct S), 41XX materials and 1080V, showed that an increase in hardness resulted in a decrease in the fracture limit (fracture limits of 0.87 for 1080V and 1.24 true compressive strain or greater for 41XX materials with the exception of hot-rolled 4140). Data from high sulfur materials

(0.025 to 0.030 wt pct S), 1045 materials and 16MnCr5 materials, showed that despite having hardness values comparable to 41XX materials, a high sulfur content resulted in lower fracture limits (fracture limits ranging from 0.63 to 0.95 true compressive strain).

5. Cracking in all materials occurred by ductile rupture with void nucleation enhanced by the presence of sulfide inclusions for as-received 1045 materials and heat-treated 10V45 w/Nb materials.
6. Surface roughening, in the form of uniform "orange peel" and longitudinal surface relief was observed and interpreted to reflect microstructural variations. Specifically, as-received 1045 materials exhibited rough surfaces (orange peel) due to the coarse ferritic-pearlitic microstructures compared with the smoother surfaces (minimal orange peel) of normalized 10V45 w/Nb materials which had fine ferritic-pearlitic microstructures. Isothermally-transformed and quenched and tempered materials exhibited smooth surfaces indicative of fine uniform microstructures. Hot-rolled and pre-drawn 4135 and 4140 exhibited longitudinal surface relief features indicative of directionality and strength difference of microstructural constituents. Cracks were found to nucleate along the surface relief bands. Pre-drawing decreased the density of these bands. Spheroidization is effective in eliminating the strength difference in 4135 material but not in 4140. PL41 material exhibited uniform orange peel for all conditions as it is composed of a ferritic-pearlitic matrix in the hot-rolled and pre-drawn conditions and a uniformly spheroidized matrix in the spheroidized conditions.
7. Specific conclusions were drawn on the effects of microstructure in the various materials groups:
    a. Testing of as-received 1045 was able to define fracture limits ranging from 0.63 to 0.85 true compressive strain. Additions of vanadium and niobium alloying and the use of TMP (i.e. lower finish-rolling temperatures than those used in hot-rolling) resulted in materials with similar fracture limits to hot-rolled products as it was concluded that the sulfide inclusion content, present in all alloys, dominated the microstructural effects leading to ductile fracture nucleation.
    b. Testing of 41XX materials affirmed the superiority of spheroidized microstructures for cold heading applications as fracture limits exceeded 1.94 true compressive strain and definite values could not be defined for spheroidized microstructures due to reaching the MTS frame maximum load capacity of 444.8 kN (100 kips). Pre-drawing after hot rolling and prior to cold heading significantly enhanced the

cold heading performance of 4140 steel by increasing the fracture limit from 0.86 to 1.24 true compressive strain, increased fracture limit for 4135 steel from 1.24 to 1.43 and had a limited effect on the PL41 steel as the fracture limit decreased slightly from 1.35 to 1.24.

c. Testing of low and high carbon materials showed that a high carbon material (1080V, fracture limit is 0.87 true compressive strain) with a low sulfur content (0.007 wt pct) is capable of undergoing approximately the same amount of deformation (indicated by the fracture limits) as low carbon materials (hot-rolled and control-rolled 16MnCr5, fracture limits are 0.95 and 0.91 true compressive strain, respectively) with a high sulfur material (0.025 wt pct).
d. Heat treating of the 10V45 w/Nb materials had limited effects on the cold headability as the material response was interpreted to be due to the effects of sulfide inclusions. The spheroidized condition showed a better cold heading performance than the normalized, the normalized and aged, the normalized and over-aged, the isothermally-transformed, and the quenched and tempered materials.
e. Despite the limiting effect of heat-treatment on cold headability, the heat-treated conditions exhibited different cracking behavior. The spheroidized material exhibited thin longitudinal cracks of increasing density with increasing strain. The normalized material exhibited multiple small cracks (larger than in the spheroidized condition). Aging treatments after normalizing result in multiple large cracks compared with the small cracks in the normalized material at the same level of strain. Isothermally-transformed materials exhibited multiple small longitudinal cracks at medium strains (1.15 true compressive strain) and both small and large longitudinal cracks at high strains (1.52 true compressive strain). In contrast, quenched and tempered materials exhibited large longitudinal cracks at medium strains (1.15 true compressive strain) and both small and large longitudinal crack at high strains (1.52 true compressive strain).

CHAPTER 7 : FUTURE WORK

Continuation of this work could attempt to evaluate cold headability of various steel microstructures processed from the same low sulfur medium carbon steel. Testing of such microstructures could allow for comparison of materials with the similar strength level but high inclusion content steels in this study. Further testing, in other facilities, of spheroidized 41XX to define definite fracture limit values could help better understand and compare spheroidized microstructures with the remaining materials for which fracture limits were defined. An SEM inclusion analysis, in which inclusions are identified and quantified with a high degree of certainty, could enhance the understanding of the role of inclusions in ductile fracture during cold heading.

REFERENCES

[1] T. Padfield, M. Bhupatiraju, ASM Handbook vol 14A, Metal Forming: Bulk Forming, pp. 383, Oct. 2005.

[2] N. Muzak, K. Naidu, C. Osborne, "New Methods for Assessing Cold Heading Quality," Wire Journal International, pp. 66-72, October 1996.

[3] Industrial Fastener Institute, "Cold Formed Parts Yield Impressive Costs Benefits," Manufacturing Engineering, vol. 93, November 1984, pp. 43-48.

[4] A. Benzerga, J. Leblond, "Ductile Fracture by Void Growth and Coalescence," Department of Aerospace Engineering, Texas A&M University, 2012.

[5] A. Jenner, B. Dodd, "Cold Upsetting and Free Surface Ductility," Journal of Mechanical WorkingTechnology, vol. 5, pp. 31-43, 1981.

[6] M. D. Meheshwari, B. Dutta, T. Mukherjee, "Quality Requirements for Cold Heading Grades of Steel," Tool & Alloy Steels, pp. 247-251, 1978.

[7] T. Matsunaga, K. Shiwaku, "Manufacturing of Cold Heading Quality Wire Rods and Wires," SEAISI Quarterly Journal, vol. 9, no. 1, pp. 45-55.

[8] A. F. Turner, C. S. Betteridge, J. Avery, "Development of Steels for the Fastener and Cold Forging Markets by Testing Under Fastener Production Conditions," British Steel Report, Commission of the European Communities, 1984.

[9] N. Nickoletopoulos, "Physical and Numerical Modeling of Steel Wire Rod Fracture during Upsetting for Cold Heading Operations," McGill University, February 2001.

[10] B. Yalamanchili, P. M. Power, J. B. Nelson Jr., "Effect of Residual Elements on Low Carbon Rod Quality and Implications to the End User," Wire Journal International, vol 32, no. 5, pp. 100-106.

[11] A. Ohmori, A. Matsuzaki, K. Amano, "Effect of Cu, Sn and Sb on Cold Forgeability of a 0.5% Carbon Steel," ISIJ International, vol. 37, no. 3, pp. 302-304, 1997.

[12] L. Samuels, Optical Microscopy of Carbon Steels, American Society for Metals, Metals Park, Ohio.

[13] G. Krauss, Steels Processing, Structure, and Performance, ASM International, Materials Park, Ohio, 2004.

[14] R. Kuziak, S. Zajac, R. Kawalla et al., "Cold Heading Quality Low-Carbon Ultra-High-Strength Bainitic Steels (Coheadbain)," European Commission Research Fund for Coal and Steel, 2010.

[15] J. Davis, Cold Heading, ASM Metals Handbook, vol 14, Forming and Forging, 1988.

[16] S.H. Goods, L.M. Brown, "The Nucleation of Cavities by Plastic Deformation," Acta Met., vol 27, 1979, pp. 1-25.

[17] Y. Sarruf, B. Cao, J.J. Jonas, N. Nickoletopoulos, “Criteria and Tests for Cold Headability,” WireAssociation International, Conference Proceedings, 68th Annual Convention, pp. 141-148, 1998.

[18] A. Jenner, B. Dodd, “Cold Upsetting and Free Surface Ductility,” Journal of Mechanical WorkingTechnology, vol. 5, pp. 31-43, 1981.

[19] H. Kudo, K. Asi, “Effect of Compression Test Condition upon Fracturing of a Medium Carbon Steel – Study on Cold Forgeability Test: Part II,” Journal of Japan Society for Technology of Plasticity, vol 8, no. 72, pp. 17-27, 1967.

[20] A, Sabih, J.A. Nemes, “Internal Ductile Failure Mechanisms in Steel Cold Heading Process,” Journal of Materials Processing Technology, vol 209, pp. 4292-4311, 2009.

[21] “High Strain Rate Tension and compression Tests, Mechanical Testing and Evaluation,” vol 8, ASM Handbook, ASM International, 2000, pp. 429-446.

[22] H. C. Rogers, “Adiabatic Shearing – General Nature and Material Aspects, Material Behavior under High Stress and Ultrahigh Loading Rates,” Plenum Press, New York, pp.101-118.

[23] L. Ma, “Effect of Pre-Draw on Formability During Cold Heading,” McGill University, August 2005.

[24] M. Oyane, T. Sato, K. Okimoto, S. Shima, “Criteria for Ductile Fracture and Their applications,” Journal of Mechanical Working Technology, vol 4, p.65-81.

[25] M.G. Cockcroft and D.J. Latham “Ductility and the Workability of Metal,” Journal of the Institute of Metals vol. 96, pp. 33-39, 1968.

[26] G. Dieter, Mechanical Metallurgy, New York, NY: McGraw-Hill, 1986.

[27] S. Semiatin, J. Jones, “Formability and workability of Metals,” ASM, Metals Park, Ohio, 1984.

[28] K. Mukherjee, D. Matlock, “Thermomechanical Processing of Medium Carbon Microalloyed Bar Steels”, 2011 Semi-Annual Progress Report of the Advanced Steel Processing and Products Research Center, MT-SRC-011-009, March 1, 2012, pp 13.1-13.14.

[29] A. Schaneman, “The Effects of Prior Microstructure on Spheroidizing Kinetics and Cold Workability in Bar Steels,” Colorado School of Mines, August 2009.

[30] S. Miller, “Effect of Microalloying on the Strength of High Carbon Wire Steels,” Colorado School of Mines, November 2012.

[31] J. William, D. Callister, Fundamentals of Materials Science and Engineering, USA, John Wiley & Sons, 2nd Ed, pp. 199.

[32] X. Ma, “Effect of Microstructure on The Cold Headability of A Medium Carbon Steel,” McGill University, 2003.

APPENDIX A: CALCULATIONS FOR SAMPLE DIMENSIONS

A sample diameter which would accommodate sufficient strain without exceeding the force capacity of the available equipment was identified by predicting force-displacement curves for material with assumed strength and strain hardening properties. The analysis was based on the geometry shown schematically in Figure A.1, and initially calculations were based on a frictionless condition for materials assumed to exhibit flow curves described by the Hollomon equation

$$\sigma = K\varepsilon^n \qquad \text{Eq. A.1}$$

where σ is true stress, *K* is the strength index, ε is true strain and n is the strain hardening exponent. By employing the constant volume assumption,

$$\pi\left(\frac{d_1}{2}\right)^2 h_1 = \pi\left(\frac{d_2}{2}\right)^2 h_2 \qquad \text{Eq. A.2}$$

$$d_2 = d_1\sqrt{\frac{h_1}{h_2}} \qquad \text{Eq. A.3}$$

Since the instantaneous contact area, A_{ins}, is $\pi\left(\frac{d_2}{2}\right)^2$ and $h_2 = h_1 - \delta$, an expression for instantaneous are then becomes

$$A_{ins} = \frac{\pi d_1^2 h_1}{4\left(h_1 - \delta\right)} \qquad \text{Eq. A.4}$$

Substituting in the expression $\sigma = \frac{P}{A_{ins}}$ and solving for load gives

$$P = \frac{\sigma \pi d_1^2 h_1}{4(h_1 - \delta)} \qquad \text{Eq. A.5}$$

By invoking Eq A.1, an expression for load then becomes

$$P = \frac{K\left[\ln\left(1 - \frac{\delta}{h_1}\right)\right]^n \pi d_1^2 h_1}{4(h_1 - \delta)} \qquad \text{Eq. A.6}$$

Eq. A.6 enables the calculation of load-displacement curves as a function of displacement and material property constants. Two hypothetical low and high carbon steels were selected to predict the curves. The low carbon steel has an n=0.21 and a K=600 MPa and the high carbon has an n=0.12 and a K=2650 MPa [29]. Calculations were done using the previously determined h/d ratio of 2. Curves were plotted to 80% reduction in height or up to the machine limit. These curves are shown in Figure A.2.

For low carbon steel, diameters up to 8 mm can be compressed to 80% reduction in height without exceeding the machine capacity. However, there is a concern with regard to high carbon steel samples, 80% reduction in height can only be achieved if a diameter of 6 mm is used. Therefore, it was decided that a consistent 6-mm-diameter samples would be used for all the tests to allow for sufficient measurable deformation before failure or reaching the machine limit. Selection of the 6 mm as the diameter also enabled expanding the study to include a high carbon steel which was not the in the initial materials matrix. This also meant that a sample height of 12 mm would be used. Corresponding for h/d ratio of 2, the height of the deformed sample was selected as 12 mm.

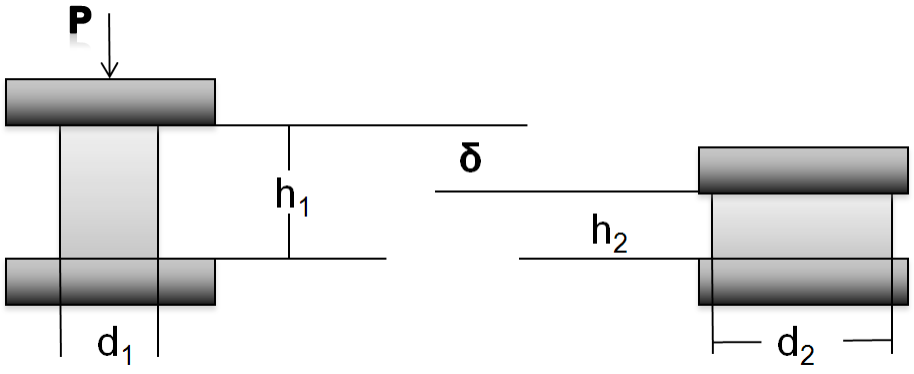

Figure A.1 Schematic illustration of a frictionless upsetting process.

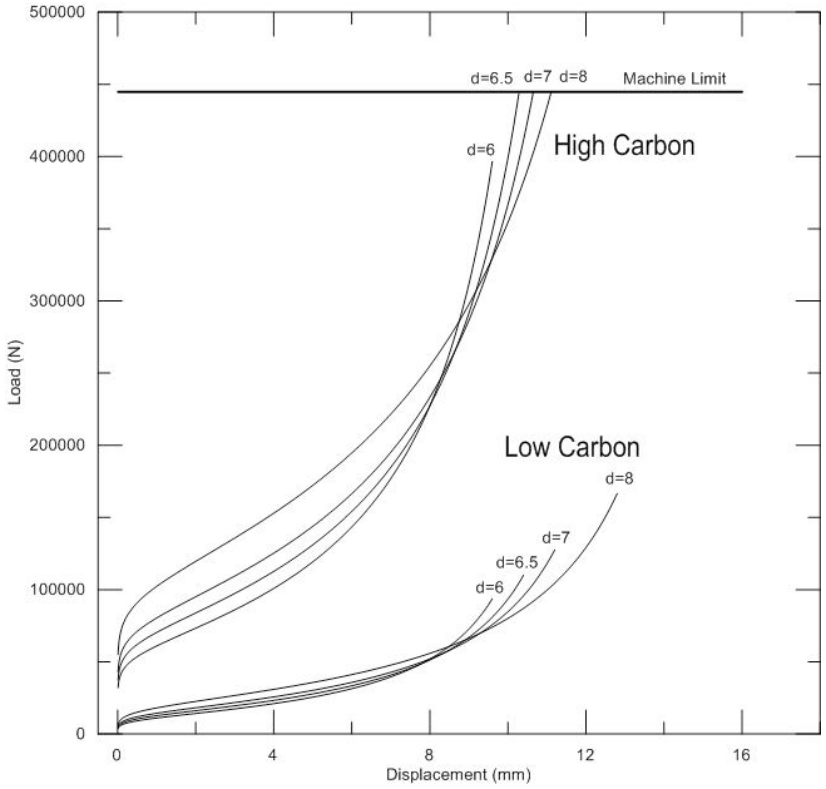

Figure A.2 Theoretical load-displacement curves for low and high carbon steels of the various indicated diameters (mm). The low carbon steel has an n=0.21 and a K=600 MPa and the high carbon has an n=0.12 and a K=2650 MPa [29].The h/d ratio was assumed to be two for all materials.

APPENDIX B: SUMMARY OF CRACK SEVERITY FOR 1045 SERIES SAMPLES TESTED AT THE THREE DEFORMATION SPEEDS

This appendix presents data on the crack severity for as-received 1045 materials tested at three impact speeds employed in the initial stage of testing. Macrographs illustrating each degree of severity (uncracked, low, moderate or high) are first presented and then a table is presented for each one of as-received 1045 material.

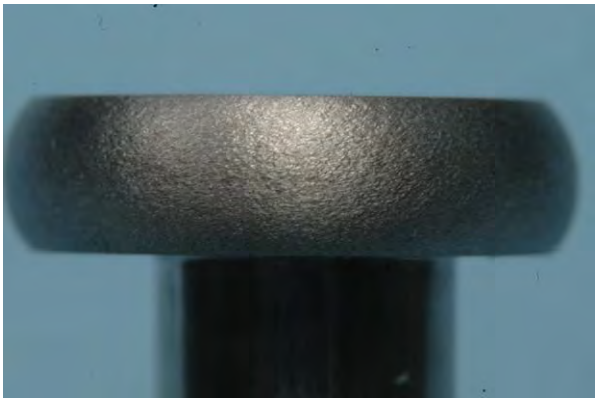

Figure B.1 Macrograph of a 1045 Al TMP sample cold headed to 72 pct engineering strain using the 0.15 mm/s speed. This sample represents an uncracked sample with respect to strain rate effects evaluation. Compressed height = 3.16 mm.

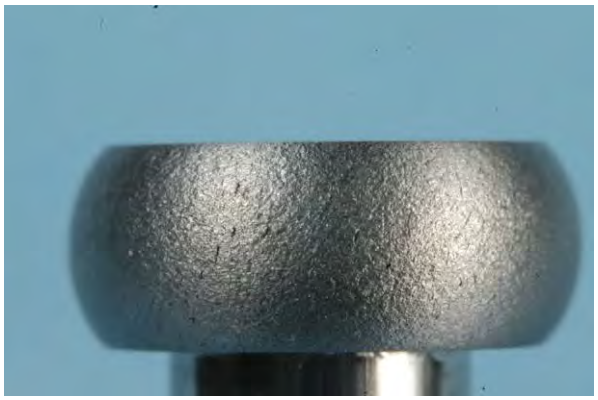

(a)

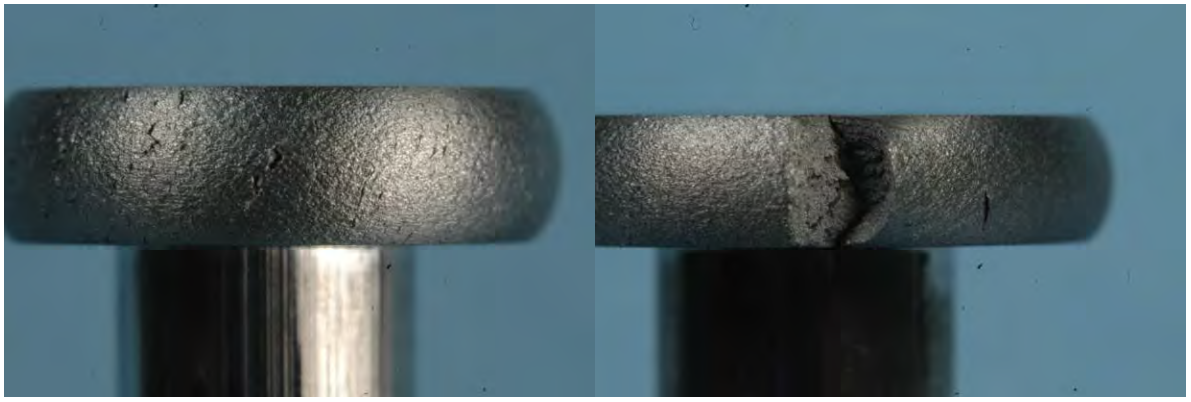

(b) (c)

Figure B.2 Macrographs of laboratory cold headed samples showing increasing degree of longitudinal cracking severity. (a) 10V45-TMP sample cold headed to 63.3% engineering strain using the 15 mm/s speed. Low severity longitudinal cracks are illustrated. Compressed height = 4.18 mm (b) 10V45 w/Nb sample cold headed to 68.9% engineering strain using the 0.15 mm/s speed. Moderate longitudinal cracks are illustrated. Compressed height = 3.20 mm (c) 1045 Al-TMP sample cold headed to 75.5% engineering strain using the1.5 mm/s speed. High severity longitudinal cracks are illustrated. Compressed height = 2.68 mm.

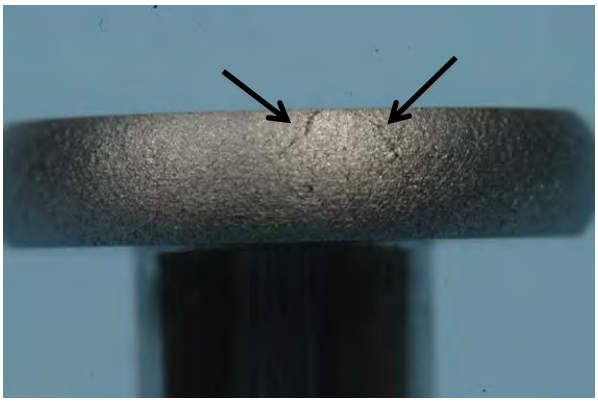

(a)

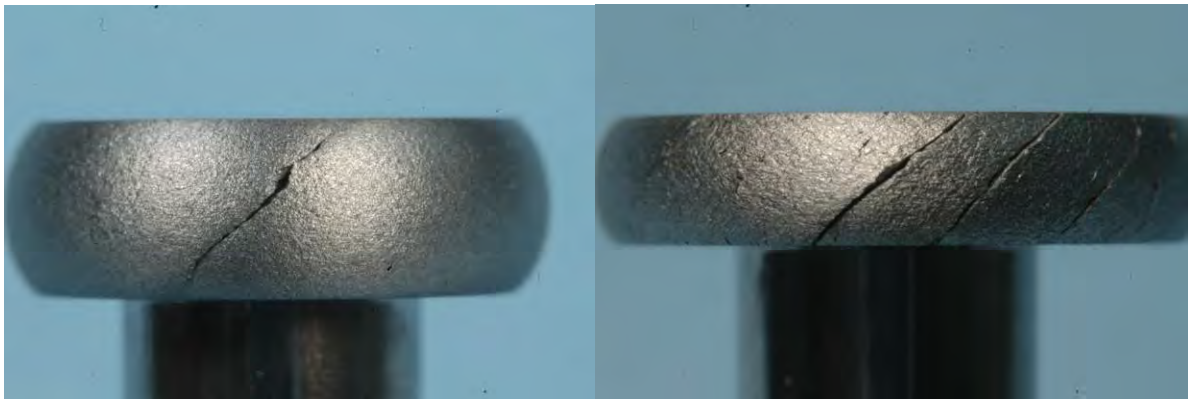

(b) (c)

Figure B.3 Photographs of laboratory cold headed samples showing increasing degree of shear crack severity. (a) 1045 Al TMP sample cold headed to 76.1% engineering strain using the 1.5 mm/s speed. Low severity shear cracks are pointed out by the arrows. Compressed height = 2.68 mm (b) 1045 Al TMP sample cold headed to 68.5% engineering strain using the 15 mm/s speed. Moderate severity shear cracking is illustrated. Compressed height = 3.59 mm (c) 10V45 sample cold headed to 80.0% engineering strain using the 0.15 mm/s speed. High degree of shear cracking is shown. Compressed height = 2.68 mm.

Table B.1 – Summary of Cracking Severity for Selected 1045 Al Samples at The Three Deformation Speeds

Engineering Strain (%)	Crack	0.15 mm/s		1.5 mm/s		15 mm/s
		First Sample	Duplicate	First Sample	Duplicate	
57.9-58.4	Shear	None		None	None	None
	Longitudinal	None		None	None	None
66.8-67.9	Shear	None	None	None	None	
	Longitudinal	None	None	None	None	
75.8-76.5	Shear	Low	Low	High	Moderate	High
	Longitudinal	None	None	None	Moderate	Moderate
81.6	Shear	High	High			
	Longitudinal	Moderate	Moderate			

Table B.2 – Summary of Cracking Severity for 1045 Al TMP Samples at The Three Deformation Speeds

Engineering Strain (%)	Crack	0.15 mm/s	1.5 mm/s	15 mm/s
63.6	Shear			None
	Longitudinal			None
67.9-68.5	Shear		None	Moderate
	Longitudinal		None	Low
71.8-71.9	Shear	None	Low	
	Longitudinal	None	Low	
76.0	Shear	Moderate	Moderate	
	Longitudinal	Low	Low	

Table B.3 – Summary of Cracking Severity for 10V45 Samples at The Three Deformation Speeds

Engineering Strain (%)	Crack	0.15 mm/s		1.5 mm/s		15 mm/s	
		First Sample	Duplicate	First Sample	Duplicate	First Sample	Duplicate
57.7-58.0	Shear	None	None	None	None	None	None
	Longitudinal	None	None	Low	Low	None	None
67.3-68.0	Shear	Low	Moderate	None	None	None	None
	Longitudinal	None	Low	Low	None	Moderate	Low
75.8-76.2	Shear	High	Moderate	Moderate	High	High	Moderate
	Longitudinal	Low	Low	High	Moderate	Low	Moderate

Table B.4 – Summary of Cracking Severity for 10V45 TMP Samples at The Three Deformation Speeds

Engineering Strain (%)	Crack	0.15 mm/s		1.5 mm/s		15 mm/s	
		First Sample	Duplicate	First Sample	Duplicate	First Sample	Duplicate
57.8-58.3	Shear	None				None	
	Longitudinal	None				None	
62.5-63.3	Shear	Moderate	None	None	None	None	None
	Longitudinal	Low	low	low	low	Low	Low
67.2-68.7	Shear	Moderate		Low		Moderate	
	Longitudinal	Low		Moderate		Moderate	

Table B.5 – Summary of Cracking Severity for 10V45 w/Nb Samples at The Three Deformation Speeds

Engineering Strain (%)	Crack	0.15 mm/s	1.5 mm/s	15 mm/s
57.8-58.3	Shear	None	None	None
	Longitudinal	Low	Low	Low
62.5-63.3	Shear	None	None	Low
	Longitudinal	Low	Low	Moderate
67.2-68.7	Shear	Moderate	None	None
	Longitudinal	Moderate	Moderate	Moderate

Table B.6 – Summary of Cracking Severity for 10V45 w/Nb TMP Samples at The Three Deformation Speeds

Engineering Strain (%)	Crack	0.15 mm/s	1.5 mm/s		15 mm/s
			First Sample	Duplicate	
62.6-62.9	Shear	Low			
	Longitudinal	Low			
67.6-68.0	Shear	Moderate	Low	Moderate	None
	Longitudinal	Low	Low	Low	High
71.9	Shear		High		
	Longitudinal		Low		

APPENDIX C: SULFIDE LENGTH DISTRIBUTION CHARTS FROM INCLUSION ANALYSIS DATA

This appendix lists sulfide length distribution charts for all materials used in the inlcusion analysis. These materials are as-received 1045 materials, hot-rolled 4135, control-rolled 16MnCr5 and 1080V.

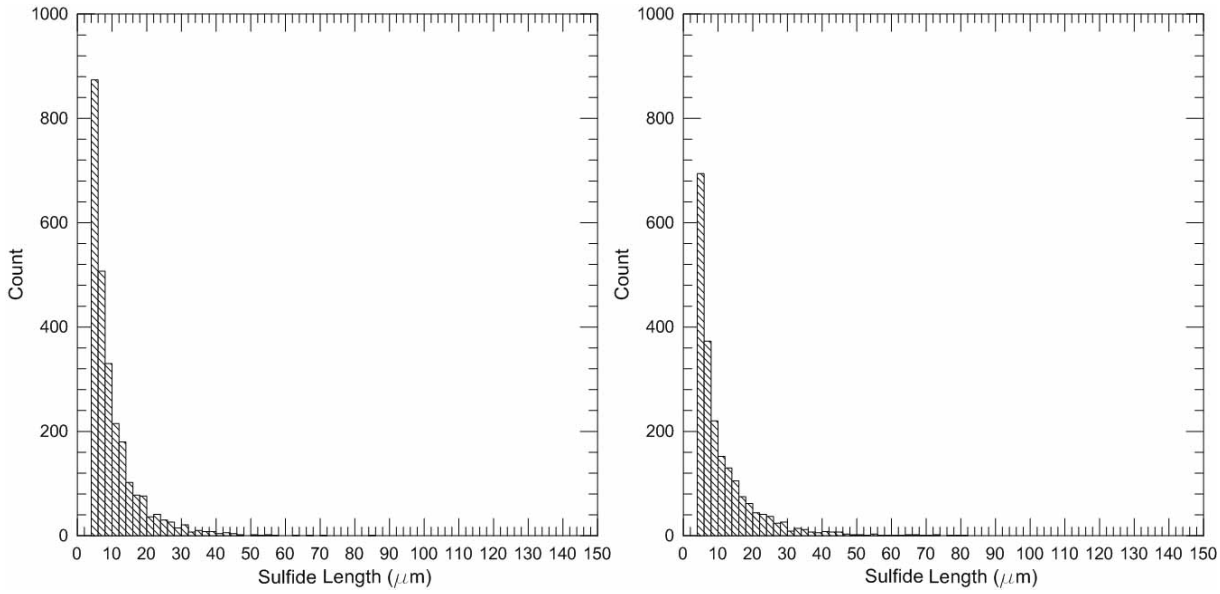

(a) (b)

Figure C.1 Sulfide length distribution charts for a) 1045 Al b) 1045 Al TMP.

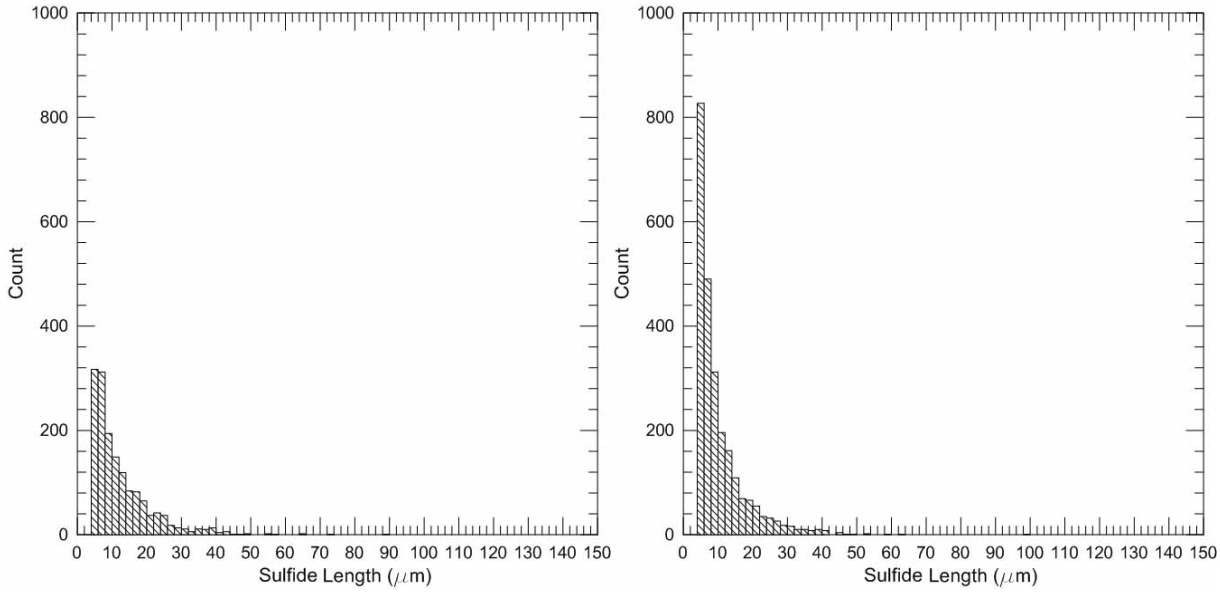

(a) (b)

Figure C.2 Sulfide length distribution charts for a) 10V45 b) 10V45 TMP.

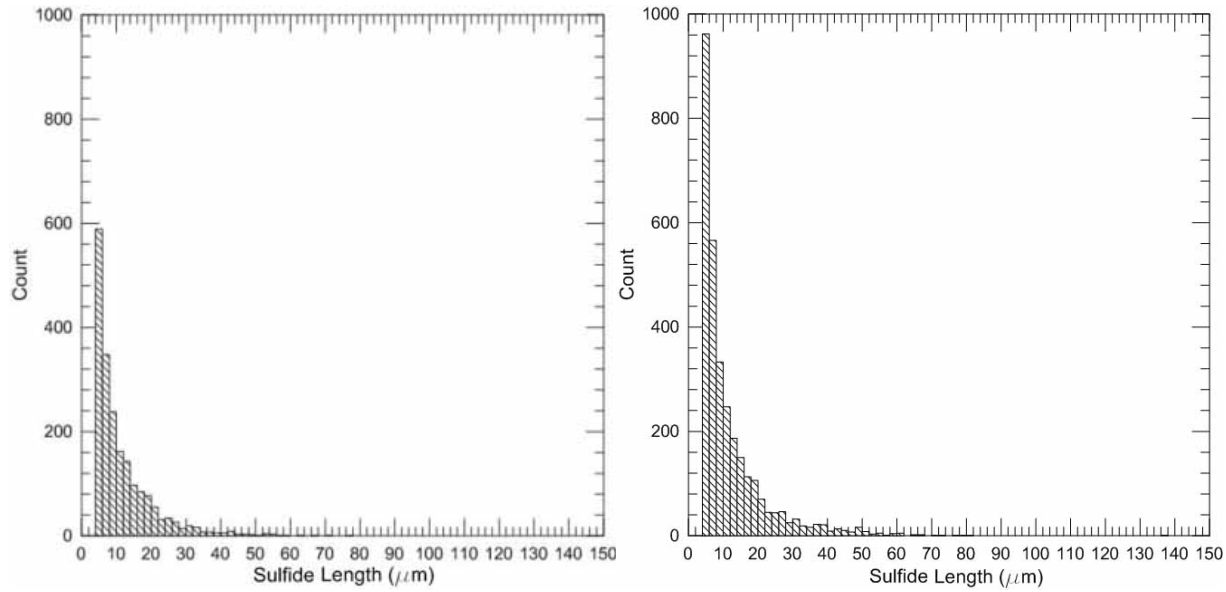

(a) (b)

Figure C.3 Sulfide length distribution charts for a) 10V45 w/Nb b) 10V45 w/Nb TMP.

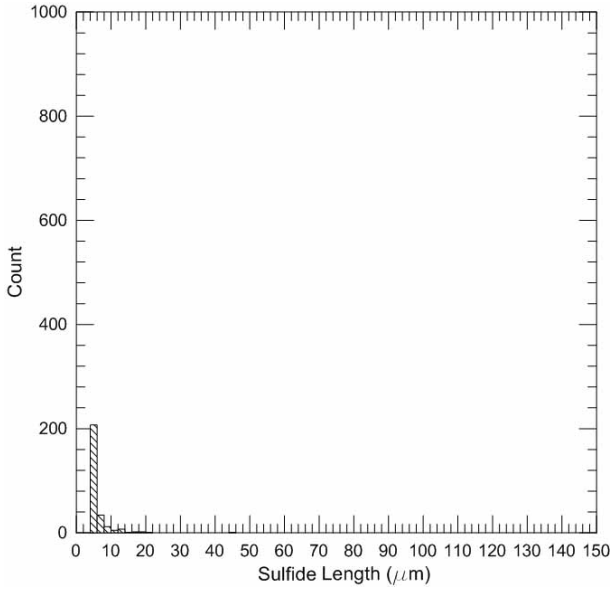

Figure C.4 Sulfide length distribution chart for hot-rolled 4135.

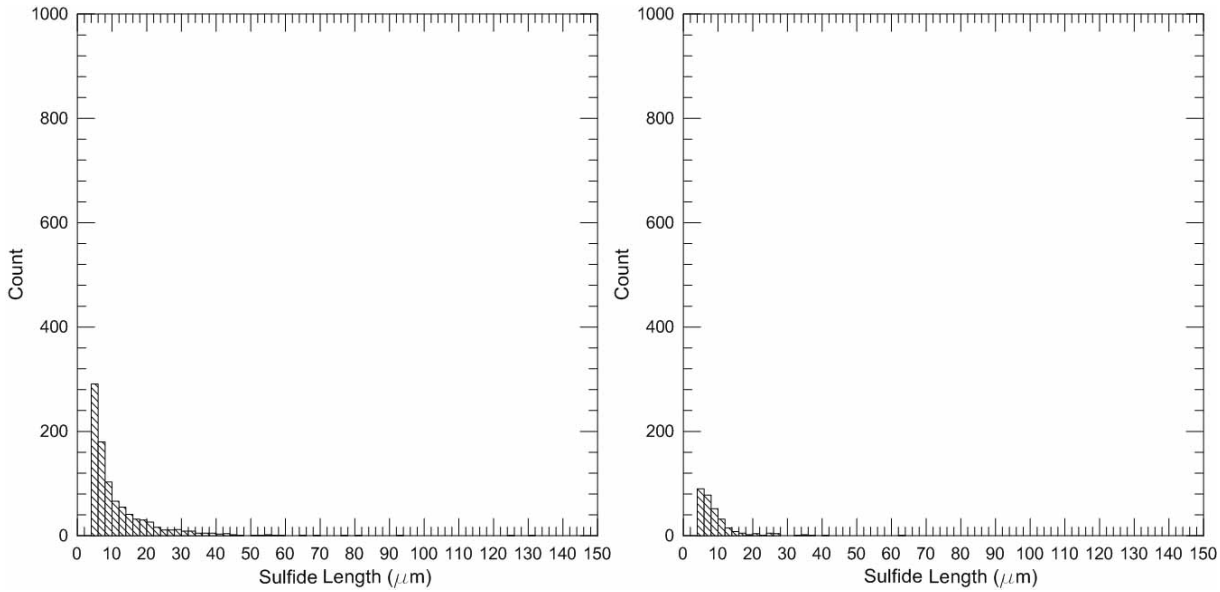

(a) (b)

Figure C.5 Sulfide length distribution charts for a) CR 16MnCr5 and b) 1080V.